POLITECNICO DI MILANO

Scuola di Ingegneria dei Sistemi

Corso di Laurea Magistrale in Ingegneria Fisica

Dipartimento di Fisica

Charge transfer effects in Co-phthalocyanine single molecule magnets on graphene

Relatore: Prof. Giacomo Claudio Ghiringhelli

Correlatore: Dr.ssa Violetta Sessi

Tesi di Laurea di:

Greta DELLEA

Matr. Nr. 751056

Anno Accademico 2011-2012

Abstract

In this thesis we investigated the electronic and magnetic coupling in hybrid graphene-single molecule magnets systems. This project is the result of a collaboration between the ESRF (European Synchrotron Radiation Facility) and the NANOsciences department of Istitut Néel, CNRS, Grenoble.

Graphene samples have been produced using a chemical vapor deposition (CVD) technique that both allows to obtain large graphene areas and to transfer them on dielectric substrates (SiO_2/Si^{++} and $SrTiO_3$) in order to perform field effect measurements. The morphological and electrical characterization of our samples shows that they are formed by a single graphene layer with only a few percent of defected areas and intrinsic hole (graphene/SiO_2/Si^{++}) or electron (graphene/$SrTiO_3$) doping.

Cobalt phthalocyanine (CoPc) single molecule magnets have been deposited *in-situ* and at room temperature on graphene substrates and on a highly oriented pyrolytic graphite (HOPG) substrate used as a reference. The evaporation process has been calibrated in order to achieve a coverage of ~10% of a monolayer of molecules on the surface.

From X-ray absorption spectroscopy measurements (X-ray magnetic circular dichroism and X-ray linear dichroism) we found that CoPc molecules do not interact with HOPG or hole doped graphene, so that the free molecule electronic ground state is retained. Opposite to that, evidence of a charge transfer effect from the substrate is observed in CoPc deposited on electron doped graphene, resulting in an almost complete quenching of the magnetic moment associated to the central cobalt ion. These results are similar to experimental results and theoretical models for CoPc deposited on metals but in addition suggest the possibility of progressively controlling the magnetic moment of CoPc just by changing the density of carriers at the Fermi level in graphene.

Estratto in italiano

Grafene e singoli magneti molecolari rappresentano due tra i settori di ricerca più all'avanguardia nel campo della scienza dei materiali e delle nanotecnologie. Nell'arco dell'ultimo decennio un crescente numero di ricercatori si è dedicato al loro studio, mossi sia dalle proprietà uniche che dalle potenzialità innovative di questi materiali.

Con l'espressione singoli magneti molecolari si designa una categoria di nano-oggetti appartenenti alla classe dei nano-magneti che sono caratterizzati dal mantenere una configurazione elettronica di tipo atomico, con un momento di spin ben definito ad essa associato, a differenza per esempio di quanto accade nei nano-cluster, che sono invece dei veri e propri aggregati di atomi con proprietà magnetiche.

Per via della loro peculiare struttura elettronica, i singoli magneti molecolari sono considerati degli ottimi candidati per diventare gli elementi di base a partire dai quali costruire un nuovo campo dell'elettronica: la spintronica molecolare. Con spintronica si intende un settore nuovo dell'elettronica, anche noto come elettronica di spin, basato sulla capacità da parte di una correte elettrica polarizzata in spin di trasportare dell'informazione interagendo con materiali magnetici. Questa proprietà permette quindi la raccolta e la trasmissione di informazioni semplicemente modificando lo stato magnetico del sistema.

Per quanto riguarda il grafene, invece, esso è un ormai noto materiale bidimensionale costituito da atomi di carbonio disposti lungo i vertici di una struttura "a nido d'ape". La presenza di questo particolare reticolo cristallino fa sì che il grafene presenti proprietà uniche in termini di struttura a bande e conducibilità elettrica. È stato infatti provato che in corrispondenza del livello di Fermi esso possiede una densità di elettroni pressoché nulla, quest'ultima può inoltre essere variata con continuità per mezzo dell'applicazione di un opportuno campo elettrico (effetto di campo) o tramite drogaggio chimico.

A questo punto è interessate cercare di comprendere come questi due sistemi –singoli magneti molecolari e grafene– possano essere accoppiati tra loro.

Il punto di partenza per comprendere questo accoppiamento è costituito da un recente

risultato sperimentale ad opera di Crommie *et al.* [1] nel quale si suggerisce l'idea che le proprietà elettroniche e magnetiche di singoli adatomi di cobalto depositati sulla superficie di un dispositivo a base di grafene possano essere modificate tramite effetto di campo. Si introduce così l'idea di utilizzare il grafene per controllare lo spin atomico attraverso opportuni campi elettrici e in modo reversibile.

La possibilità di fare lo stesso utilizzando singoli magneti molecolari aprirebbe la strada alla realizzazione di memorie e dispositivi basati sulla spintronica, nei quali l'informazione associata al momento magnetico delle molecole può essere modificata semplicemente tramite l'applicazione di un campo elettrico, anziché magnetico, come quelli normalmente utilizzati in questi settori.

Sebbene una concreta implementazione tecnologica di questi dispositive potrebbe essere ancora molto lontana, al momento sembrano sempre più necessari esperimenti che testino la reale possibilità di avere accoppiamento tra singoli magneti molecolari e grafene. In particolare la comprensione dei meccanismi fisici alla base di una possibile interazione e le condizioni in cui essa stessa possa essere realizzata risultano di fondamentale importanza per ogni applicazione futura.

In questo contesto, l'esperimento presentato in questa tesi ha l'obiettivo di investigare la possibilità di accoppiare lo spin di un singolo magnete molecolare con gli elettroni del grafene attraverso un meccanismo di trasferimento di carica (CT). La realizzazione di questo progetto è stata possibile grazie a una collaborazione tra il sincrotrone europeo ESRF (European Synchrotron Radiation Facility) and il dipartimento NANOsciences dell'Istituto Néel, CNRS, Grenoble.

Come magneti molecolari si è deciso di utilizzare le cobalto ftalocianine (CoPc), dal momento che queste molecole costituiscono dei sistemi estremamente stabili dove il momento magnetico è principalmente associato all'atomo centrale di cobalto. Inoltre, un possibile processo di trasferimento di carica con substrati metallici è già stato analizzato in grande dettaglio per queste molecole, semplificando notevolmente l'interpretazione dei nostri dati.

I campioni di grafene sono stati prodotti usando una tecnica di deposizione chimica da fase vapore (CVD), che permette allo stesso tempo di ottenere delle superfici estese di grafene (campioni millimetrici sono necessari per le successive misure al sincrotrone) e in un secondo momento di trasferire il grafene così prodotto su dei substrati di materiale

dielettrico (SiO_2/Si^{++} and $SrTiO_3$) creando così dei dispositivi a effetto di campo.
Da una caratterizzazione elettrica e morfologica dei nostri campioni si evidenzia come essi siano costituiti da un solo strato atomico di grafene, con solo una ridotta percentuale di difetti, e presentino un drogaggio intrinseco di elettroni (grafene/$SrTiO_3$) o di lacune (grafene/SiO_2/Si^{++}) dovuto al processo stesso di fabbricazione.
Le cobalto ftalocianine sono state depositate *in-situ* e a temperatura ambiente su substrati di grafene e HOPG (acronimo di "highly oriented pyrolytic graphite", che sta ad indicare un particolare tipo di grafite caratterizzato da un ordine strutturale particolarmente elevato e spesso utilizzato come campione di riferimento in esperimenti inerenti il grafene). Il processo di evaporazione è stato calibrato in modo tale da ottenere un ricoprimento di molecole sulla superficie dell'ordine del ~10% di un singolo strato atomico.
Attraverso misure di spettroscopia di assorbimento con l'utilizzo di raggi X, quali la XAS (X-ray absorption spectroscopy), la XMCD (X-ray magnetic circular dichroism) e la XLD (X-ray linear dichroism), abbiamo concluso che le cobalto ftalocianine non presentano fenomeni di interazione con i substrati di HOPG e grafene drogato con lacune, e lo stato fondamentale elettronico delle molecola isolata è conservato. Un cambiamento drammatico nella forma degli spettri di assorbimento è stato invece riscontrato nel caso di cobalto ftalocianine depositate su grafene drogato con elettroni. Queste misure preliminari suggeriscono la presenza di un effetto di trasferimento di carica tra il substrato e le molecole, tale da indurre un quasi completo annullamento del momento magnetico associato allo ione centrale di cobalto.
Questi risultati sono simili a quanto predetto da modelli teorici e riportato per esperimenti analoghi nel caso di cobalto ftalocianine depositate su superfici metalliche, ma in aggiunta a quanto già studiato suggeriscono la possibilità di controllare progressivamente il momento magnetico delle CoPc semplicemente cambiando la densità di cariche al livello di Fermi del grafene.
Traendo ispirazione da questi risultati, è in progetto per il futuro di focalizzarsi su esperimenti in cui il processo di trasferimento di carica possa essere controllato dall'esterno in modo reversibile e non soltanto indotto da un differente doping chimico dei substrati. Per ottenere questo risultato sarà quindi necessario produrre campioni di

grafene in cui il drogaggio possa essere variato da elettroni a lacune (e viceversa) applicando un opportuno potenziale di gate.

Il lavoro presentato nel seguito della tesi è suddiviso in due parti principali: (i) la fabbricazione e caratterizzazione dei campioni di grafene e (ii) lo studio dei sistemi ibridi CoPc-grafene attraverso radiazione di sincrotrone.

La tesi stessa verrà sviluppata nel seguente modo:

Nel *primo capitolo* verrà presentata una breve introduzione alle proprietà del grafene e delle cobalto fatalocianine.

Il *secondo capitolo* verrà dedicato allo sviluppo dei dispositivi a base di grafene e alla loro caratterizzazione con misure di microscopia e trasporto.

Nel *terzo capitolo* verrà mostrato lo studio delle CoPc depositate su grafene tramite tecniche di spettroscopia con raggi X, con una particolare attenzione all'accoppiamento tra gli elettroni del grafene e lo spin dello ione centrale TM (metallo di transizione) della molecola.

Infine, nella sezione *Conclusions and Outlook* verranno riassunti i principali risultati ottenuti nel corso di questo lavoro di tesi, insieme con idee per nuovi esperimenti che vadano a completare e approfondire il lavoro fin qui svolto.

Contents

List of figures

Introduction

Single molecule magnets and graphene are two main topics in the fields of material science and nanotechnology. In the last decade an increasing number of researchers moved to these two subjects attracted both by the unique properties and the innovative potentialities of these materials.

On the one hand, single molecule magnets are nano-objects quite interesting within the class of nano-magnets as, differently from magnetic nano-clusters which are aggregations of magnetic atoms, retain an atomic-like electronic configuration with an associated spin moment. For this reason these structures are expected to provide the building blocks for a new field of electronics, which takes advantage of both their reduced dimension and their magnetic behavior: molecular spintronics. Spintronics is a new field, but already with technical applications [2], based on the capability of a spin polarized electrical current to carry information while interacting with magnetic materials. This property allows to store and transmit information just by changing the magnetic state of the system [3].

On the other hand, graphene is a well known two dimensional system formed by carbon atoms arranged in a honeycomb lattice, and due to this peculiar lattice structure it presents unique properties in terms of band structure and conductive behavior. Indeed it has been found to possess a vanishing electron density in correspondence of the Fermi level, that can be continuously tuned by means of either electric field effect or chemical doping [4].

It is now interesting to figure out how these two systems -single molecule magnets and graphene- can be coupled.

The starting point is a recent experimental result [1] that suggested that electronic and even magnetic proprieties of cobalt ad-atoms deposited on graphene could be tuned by the field effect in graphene. This experiment envisages the possibility of controlling the atomic spin by means of electric fields, in a reversible way.

The possibility of doing the same by using single molecule magnets would open up the

way to memories and spintronics devices in which the information contained in the magnetic moment of the molecules can be changed by simply applying an electric field instead of the normally used magnetic field.

Even though the way to a real technological implementation might be very long, experiments that test the coupling of single molecules magnets with graphene are currently needed. In particular, understanding the basic physical mechanism of this interaction and the conditions under which it can be realized is of fundamental importance for any future application.

The experiments presented in this thesis had the aim to investigate whether the spin of a single molecule magnet can be coupled to graphene electrons through charge transfer (CT) mechanisms. Cobalt phthalocyanine (CoPc) molecules have been chosen as molecular magnets, since they are a very stable and simple system were the magnetic moment is mainly due to the central cobalt ion. Moreover, a possible charge transfer process with metallic substrates has already been investigated in detail for these molecules, which simplified the interpretation of our data.

The work presented in the following was divided in two main parts: (i) fabrication and characterization of proper graphene samples and (ii) study of hybrid systems CoPc-graphene by synchrotron radiation.

The thesis will be developed in the following way:

In the first chapter a brief introduction to the properties of graphene and CoPc molecules will be presented.

The second chapter will be dedicated to the development of graphene devices and their characterization by microscopy and transport measurements.

In the *third chapter* X-ray spectroscopy studies of cobalt phthalocyanines on graphene will be shown, with focus on the coupling between graphene electrons and transitional metal (TM) ion spin.

Finally in *Conclusions and Outlook* the most important achievements of the thesis will be summarized together with ideas for new experiments complementing the present work.

Chapter 1

Properties of graphene and Co-phthalocyanine single molecule magnets

In this chapter a brief introduction to the physics of hybrid graphene-single molecule magnets systems will be presented.
After a discussion of graphene history and its main properties, the possibility of changing the density of states at the Fermi level by means of a gate voltage or chemical doping will be discussed.
Then, single molecule magnets will be introduced, with a particular attention to cobalt phthalocyanine molecules, the ones used in our experiment.
Finally, the state of the art experiments and predictions about CoPc magnetic and electronic coupling with different substrates will be introduced.

1.1. Graphene: history and properties

Graphene is a single two-dimensional layer of carbon atoms bound in a hexagonal lattice structure. It is a basic building block for graphitic materials of all other dimensionalities (see *Figure 1.1* [5]). It can be wrapped up into 0D fullerenes, rolled into 1D nanotubes or stacked into 3D graphite.
Even though Graphene (known even as “2D graphite”) has been studied by theoretists

already seventy years ago [6], it was isolated for the first time only in 2004 by Andre Geim and Konstantin Novoselov, who won the 2010 noble prize in physics for their groundbreaking work on graphene [4].

From that moment, graphene has increasingly attracted the interest of researches due to a number of exceptional properties that it has been found to possess. In the following the most interesting properties, in view of our experiments, will be presented.

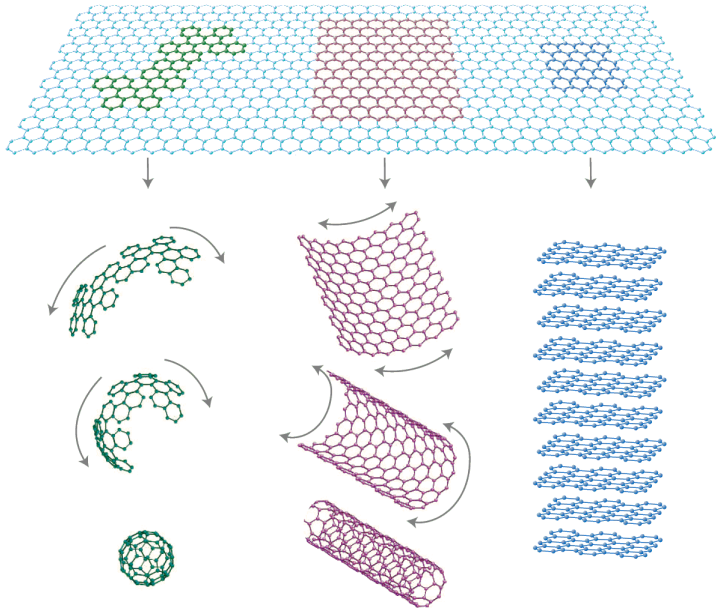

Figure 1.1*: Graphene can be seen as the 2D building block material for carbon materials of all other dimensionalities. It can be wrapped up into 0D 'buckyballs' fullerenes, rolled into 1D nanotubes or stacked into 3D graphite (after Novoselov and Geim, 2007 [5]).*

1.1.1. A material that should not exist

A bidimensional crystal like graphene was thought impossible 70 years ago. Indeed, Landau and Peierls argued that strictly 2D crystals were thermodynamically unstable and could not exist. Their theory pointed out that a long range order in two dimensional systems would be destroyed by thermal fluctuations. The latter in fact lead to a displacement of atoms of the order of the inter-atomic distance at any finite temperature,

making 2D crystals unstable, since they would simply melt [7-8].

The argument was later extended by Mermin [9] and it is strongly supported by experimental observations [10]. Indeed, the melting temperature of thin films rapidly decreases with decreasing thickness, single layers being an extreme case of this scenario.

How come that we still speak about graphene 70 years later?

As graphene lives in a three dimensional world, thermal fluctuations can be dissipated in the third dimension making the two dimensional crystal stable. This does not contradict Peierls and Landau's conclusion, that was based on a bidimensional crystal living in a bidimensional world. The cost of this stability is a deformation in the third direction, which makes graphene not perfectly flat.

Undulations have been observed experimentally, in particular in suspended graphene. They are on average 1 nm high and 10 nm long, they are smooth and surprisingly they do not create any defects in the crystalline structure [11].

1.1.2. Electronic structure: Dirac point and massless Dirac fermions

Graphene has a remarkable band structure thanks to its crystalline structure. Carbon atoms form a hexagonal lattice where each carbon atom is positioned at a distance a = 1.42 Å from its three neighbors.

Carbon atoms have six electrons ($1s^2 2s^2 2p^2$), in the ground state two of them are core electrons, close to the nucleus and irrelevant for chemical reactions, while the four electrons remaining are valence electrons. In graphene three of these electrons occupy sp^2 carbon hybrid orbitals and form strong covalent σ-bonds with the neighbor atoms, the remaining one occupies a $2p_z$ hybrid orbital and yields π-bonds, that are oriented in the z-direction (out of the plane). Each atom has one of these π-bonds.

$2p_z$ orbitals from neighboring atoms are then hybridized together to form the crystalline π-bands and π*-bands. These bands are responsible for the most peculiar electronic proprieties of graphene, as we will see in the following. There is then one electron per

atom related to the electronic properties at low energies, and three electrons that form energy bands far from the Fermi level and that are related to the honeycomb lattice.

The hexagonal structure describing carbon atoms arrangement in graphene is not a Bravais lattice, since atoms in the crystal are not equivalent (they do not "see" the same environment). Indeed, the hexagonal lattice of graphene can be regarded as two interlaying triangular Bravais lattices. Carbon atoms are then classified into atoms of type A and atoms of type B. Atoms of type A have a nearest neighbor in the north and two in the south. Atoms of type B have two nearest neighbors in the north and one in the south. See *Figure 1.2*.

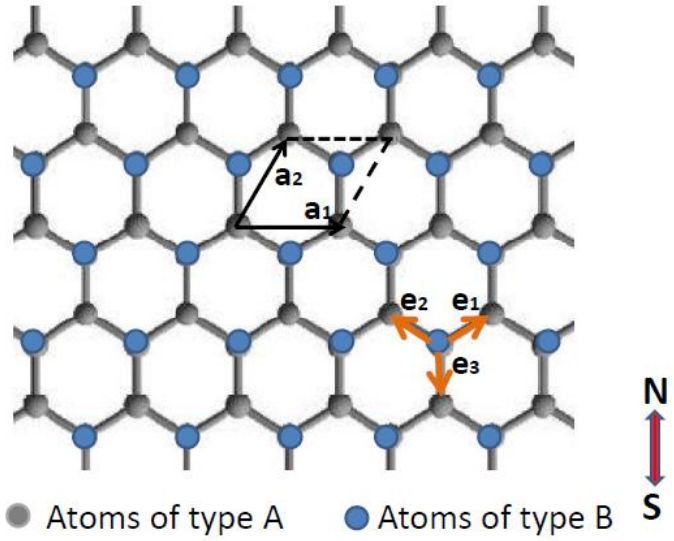

***Figure 1.2**: Honeycomb lattice structure of graphene. Lattice vectors $\boldsymbol{a_1}$ and $\boldsymbol{a_2}$ denote a triangular Bravais lattice with two atoms A and B per unit cell. Vectors $\boldsymbol{e_1}$, $\boldsymbol{e_2}$ and $\boldsymbol{e_3}$ indicate the nearest neighbors of type B atoms. Each atom in sublattice A has three nearest neighbors in sublattice B and viceversa.*

Positions of nearest neighbors of atoms B are determined by the vectors $\boldsymbol{e_1}$, $\boldsymbol{e_2}$ and $\boldsymbol{e_2}$:

$$\boldsymbol{e_1} = \frac{a}{2}\left(\sqrt{3}\,\boldsymbol{e_x} + \boldsymbol{e_y}\right) \tag{1.1}$$

$$\boldsymbol{e_2} = \frac{a}{2}\left(-\sqrt{3}\,\boldsymbol{e_x} + \boldsymbol{e_y}\right) \tag{1.2}$$

$$\boldsymbol{e_3} = -a\boldsymbol{e_y} \tag{1.3}$$

Here $\boldsymbol{e_x}$, $\boldsymbol{e_y}$ and $\boldsymbol{e_z}$ are the unit vectors in the three Cartesian directions.

This definition will be used in the following.

The hexagonal (honeycomb) lattice instead can be described by the unit lattice vectors $\boldsymbol{a_1}$ and $\boldsymbol{a_2}$ as:

$$\boldsymbol{a_1} = \sqrt{3}a\,\boldsymbol{e_x} \tag{1.4}$$

$$\boldsymbol{a_2} = \frac{\sqrt{3}a}{2}\left(\boldsymbol{e_x} + \sqrt{3}\,\boldsymbol{e_y}\right) \tag{1.5}$$

Known the Bravais lattice, it is now possible to calculate the reciprocal lattice. Reciprocal lattice vectors are given by the relations:

$$\boldsymbol{a_1^*} = \frac{2\pi}{\sqrt{3}a}\left(\boldsymbol{e_x} - \frac{\boldsymbol{e_y}}{\sqrt{3}}\right) \tag{1.6}$$

$$\boldsymbol{a_2^*} = \frac{4\pi}{\sqrt{3}a}\,\boldsymbol{e_y} \tag{1.7}$$

Even the reciprocal lattice presents an honeycomb like structure and the First Brillouin Zone is hexagonal with two inequivalent points K and K', as reported in *Figure 1.3*.

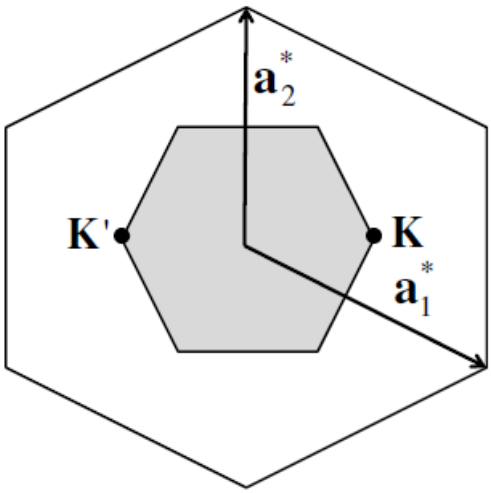

***Figure 1.3**: Unite cell of the graphene reciprocal lattice and First Brillouin Zone with the two inequivalent points K and K'.*

K and K' cannot be related using reciprocal lattice vectors and are identified it the reciprocal space by the vectors $\mathbf{K}^+$ and $\mathbf{K}^-$:

$$\boldsymbol{K}^{\pm} = \pm\frac{4\pi}{3\sqrt{3}a}\boldsymbol{e_x} \tag{1.8}$$

Other equivalents points can be obtained from K and K' with a translation of the reciprocal vector:

$$\boldsymbol{G} = \gamma_1\boldsymbol{a_1^*} + \gamma_2\boldsymbol{a_2^*} \tag{1.9}$$

where γ_1 and γ_2 are integers.

This crystalline structure of graphene is the starting point for the calculation of the band structure of a monolayer graphene. It was first calculated by Wallace in 1947, when he obtained the band structure of a "single layer of graphite" using a tight-binding approximation [12].

Following the original work of Wallace, the tight-binding Hamiltonian can be written using a basis of two atoms (the A and B atoms introduced before) per unit cell, and is given by the relation:

$$H_{\boldsymbol{k}} = \begin{pmatrix} \epsilon_A & te^{i\boldsymbol{k}\cdot\boldsymbol{e_1}} + te^{i\boldsymbol{k}\cdot\boldsymbol{e_2}} + te^{i\boldsymbol{k}\cdot\boldsymbol{e_3}} \\ c.c. & \epsilon_B \end{pmatrix} \tag{1.10}$$

where $\boldsymbol{k}$ is the electron momentum, $\boldsymbol{e_1}$, $\boldsymbol{e_2}$ and $\boldsymbol{e_3}$ are the positions of the three nearest neighbors as defined before, $\epsilon_A = \epsilon_B = 0$ are the on-site energies of the carbon atoms on sites A and B, $t \simeq 2.7$ eV is the nearest neighbors hopping integral[1] calculated between A and B sites, and *c.c.* is the complex conjugate of the off-diagonal matrix element.

Calculations of the eigenvalues of the tight-binding Hamiltonian lead to the dispersion relation between energy and momentum of electron within graphene, as shown in *Figure 1.4* [13]. Since graphene constrains the motion of electrons into two dimensions, the momentum space is reduced to two dimensions: $\boldsymbol{k} = (\ k_x, k_y\ )$. Electron and hole

[1] Next nearest neighbor hopping is not considered since overlap between wavefunctions in that case is $t' \simeq 0.1$ eV and affects dispersion relation only at energies of the order of 100 meV.

bands touch at the already seen K and K' points, called Dirac points. There is then no gap between the two bands. Since there are as many electrons π as carbon atoms, for neutral or ideal graphene, the valence band is full, while the conduction band is empty, so that the Fermi level is just at the contact point between the two bands. The Dirac points are located on the edges of the Brillouin zone, in correspondence of points K and K', which are crystallographically inequivalent. Graphene is then a zero-gap semiconductor with a valley degeneracy of $g_v = 2$. It can also be seen as a metal in which valence and conduction bands form a single band having a zero density of states at the Fermi level.

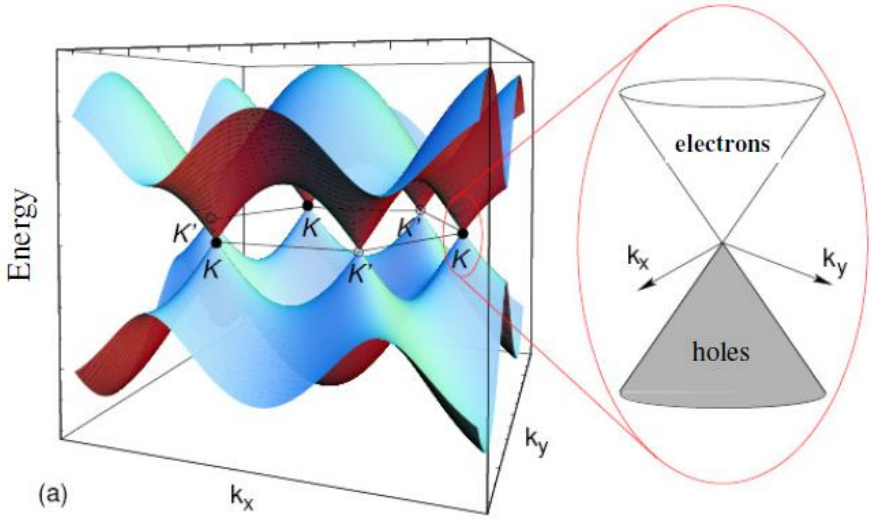

***Figure 1.4**: Dispersion relation of graphene. Electron and hole band touch at Dirac points K and K'. The zoom shows the low energy dispersion relation. From Ref. [13].*

When considering low energy excitations (energy E lower that $t \simeq 2.7$ eV) the tight-binding Hamiltonian can be developed around the Dirac point, giving a linear dispersion relation (see zoom in *Figure 1.4*) that is generally expressed as follows:

$$E_{\pm}(k) \approx \pm \hbar v_f |k - K| \tag{1.11}$$

The latter equation corresponds to the spectrum of the Dirac Hamiltonian for low-energy massless Dirac fermions, again calculated using a lattice with the basis {A, B}:

$$H_k = \hbar v_f \begin{pmatrix} 0 & k_x - ik_y \\ k_x + ik_y & 0 \end{pmatrix} = \hbar v_f \boldsymbol{\sigma} \cdot \boldsymbol{k} \quad (1.12)$$

$$\hbar v_f = \frac{3ta}{2} \quad (1.13)$$

where $\boldsymbol{\sigma}$ = (σ_x, σ_y) is the 2D vector of the Pauli matrices, The Dirac Hamiltonian was obtained expanding the tight-banding Hamiltonian close to K points. Using K' instead of K, the Hamiltonians (1.12) simply becomes: $H_{k'} = \hbar v_f \boldsymbol{\sigma}^* \cdot \boldsymbol{k}$, * denotes the complex conjugate, $\boldsymbol{k}$ is the electronic momentum, and the k-independent Fermi velocity of the electrons is $v_f \approx 10^6$ m/s, that is 1/300th of the speed of light in vacuum.

From the above considerations we conclude that Schroedinger equation is no more sufficient to describe electronic proprieties of graphene. Due to the interaction with the periodic potential arising from the honeycomb lattice of graphene, its charge carriers behave like relativistic quasiparticles and they are more efficiently described using the Dirac equation rather than the Shroedinger equation [14]. These quasiparticles, called massless Dirac fermions have a zero effective mass $m^* = 0$ and an effective speed v_f. Interest in graphene is then related to this peculiar behavior, that provides a way to probe quantum electrodynamics (QED) phenomena experimentally.

Finally, another interesting aspect of the graphene band structure is the symmetry between the conduction and the valence band near the Fermi level, a phenomena known as electron hole symmetry.

1.1.2.1. Graphene doping

The ability of external controlling the electronic properties of a material is at the hearth of modern electronics. In that way, graphene has attracted increasingly interest, due to its unique band structure, that lead to new transport effects, such as ambipolar field effect, which is absent in most conventional materials [4].

In graphene, in fact, is possible to change the position of the Fermi energy E_F with respect to the Dirac point. Charge carriers at the Fermi level can be tuned continuously between electrons and holes in concentration (n) as high as 10^{13} cm^{-2} and their

mobilities μ can exceed 15000 $cm^2\ V^{-1}\ s^{-1}$ even under temperature conditions [4]. Moreover, the mobility weakly depends on temperature, meaning that at 300 K it is still limited by impurity scattering and therefore can be improved significantly, even up to 100000 $cm^2\ V^{-1}\ s^{-1}$[4].

Actually, some other semiconductors exhibit mobility as high as 77000 $cm^2\ V^{-1}\ s^{-1}$ (for example in case of InSb) at room temperature, but those values are valid only for undoped bulk semiconductors. In graphene, mobility remains high even at high carrier density ($n > 10^{12}\ cm^2$) in both electrically and chemically doped devices.

There are two main possibilities for changing the Fermi level position of graphene: (i) chemical doping and (ii) application of a gate voltage.

In the latter case, graphene should be deposited on a dielectric material with an electrical contact underneath, the back gate[2]. By varying the applied gate voltage V_g between graphene and back-gate, it is possible to change the Fermi level of graphene. Top gate is also possible but we will focus on the method used in this thesis work.

Positive gate (negative) voltage induces electrons (holes) doping.

The concentration of the induced carriers can be estimated by the linear relation:

$$n = \alpha\, V_g \tag{1.14}$$

where the coefficient α ($cm^{-2}\ V^{-1}$) depends on the proprieties of the layer used as a dielectric [4].

This charge density shifts accordingly the Fermi level position in the band structure. It is possible to estimate the relationship between applied gate voltage and induced density of charges and Fermi level position. According with (1.11) the Fermi energy can be obtained as:

$$E_f = \hbar v_f k_f \tag{1.15}$$

Since graphene is a bidimensional material, the number of electronic states with momentum assuming values between k and $k+dk$, considering a spin and valley

[2] For more details about devices fabrication and density of charges evaluation, see paragraph 2.2.3.

degeneracy $g_s = g_v = 2$ and a total surface in the real space A, can be written as:

$$dn = 4\frac{A}{(2\pi)^2}2\pi k dk \tag{1.16}$$

Integrating over the k-space, from 0 to k_f, we obtain the total number of charges N (in the case of temperature $T = 0$K):

$$N = \frac{k_f^2 A}{\pi} \tag{1.17}$$

The relation between the surface density of charges (n) and the Fermi momentum (k_f) is:

$$n = \frac{N}{A} = \frac{k_f^2}{\pi} \quad \Rightarrow \quad k_f = \sqrt{\pi n} \tag{1.18}$$

Substituting the (1.18) in the (1.15) we finally obtain:

$$E_f = \hbar v_f \sqrt{2\pi n} = \hbar v_f \sqrt{\frac{2\pi Q}{Ae}} = \hbar v_f \sqrt{\frac{2\pi CV}{Ae}} = \hbar v_f \sqrt{\frac{2\pi \varepsilon_0 \varepsilon_r V_g}{de}} \tag{1.19}$$

Where Q is the total charge, C is the capacity of the dielectric material used as a substrate for graphene in transport measurements, d is its thickness and ε_r is the relative dielectric permittivity, ε_0 is the vacuum dielectric permittivity, V_g the gate voltage applied to the sample, and e is the electron charge.

If the Dirac point is shifted away from the V_g = 0V point, relation (1.19) can be expressed as a function of the difference between the gate voltage applied V_g and the gate voltage required to reach the Dirac point V_D:

$$E_f = \hbar v_f \sqrt{\frac{2\pi \varepsilon_0 \varepsilon_r (V_g - V_D)}{de}} \tag{1.20}$$

From (1.14) it is clear that at the Dirac point *n* should theoretically vanish, but thermally generated carriers and electrostatic spatial inhomogeneity limit the minimum charge density [4]. The ambipolar field effect corresponds to a change in charge resistivity ρ (or conductivity $\sigma = 1/\rho$) that occurs when the charge density is modified.

In *Figure 1.5* [4] the resistivity of graphene as first calculated by Novoselov and Geim (2004) is plotted as a function of the applied gate voltage. Resistivity rapidly decreases while adding or removing charge carriers starting from Vg = 0V, reaching its maximum at the Dirac point. This rapid variation in resistivity indicates that free carriers in graphene have a very high mobility, that can be estimated as $\mu = 1/en\rho$.

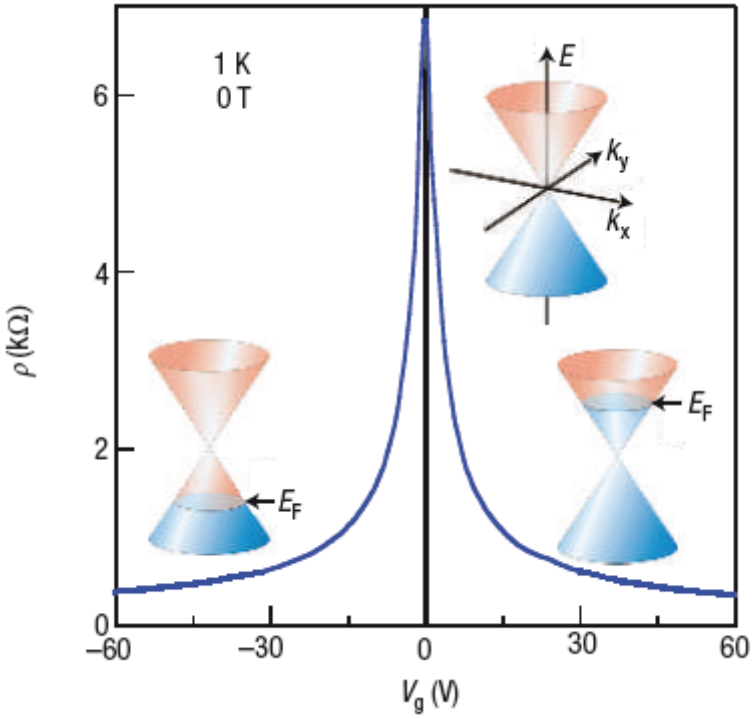

***Figure 1.5**: Ambipolar electric field effect in single layer graphene. The inserts show graphene low energy spectrum E(k) indicating changes in the position of the Fermi energy E_F while changing the gate voltage V_g. Positive (negative) V_g induces electrons (holes). The rapid increase in resistivity on adding charge carriers indicates their high mobility. Novoselov and Geim (2004) [4].*

So far it has been described how to change the Fermi level position in graphene by applying an appropriate gate voltage. This is not the only possibility. Dirac point tuning in graphene can also be achieved by means of chemical doping. The mechanism of

chemical doping in graphene is still controversial. It can be classify in two categories: (i) surface transfer doping and (ii) substitutional doping. The former is an adsorbate-induced doping and is achieved by electron exchange between graphene and dopants that are adsorbed at the graphene surface itself. In general it is a reversible process and does not destroy graphene structure. The latter refers to the substitution of carbon atoms in the honeycomb lattice of graphene by atoms with a different number of valence electrons such as nitrogen and boron. The incorporation of foreign atoms would disrupt the sp^2 bondings between carbon atoms in graphene. Moreover, interactions with the substrate, residuals chemical species and ambient air can induce involuntary doping [15].

This phenomenon of chemical surface transfer doping can be desired and induced in order to obtain a certain shift in the Fermi level of graphene, or it can be accidental.

Indeed, in contrast with theoretical graphene, experimental graphene always contains impurities, defects, interacts with the substrate, has edges and ripples. All these perturbations from the ideal graphene can alter the electronic proprieties inducing contaminations and chemical doping that shift the experimental Dirac point far away from its theoretical value [16], as also observed in our samples (for more details see paragraph 2.3.2).

1.1.2.2. From graphene to graphite

It has been shown that the electronic structure of graphene rapidly evolves with the number of layers, approaching the 3D limit of graphite at about 10 layers [17]. Only graphene and, with a good approximation bilayer-graphene present a simple electronic spectra, with a zero-gap semiconductor structure, while for three or more layers the spectra becomes increasingly complicated and conduction and valence band start overlapping [17].

It is then possible to identify single, double and few (3÷10) layer structure as three different kind of 2D graphene-like crystals, while structures with more layers can be considered as thin films of graphite.

In the case of the following experiment, graphite itself will be also used, as a reference

substrate. Indeed, the graphite structure consists in a superposition of planar graphene-like layers, weakly bound to each other through Van Der Waals forces. The hexagonal in-plane arrangement of atoms is then conserved, as well as the high in-plane mobility, while the out-of-plane mobility in considerably lower.

In our experiment we make use of a particular kind of graphite, know as Highly Oriented Pyrolitic Graphite (HOPG), which is obtained by heating hydrocarbons close to their decomposition temperature (~ 3300 K) and it is characterized by a higher degree of ordering than ordinary graphite, with an angular spread between the graphene sheets of less than $\sim 1°$. Graphene layers are perfectly planar in HOPG, while in graphite they can form microscopic randomly oriented domains, and this makes HOPG a better in-plane electric conductor than ordinary graphite [18].

Side and top view of HOPG are shown in *Figure 1.6* [18]. The distance between the nearest carbon atoms is again a = 1.42 Å, while the distance between graphene planes is d = 3.35 Å. Half of the carbon atoms in each plane are situated directly on top of an atom of the layer below, while the other half are located in correspondence of the centre of the hexagon of the layer below. The third layer is aligned with the first one, giving to this arrangement the name of ABA stacking.

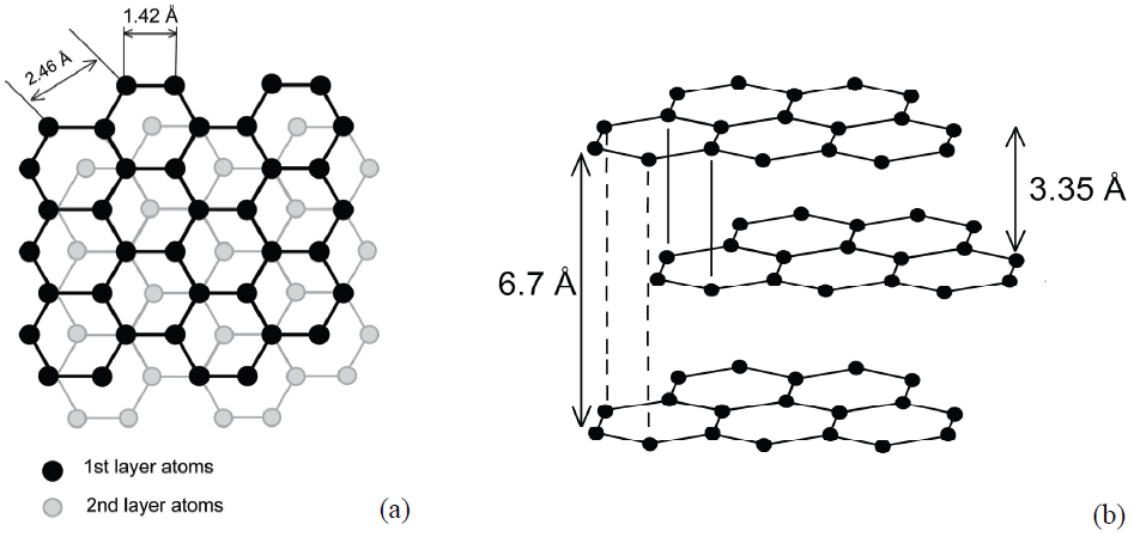

***Figure 1.6**: Top view (a) and side view (b) of HOPG structure. From Shriver et al. [18].*

1.2. Single molecule magnets: Co-phthalocyanine

Single Molecule Magnets (SMMs) consist in a class of molecules with an inner magnetic atomic like core and a surrounding shell of organic ligands. From a physical point of view, SMMs combine the classical macroscale properties of a magnet to the quantum properties of a nanoscale entity. Moreover, they offer crucial advantages over magnetic nanoparticles because they are perfectly monodisperse and so they can be studied in crystals.

A historically very important material in the development of SMMs is the Mn_{12}, studied by D. Gatteschi and R. Sessoli in the 90s [19].

SMMs presents a variety of shapes and sizes and allow selective substitutions of the ligands to alter the coupling with the environment. It is also possible to exchange the magnetic ions, thus changing the magnetic properties without modifying the structure. The magnetic properties of SMMs can be even affected when depositing on surfaces or between leads.

Finally it is interesting to notice that they display an impressive array of quantum effects, ranging from quantum tunnelling of the magnetization to quantum coherence, with important consequences for the physics of spintronic devices [20].

In the case of our experiment cobalt phthalocyanine molecules have been used as SMMs, they are a very simple type of molecular magnets belonging to the family of phthalocyanines.

1.2.1. Phthalocyanines

Phthalocyanines are a class of stable, blue-green organic pigments which can be synthesized with a variety of metal ions at their centre. They are related to molecules like heme and chlorophyll, and likewise show useful optical properties.

They where first synthesized between 1907 and 1927, and in 1928 they where first produced at industrial scale in form of crystals [21].

Phthalocyanine complexes are formed by synthetic organic macrocyclic compounds

consisting in isoindole[3] units linked together by four bridging nitrogen atoms.
They can be metal-free (H_2Pc) or they can have a metal atom (MePc) bounded to the four pyrrole nitrogen atoms (see *Figure 1.7*). The most commonly used MePcs contain one of the first row transition metals (TM) in the centre, but in total there are around 70 elements that can form phthalocyanine compounds [21].

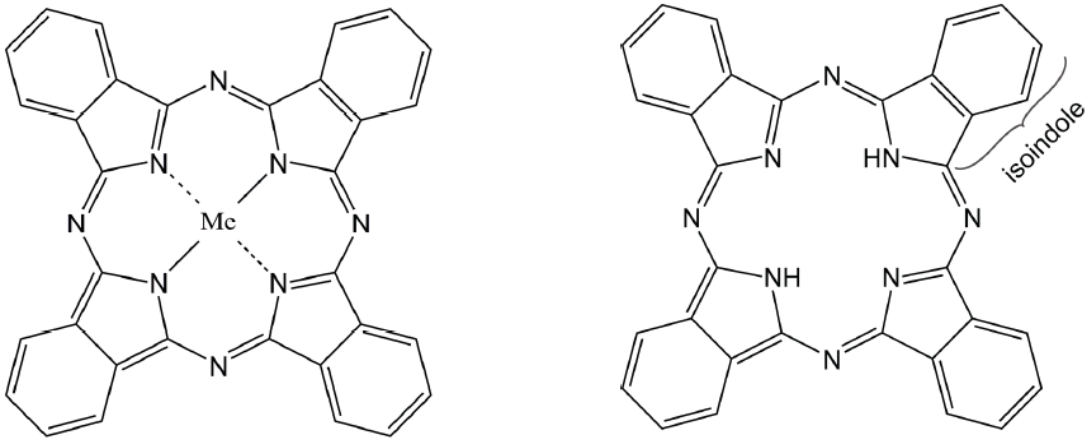

***Figure 1.7**: Molecular structure of metal phthalocyanine (MePc, $C_{32}H_{16}N_8Me$) and metal-free phthalocyanine (H_2Pc, $C_{32}H_{16}N_8H_2$) molecules.*

Phthalocyanines are planar molecules, except for a few cases such as the tin and the lead phthalocyanines (SnPc, PbPc), where the central metal ion is too large to be accommodated into the cavity and it lies outside of the macrocycle ring [22].
Macrocycles contain delocalized π bonds and have an aromatic character. As a consequence of the aromaticity, phthalocyanines exhibit interesting stability properties, such as: (i) high thermal and chemical stability, (ii) stability upon exposure to intense electromagnetic radiation. For example, phthalocyanines remain intact up to around 500°C and in some cases (such as cobalt-Pc, the one used in this experiment) the metal is so strongly bound that it can only be removed by breaking the macrocycle [23].
The properties of phthalocyanines are closely related to their electronic structure. In

[3] In chemistry, an isoindole is a benzene fused with a pyrrole. A benzene is a heterocyclic aromatic compound composed of six carbon atoms in a ring, with one hydrogen atom attached to each carbon atom and the molecular formula C_6H_6. While a pyrrole is again a heterocyclic aromatic compound, but with a five-membered ring with the formula C_4H_4NH.

particular, phthalocyanines containing certain transition metals (such as Cr, Mn, Fe, Co) present a quite complex electronic structure, with unpaired spins in the *d* valence band. The electronic and magnetic properties of phthalocyanines and phthalocyanines absorbed on a surface can be even modified (i) by changing the metal atom in the centre [24], (ii) by attaching different functional groups [25], (iii) by atom by atom manipulation [26], (iv) or by changing the support surface [27] as will be discussed in this thesis. Indeed, in the framework of spin manipulation it is very interesting to investigate the charge transfer and hybridization effects in metal-organic molecules adsorbed on different substrates.

1.2.2. Co-phthalocyanine

Cobalt phthalocyanine (CoPc) is a well known phthalocyanine molecule in which the central metal is Co^{2+}. It is particularly interesting as single magnet since it has been proved with experiments and theoretical calculations that in its ground state it presents a net magnetic moment localized on the cobalt *3d* orbitals, with spin $S = ½$ [28-29].

The central cobalt ion electronic configuration in the ground state is the essential quantity for understanding the magnetic behavior of the molecule, since it defines the total spin of the transition-metal ion.

The *3d* ground state of CoPc has been approximately known since twenty years ago [29], however uncertainties still existed regarding the role of excited states mixed into the ground states. Only in 2011 Stepanow *et al.* provide a definitive description of the molecular ground state at low temperature (~10K) by means of X-ray absorption spectroscopy (XAS) and X-ray magnetic circular dichroism (XMCD) experiments and ligand field multiplet calculations [28]. For more details about the experimental results in [28] we refer to paragraph 3.3.1.

According to Stepanow *et al.* a $3d^7$ configuration for the Co ion located in the centre of the molecule and a D_{4h} tetragonal crystal-field symmetry can be assumed.

Since phthalocyanine molecules have a four fold symmetry with a symmetry axis (taken as the z-axis) normal to the molecular plane, placing a transition-metal ion in the centre of the molecule results in a splitting of the formerly degenerate transition-metal *3d*

states. The splitting is due to the interaction between the ion and the surrounding ligand charges and depends on the symmetry of the molecule. The D_{4h} crystal field resulting from a distortion of the octahedral symmetry, causes a splitting into four levels, as shown in *Figure 1.8* [30]. The order of their corresponding energies depends on the strength and type of the distortion (squashing and elongation), as well as on possible hybridization effects.

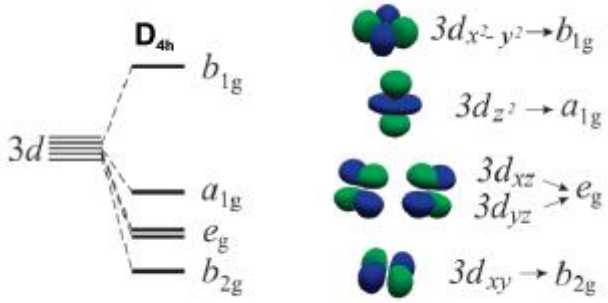

***Figure 1.8**: Schematic sketch of the metal 3d orbital splitting from the O(3) spherical symmetry to the D_{4h} symmetry. Adapted from Betti et al.[30].*

Stepanow *et al.* found that in the case of CoPc the many electrons ground state symmetry is $^2A_{1g}$, with the occupation of the individual *d*-state orbitals given by $(e_g)^4(b_{2g})^2(a_{1g})^1$ which is a low-spin configuration with $S = ½$ and the unpaired electron located in the a_{1g} (d_{z^2}) orbital. Since the first excited state (symmetry ^2E_g with corresponding configuration $(e_g)^3(b_{2g})^2(a_{1g})^2$) lies only ~80meV above the ground state, $^2A_{1g}$ and ^2E_g states are mixed by the spin-orbit coupling. This mixing partially depopulates the e_g orbital filling the half-empty a_{1g} and resulting in a final $(e_g)^{3.8}(b_{2g})^2(a_{1g})^{1.2}$ configuration. The depopulation of the e_g state even creates a finite orbital momentum in the plane of the molecule, indeed spin-orbit coupling removes the orbital moment quenching caused by the crystal field splitting.

1.2.3. Co-phthalocyanine interaction with a substrate

The magnetic properties of transition-metal (TM) compounds depend critically on the

competition between *d-d* electron correlation and covalency, that is the transfer of charge between *d*-orbitals and delocalized ligand states. Is it then clear the fundamental role of charge transfer (CT) in determining the electronic structure of MePc compounds. Recently, charge transfer process taking place at the interface between magnetic molecules, such as CoPc, and substrate surfaces has come under investigation. Indeed, in principle the CT process can happen between the central transition metal of the molecule and ligand orbitals, but also between molecular states and the electron reservoir of a metallic-like substrate.

Charge transfer process from the substrate seems strongly dependent on the central TM ion of the phthalocyanine molecule and on the electron affinity of the substrate.

In the case of CoPc, in particular, it has been noticed a strong influence of charge transfer process on the magnetism of the molecule.

Theoretical DFT (Density Functional Theory) calculations predict a non magnetic behavior, with spins $S = 0$, for CoPc adsorbed on Au(111) [31], Cu(111) [32], and ferromagnetic Fe (110) films [33]. This non-magnetic configuration is assumed due to a complete filling of the previously unpaired a_{1g} (d_{z^2}) state by means of electronic charge transferred from the metallic substrate.

From few years ago, some experimental results supporting this interpretation have been obtained. However they were only indirect measurements of the magnetic state of the molecule, based on the absence of Kondo resonances detected by Scanning Tunneling Microscopy (STM) [31-33], or spin-polarized STM measurements [34].

Only recently, X-ray spectroscopy techniques, such as X-ray magnetic circular dichroism (XMCD), X-ray absorption spectroscopy (XAS), and X-ray linear dichroism (XLD) have been used in order to investigate the electronic and magnetic structure of CoPc. These techniques are particularly advantageous because they allow a direct measurement of electronic configuration and local magnetic moments of the central TM ion in phthalocyanines.

Due to this notable advantage, these X-ray spectroscopy techniques are the ones also used in this thesis.

X-ray spectroscopy measurements form CoPc deposited on metal substrates, such as Au(111) [28], Au(110) [30] and Cu(111) [35], confirm the predicted quenching of the

magnetic moment associated to the central Co ion for a monolayer of CoPc deposited onto the metals surface.

This phenomena is explained as associated to fluctuations of charges between the *d* states of the CoPc molecules and the electrons of the metal substrate.

Chapter 2

CVD-graphene samples preparation and characterization

The graphene samples used in this experiment have been developed in collaboration with the research group of Dr. Vincent Bouchiat, at the NANOsciences department of the Institut Néel, CNRS, Grenoble. In the following chapter a detailed description of the samples preparation and characterization will be presented.
In the first paragraph, the choice of Chemical Vapor Deposition (CVD) instead of other techniques will be justified, then the CVD growth process of graphene will be introduced.
In the second paragraph, the actual fabrication and transfer of the graphene samples used in the following chapters will be explained in detail. Two different substrates have been used to support graphene flakes and the differences between the two systems will be discussed.
Finally, in the last paragraph, the samples morphology and electrical properties, studied by means of Atomic Force Microscopy (AFM), Scanning Electron Microscopy (SEM), Optical Microscopy, Raman spectroscopy and transport measurements, will be shown.

2.1. CVD growth of graphene

Chemical vapor deposition (CVD) is a vapor-phase synthesis technique for solid thin films deposition. Even before CVD graphene synthesis became common, CVD was

often used to grow silicon or silicon oxide thin films, and many laboratories also produced carbon nanotubes in this way [36].

The main idea of CVD is to flow gases, including synthesis precursors and sometimes inert compounds, into a heated chamber where they react with each other as well as with the substrate, resulting in the desired material being deposited on the substrate.

The chemical reaction plays a fundamental role in CVD and this is one of the most distinctive features compared to other film deposition techniques, such as physical vapor deposition (PVD).

In the case of graphene, the reagents are methane (CH_4) and hydrogen (H_2). The deposition can be divided into two parts: (i) precursor pyrolysis to carbon and (ii) formation of graphilitic structure from dissociated carbon atoms. As far as it concerns the substrate, in principle a lot of different metals could be used, however copper is nowadays preferred as it solves the problem of having a large-area and good-quality graphene samples [37], as it will be shown in the next paragraphs.

2.1.1. Why CVD ?

CVD is not the only possible technique for graphene growth. Due to the increasing interest in graphene and its possible applications, a lot of effort has been put into developing and improving synthesis processes during the last few years. There are currently three main procedures for obtaining a good quality single layer of graphene. The following will briefly review their main characteristics.

The first procedure is the well-known micromechanical exfoliation or "scotch-tape technique", introdced in 2004 by Novoselov and Geim [4]. An adhesive tape is used to repeatedly peel layers of a bulk graphite sample in order to eventually produce single layer graphene samples. This procedure is based on the relatively strong σ-bonds between carbon atoms in graphite planes compared to the weak interplanar π-bonds. Graphene samples obtained in this way present very high electronic quality (mobility $\mu \sim 15000\ cm^2V^{-1}s^{-1}$ at room temperature on SiO_2/Si^{++} wafers [38]), but they are limited in size (usually < 1000 μm^2 [37]).

A way to avoid this dimensional problem is the direct growth of graphene on a substrate which is the second procedure to grow graphene. Several synthesis techniques exist, such as (i) graphitization of a SiC (0001) wafer, where the crystal is heated to 1200˚C in order to desorb Si atoms located near the surface, leaving a mono or multilayer graphene structure that behaves like graphene [39-40], or (ii) epitaxial growth of graphene on single crystals [41-42].

Recently a new process have been developed, consisting of growing graphene on copper foils by chemical vapor deposition [37]. This is currently the third procedure for preparing graphene (which is called CVD-graphene to distinguish it from the exfoliated one). Samples obtained in this way present large areas, in the order of centimeters, and they are mainly monolayers, with less than 5% of the area having two or three layer graphene flakes [37]. Another important advantage is the possibility of etching the copper foil and transferring the sample onto a different substrate. A drawback of this technique concerns electric properties, as the mobility obtained is still much lower than that reported for exfoliated graphene ($\mu \sim 4000$ $cm^2V^{-1}s^{-1}$ at room temperature on SiO_2/Si wafers [37]), however there is currently a great deal of research in this field.

In *Table 2.1* properties of graphene samples obtained by the three procedures are summarized.

Method	**Number of layers**	**Size**	**μ ($cm^2V^{-1}s^{-1}$)**	
Exfoliation	1 ÷ 10	100 μm	15000	[38]
Graphitization SiC	1 ÷ 4	1 cm	10^3 - 10^5	[39]
CVD	1	10 cm	$\sim 10^3$	[37]

***Table 2.1**: Comparison of graphene synthesis methods. Some typical values are reported, in particular the number of layers produced, the size of graphene layers and their mobility when placed on a SiO_2/Si^{++} wafer at room temperature.*

Which kind of graphene is the most suitable for this type experiment? As X-rays measurement techniques will be used, with a beam spot size of about (1.5 × 0.5) mm^2, exfoliated graphene does not fulfill the dimension requirements, since the flakes are smaller than the beam size.

Graphene grown on SiC is also not a good choice, because of the thickness of the

underlying crystal that does not allow field effect experiments to be performed.
On the other hand, CVD-graphene grown on copper and then transferred onto a dielectric substrate satisfies both the needs of having a large area sample and being able to apply a gate voltage, and is therefore the most suited for this experiment.

2.1.2. A brief insight in CVD-graphene growth process

Before explaining in detail the fabrication of single layer graphene samples by means of CVD, it is interesting to focus on some of the physical details of the process itself, which are explained in the following.

- **Importance of the copper substrate:**

First of all, it is necessary to explain why the introduction of copper as a substrate has been a major breakthrough in the fabrication of good quality CVD-graphene samples.
Not all materials can be chosen as substrates for the CVD process, as they have to behave as catalysts for the chemical reaction. Their first function is to lower the energy barrier required for the reaction. For obtaining large area graphilitic structures without catalysts, it is in fact necessary to reach temperatures beyond 2500 °C, which are too high for the conventional experimental setup.
Moreover, in the case of graphene, the catalysts ensure the reaction to be heterogeneous[4], implying that the precursors only react at the substrate surface without precipitation of carbon clusters from the gas phase. The latter process would form carbon soot and sits on the synthesized graphene with an amorphous structure no longer retaining the proprieties of monolayer graphene. To obtain a heterogeneous reaction at the surface, it is necessary to use an opportune catalyst.
Different materials can be used as catalysts for CVD-graphene growth, they are usually

[4] It is possible to distinguish between homogeneous and heterogeneous reactions. In the first case, the reaction takes place in the gas phase, only the precursors are involved and there is no interaction with the substrate; in the second case instead, the reaction takes place at the substrate surface, which is directly involved in the process.

metals with a certain degree of carbon solubility. In particular, nickel[5] has a non-negligible carbon solubility [44], whereas carbon solubility in copper is almost zero [45]. Carbon solubility phase diagram are shown in *Figure 2.1* for Cu and Ni [46].

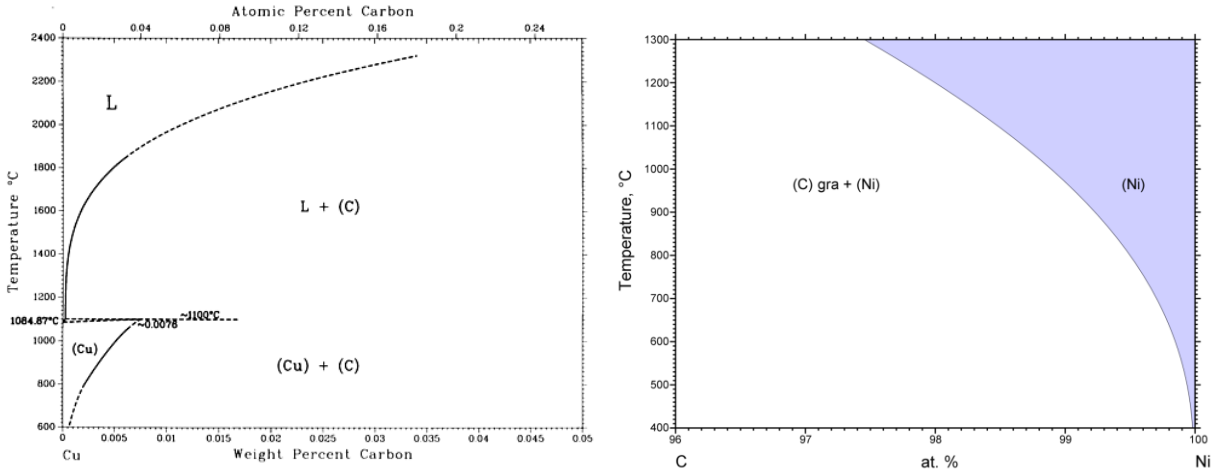

Figure 2.1*: Carbon solubility phase transition in units of weight percent for copper (left) and nickel (right). The carbon solubility at the melting point of copper (1085°C) is only 0.0076%. The low solubility of carbon is a common feature of the noble metals. On the other hand the carbon solubility at the melting point of nickel (1455 °C) is 0.6%. Even at the temperature of 1085 °C, the solubility is still orders of magnitude higher than in copper. A similar behavior is observed in other transition metals. Copyright ASM International.*

These different values of solubility are the turning point in understanding the reason why CVD on copper produces a single layer graphene, while on nickel generates a more disordered multilayered graphene.

In the case of nickel, carbon has a high solubility at the operation temperature of the furnace (1000 °C), so that when the precursor decomposes into carbon ad-atoms on the Ni surface they soon dissolve into the bulk. Upon sample cooling to room temperature (cooling step, see paragraph 2.2.2) the Carbon solubility is also reduced as it is a temperature-dependent property, thus the dissolved carbon atoms in excess are forced to

[5] Nickel has an important role in the development of CVD-graphene growth, since it has been the first metal used as a substrate in this technique [43]. It is discussed here for comparison with copper.

precipitate back onto the top surface (dissolution-precipitation mechanism) where they form graphene sheets. The thickness of graphene is therefore controlled by the difference between the carbon solubility in Ni at the deposition temperature and at room temperature, and by the cooling rate. In fact, when cooling is performed in an out-of-equilibrium regime it is possible to vary the coverage thickness: extremely fast cooling leads to little carbon precipitation, because carbon does not have sufficient time to precipitate; medium cooling produces graphene growth and slow cooling leaves nothing at the surface because carbon atoms diffuse deep into the bulk catalyst. A scheme of the process is shown in *Figure 2.2* [47]. The scheme suggests that the growth of a single layer graphene is very challenging to control.

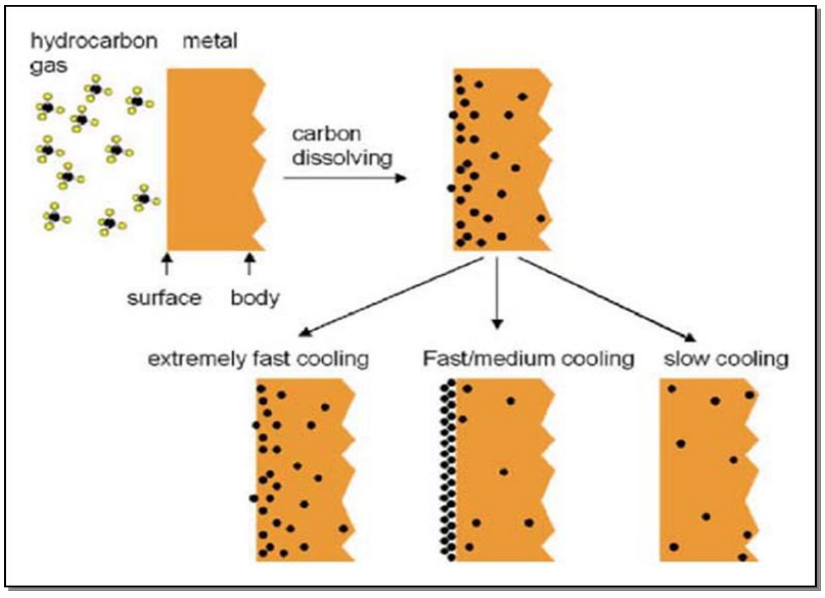

***Figure 2.2**: Illustration of carbon segregation at the metal surface. Yu et al., 2008 [47].*

In the case of copper, instead, thanks to the very low carbon solubility even at 1000 °C, the amount of atoms dissolved in the bulk is not enough to significantly affect the growth process. As a result, the dissolution-precipitation mechanism is negligible for Cu. Graphene sheets are directly formed by graphitization of carbon ad-atoms at the surface. This mechanism suggests easier control over the deposition and even the cooling rate at the last step does not affect the graphene thickness.

In that way, copper is considered a better catalyst for CVD-graphene production.

However, as Cu is a metal more reactive than Ni, steps must be taken to avoid the oxidation process: the pressure in the furnace should be lower than the one used in the case of nickel, and the sample should not be extracted from the CVD-system when still a high temperature.

- **Graphene growth as a self-limiting process:**

Another important advantage of CVD-graphene is that the growth is a self-limiting process. This means once a graphene sheet has been deposited on the catalyst surface, the "catalyst-poisoning" effect takes place. The substrate loses its catalytic behavior once completely covered by the first layer of graphene which then protects from future interactions with the precursor species. In effect the growth automatically stops after the first layer synthesis.

In principle the first graphene layer could act as a catalyst for the second but as graphene is a less efficient catalyst, the energy required to grow the second layer would become so large as to make the process negligible.

It is important to stress the fact that small patches of double or triple layer graphene can however be found if the deposition time is quite long. The process of formation of graphene multi-layers on Cu is still under debate [48].

- **Annealing:**

It is also interesting to point out that the annealing of catalysts it is not only necessary in order to reach the temperature of activation of the reaction, but also useful to reduce their surface roughness and enlarge the grain sizes of the crystal.

When carbon atoms arrive on the substrate surface, they tend to stay in regions with a higher surface energy, such as defects, grain boundaries and surface trenches. These points present more dangling bonds, they are more reactive thus producing a non uniform carbon deposition. In order to reduce this effect, it is important to pre-anneal the substrate to reduce grain boundaries and defects and obtain larger grains. In fact, the less grain boundaries and defects the catalytic substrate has, the more homogeneous the derived graphene will be.

- **Addition of inert gases:**

Finally, a variant to the procedure consists of using a mixture of gases containing both hydrogen and argon, H_2(90%) and Ar(10%), instead of hydrogen alone. Of course it is a safer solution, as hydrogen alone is highly explosive. Furthermore, the addition of a non reactive gas allows the deposition to be performed at a higher pressure, simplifying the instrumental setup, without increasing the probability of depositing contaminations or doping agents from the atmosphere on graphene. Argon atoms, having high atomic number (18), impact on the substrate transferring a large amount of energy, encouraging the diffusion of carbon ad-atoms on the surface and preventing the formation of defects and second layers.

2.2. CVD growth and transfer of large scale graphene flakes for synchrotron radiation studies

CVD is a very complex process and a deep understanding of the minute details of graphene growth in the different stages is still missing. As a result, a trial-and-error method is commonly used to deduce good "recipes" and try to improve them in order to define a well reproducible way to obtain large area and good quality graphene samples.
In the following paragraphs the experimental setup and the exact procedure used for the experimental samples will be described.

2.2.1. Description of the CVD experimental apparatus at NANOsciences

The CVD tube-furnace used for growing our samples was suitably developed in the NANOsciences department of the Institut Neel, CNRS, Grenoble.
Figure 2.3 shows a schematic drawing of the CVD system. The four main components are distinguishable:

- a gas delivery system
- a reactor
- a gas removal system
- an auto-control unit

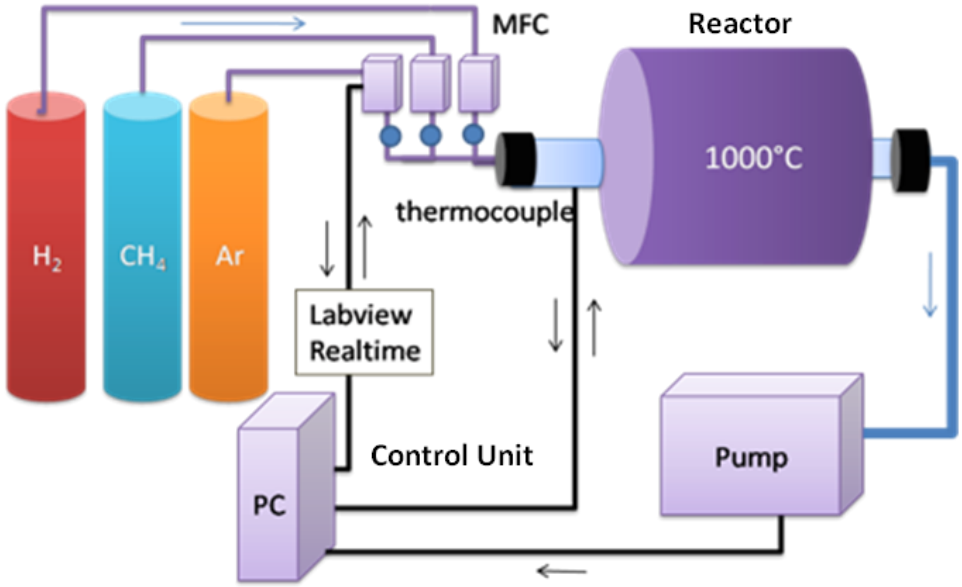

***Figure 2.3**: Schematic diagram of the tube-furnace CVD system at NANOsciences. Gas flows are regulated by MFCs, and fed into the reactor through a gas-distribution unit. Chemical deposition takes place in the reactor that is heated by the outside heaters. The exhaust gases are removed by vacuum pumps. All the process is automatically controlled by the auto-control unit.*

During the CVD process, reactive gas species are fed into the reactor by the gas delivery system consisting of (i) valves, called Mass Flow Controllers (MFCs), controlling the flow rates of the gases passing through them, and (ii) a gas-mixing unit responsible for mixing the various gases uniformly before they are inserted in the reactor.

The reactor is where the chemical reaction takes place and the solid materials are deposited on substrates. Heaters are placed surrounding the reactor, to provide high temperatures for the reaction.

Finally the by-products of the reaction and non-reacted gases are removed by the gas removal system made of one or more pumps, regulated by specific pressure control

valves.

All inputs and outputs, such as temperature reading and pressure adjustment, are interfaced by a homemade Labview programme through an auto-control unit.

In *Figure 2.4* is it possibile to see how the NANOsciences CVD system looks in reality.

Figure 2.4 *CVD system at the NANOscience department of the Istitut Néel, Grenoble.*

2.2.2. CVD-graphene growth on copper foils

CVD is not an easy-to-control process. Many different parameters have to be taken into account, not only temperature, pressure, time and so on, but also the transport kinetics of gas species, dominated by mechanisms of convection and diffusion.

Even the chemical reaction itself can be very complicated, because it usually involves many intermediate steps and the exact step-by-step reaction process may not be known, as is the case for graphene. The process by which CH_4 molecules are thermally decomposed is still not absolutely understood because of the intermediate steps in CH_4

pyrolysis. A possible dissociation path of CH_4 could be CH_3-CH_2-CH-C by means of subsequent losses of hydrogen atoms.

To better explain the complexity of controlling the CVD growth, *Figure 2.5* [49] shows an example of the strong dependence of CVD graphene growth on process parameters. In the four Scanning Electron Microscopy images it is possible to distinguish typical "flower-shaped" graphene grains growing on the copper substrate. The shape and dimension of the grains strongly depends on the process parameters.

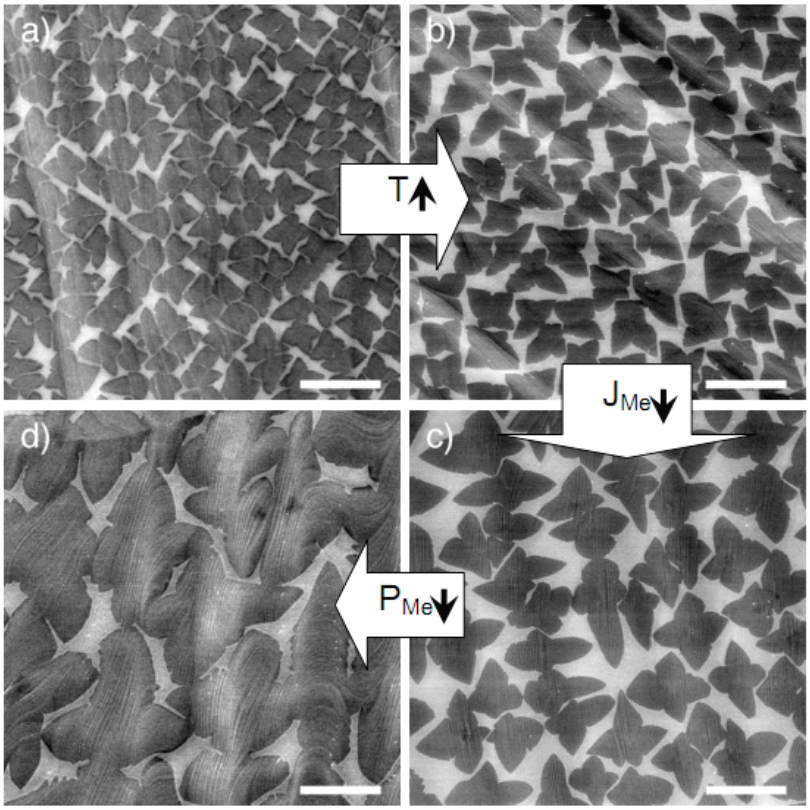

***Figure 2.5**: Scanning Electron Microscopy (SEM) images of CVD graphene on copper. The effect of temperature (T), methane flow (JMe) and methane partial pressure (PMe) on the graphene domains size is shown. Scale bars are 10 µm (from Li et al., [49]).*

Therefore, in order to obtain good quality samples with high enough reproducibility, a well known copper-foil graphene CVD synthesis recipe has to be followed during samples preparation. Historically, the first "recipe" was developed by Li *et al.* [37] in 2009. Since then a lot of work has been done in trying to optimize it, in order to obtain

graphene with better structural and electronic proprieties. Many slightly different variants of this procedure exist. In this experiment the method developed by the Bouchiat group in 2011 [48] has been used.

Graphene is grown on a copper foils at temperatures up to 1000 °C by CVD of carbon using a mixture of methane and hydrogen. The exact procedure can be summarized in four steps:

- copper foil preparation
- furnace preparation
- Cu foil annealing
- graphene growth

First of all, a poly-crystalline copper foil (Alfa Aesar, 99.98 % purity, 25 μm thickness) is cut into the desired size (roughly 8 cm × 10 cm) and cleaned with nitrogen blow. Cut foils are then put onto a rectangular quartz substrate holder, and inserted in a quartz tube (the reactor of the CVD furnace).

Once the copper foils have been mounted, the reactor is evacuated using a scroll pump. It is very important to have a good vacuum, because gas leaks, especially oxygen, can damage graphene growth and even cause explosions, due to the presence of hydrogen in the chamber. The reactor should be pumped down, until a vacuum of about 1 mbar is achieved. After opening the corresponding cylinder the hydrogen flow is set to 100 SCCM[6] by the corresponding MCF. This results in a small increase in the tube pressure, compensated by the feedback loop of the control unit itself which is in turn regulated by Proportional-Integral-Derivative (PID) parameters.

The furnace is now ready for the deposition, but it is still necessary to anneal the copper foil. For this purpose the furnace lid is clamped and the heater system set to 1000 °C. It takes about 1.5 hours to reach this temperature. PID parameters are continuously adjusted to maintain constant the pressure in the chamber, compensating for fluctuations due to gases desorbed from the quartz tube, substrate holder and copper foil. Once the temperature is reached, the foil should be annealed for at least 30 minutes, this will help

[6] SCCM is an acronym for Standard Cubic Centimeters per Minute used here as gas flow unit.

to clean the foil itself as well as to increase the size of crystal grains (as discussed in paragraph 2.1.2).

When the annealing is complete, the methane MFC is set to 2 SCCM for about 60 minutes at a total pressure of 1 mbar that leads to the growth of graphene.

Once the desired growth has been achieved, the heating of the furnace can be stopped in order to start cooling down the system to room temperature.

All deposition parameters, such as temperature, gas flow rate and reaction time are summarized in *Figure 2.6* [48].

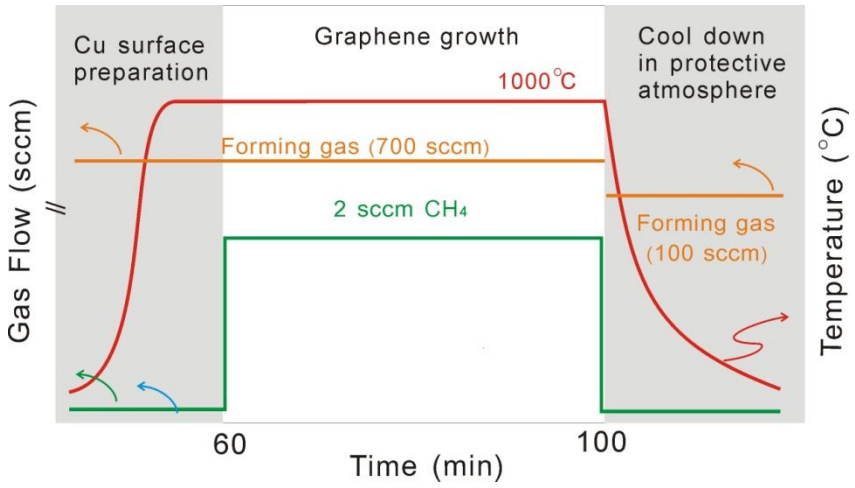

***Figure 2.6**: Procedure for CVD-graphene synthesis on copper foil, as developed by the Bouchiat group at NANOsciences department [48].*

After cooling the pumps can be stopped and the system vented. The MFCs are turned off and, when the substrate holder is cold enough (roughly at room temperature), it is removed with a clean rod to avoid contaminations of the furnace.

The copper foil is placed horizontally into the furnace, the upper side being directly exposed to the gas reactants flown into the chamber. The lower side of copper foil is instead in close contact with the underneath quartz support, which protects it from reacting with synthesis precursors. Therefore the copper foil is covered by graphene on the upper side only[7]. It is even possible to see "by eye" the difference between the two

[7] Actually, a small amount of graphene islands can be deposited even on the lower side of the copper foil, as will be better explained in the following paragraphs.

sides; the upper side (Cu + graphene) is bright and shiny, as shown in the right side of *Figure 2.7*, and should not lose its luster, as graphene doesn't react with oxygen, behaving as an oxidation-resistant coating. The bottom side instead is less shiny and will be subjected to oxidation process if left in air, as shown in the left side of *Figure 2.7*.

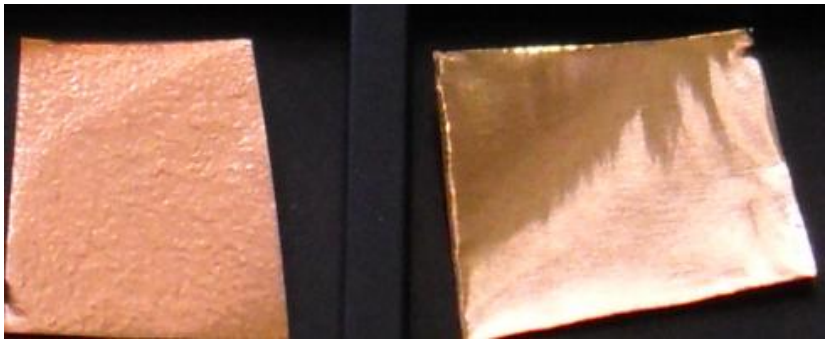

***Figure 2.7**: Comparison between copper foils without (left side) and with (right side) CVD-graphene growth. Once deposited on Cu, Graphene behaves as an oxidation-resistant coating, leaving a bright and shiny surface. Images are taken from samples prepared at NANOsciences.*

2.2.3. CVD-graphene transfer on SiO_2/Si^{++} and $SrTiO_3$

The graphene samples obtained so far are deposited on a metal substrate. As the goal of this experiment is to measure graphene resistance and field effect in order to know the level of doping in the samples, this configuration does not satisfy the experimental requirements. In fact, every electrical current flowing through the graphene would be shorted by the conducting substrate. It is therefore necessary to remove the catalytic metal and replace it with a more suitable substrate. The possibility of doing that, is another important advantage of CVD-graphene growth.

In our experiments two different substrates have been used: SiO_2/Si^{++} and $SrTiO_3$. Most of the measurements have been performed using SiO_2/Si^{++} substrates, which are very common in the field of electric transport. Some preliminary measurements have been done using $SrTiO_3$ as a supporting substrate. This is a common dielectric material used

in combination with superconductors, but until now has never been used together with CVD-graphene.

Our interest in different substrates is due to experimental evidence that the substrate itself could have an influence on the electronic and morphologic proprieties of graphene [30]. Before describing the transfer process, it is useful to present a short description of the main physical proprieties of the two substrates.

- **SiO_2/Si^{++}**

Si wafers with an oxidized dielectric SiO_2 layer on the surface are widely employed in electronic devices. In particular, in the case of devices based on the electric field effect, SiO_2 is the gate oxide, whereas highly electron doped Si[8] is the back gate electrode. SiO_2/Si^{++} is often fabricated by doping the back side of a Si wafer with B or N, and oxidizing the top side of the wafer. Nowadays, many different and sophisticated fabrication techniques exist, due to the wide diffusion of this material in the production of electronic components.

In the case of graphene devices, the use of SiO_2/Si^{++} is mainly due to historical and practical reasons. Indeed, the critical ingredient for graphene production success was the observation that a single layer of graphene becomes visible under an optical microscope if placed on top of a SiO_2/Si^{++} wafer with a carefully chosen thickness of SiO_2, due to a feeble interference-like contrast with respect to a wafer not covered by graphene. Without this very simple, yet effective way of scanning the substrate in search of graphene flakes, the latter would probably have remained undiscovered since today [4].

As already seen in the first chapter, is it possible to change the density of carriers in graphene inducing a chemical or electrical doping. When a gate voltage V_g is applied to a device made of graphene deposited on a SiO_2/Si^{++} wafer, it can induce a charge density of the order of about 10^{12} cm^{-2} with a gate voltage of several tens of Volts.

It is possible to estimate the amount of charge carriers per unit surface area *n* induced at

[8]Semiconductor doping has the utility of changing the Fermi level position. For intrinsic semiconductors no doping effect is present and the Fermi level stays more or less in the centre of the energy gap. For degenerate semiconductors instead the doping is so high (in the order of 10^{18} carriers / cm^3) that the Fermi level enters in the conduction band (in case in electron doping) or in the valence band (in case of hole doping) and the semiconductors behave like a metal.

the graphene surface with the relation:

$$n = \frac{\varepsilon_0 \cdot \varepsilon_r \cdot V_g}{t \cdot e} \tag{2.1}$$

where ε_0 is the vacuum permittivity ($\sim 8.85 \times 10^{-12}$ F/m), ε_r is the relative dielectric constant of SiO_2, e is the electron charge, and t is the thickness of the SiO_2 layer.

In this experiment, the silicon wafers were 0.5 mm thick, with a 300 nm SiO_2 layer at the surface. The relative dielectric constant of SiO_2 is $\varepsilon_r = 3.9$ at room temperature, and can be considered approximately constant with temperature [38]. With these values, a density of carriers in the order of 7.2×10^{12} cm^{-2} can be obtained by applying a gate voltage of $V_g = 100$ V at the sample.

The linear relation between density of carriers and gate voltage, as verified experimentally by Novolesov and Geim in 2004 [4], is reported in *Figure 2.8*.

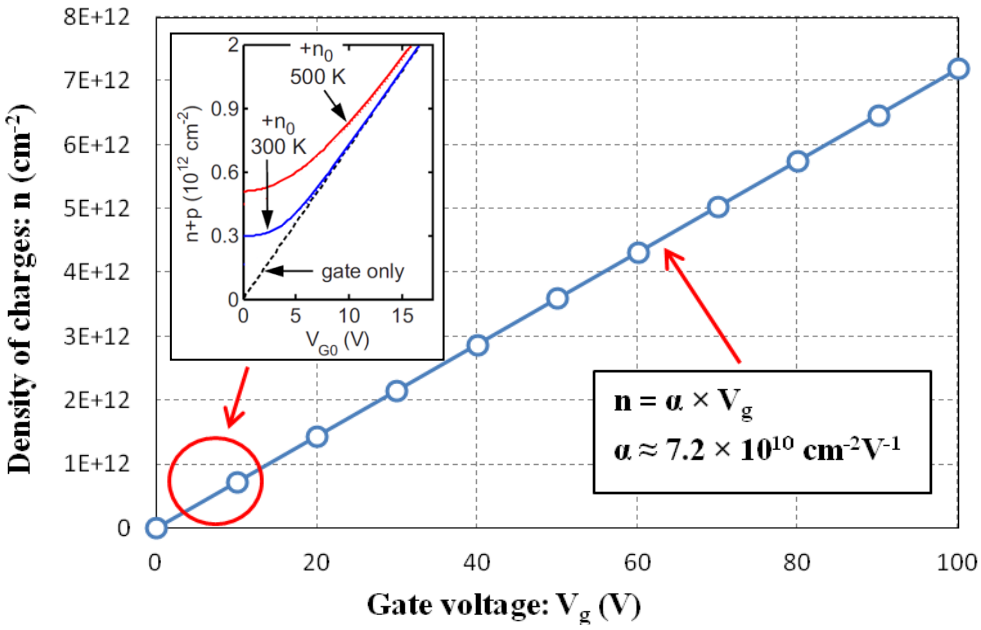

***Figure 2.8**: Schematic plot of the relation between density of charges and applied gate voltage in graphene/SiO_2/Si^{++} devices with 300 nm thickness of the oxide. The insert shows calculated charge density as a function of gate voltage at 300 K and 500 K (Dorgan et al., 2010 [50]), solid lines include contribution from thermal generation and defects, dashed line shows only the contribution from the gating.*

The linear and temperature independent approximation fits particularly well away from the Dirac point. At the Dirac point *n* should theoretically vanish [3], but thermally generated carriers and electrostatic spatial inhomogeneity limit the minimum charge density, as shown in the insert of *Figure 2.8* [50].

It should be stressed that this approximated relation (2.1) only gives an estimation of the number of carriers. The only way to carefully measure the number of electrons taking part in the transport is to do Hall Effect measurements [4].

One of the drawbacks of using SiO_2/Si^{++} is the fact that a very high quality of these substrates is required in order to avoid the dielectric breakdown. Indeed, in these wafers there are always defects, which can lead to the breakdown at a certain applied gate voltage, as they create a leak current between the graphene sample and the back gate.

As observed during the experiment, the breakdown voltage changes from wafer to wafer. Good quality SiO_2/Si^{++} wafers can present a breakdown voltage as high as few hundreds of volts, but generally it is not possible to apply more than ~ 100 V. However, applying hundreds of volts can still not be sufficient to reach the Dirac point in case of the heavily doped graphene. Indeed, in the case of large flakes of CVD-graphene, graphene sometimes was so doped to have the Dirac point shifted even far beyond the range of ±100 V.

Another significant problem to consider, specific to our setup, are the effects induced by ionizing radiation on SiO_2. Indeed, radiation-induced interference charge traps can slightly modify the gate voltage and the charge transfer seen by graphene [51]. In this experiment it have been observed that this phenomenon does not affect significantly the experimental results, since the time constant of the graphene resistivity variation due to ionizing radiation is much bigger than the measurement time. Within the time of an experiment the resistivity variation due to ionizing effects was of the order of ~ 1% of the resistivity variation induced applying a back gate of less than 40 V to the sample.

Figure 2.9 shows a plot of the attenuation length[9] of X-rays in SiO_2 as a function of the incident radiation energy.

[9] The attenuation length is defined as the depth into the material measured along the surface normal where the intensity of x-rays falls to 1/e of its value at the surface.

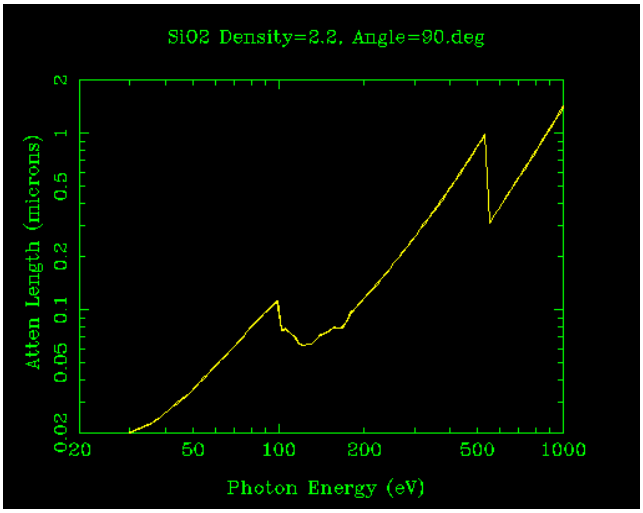

***Figure 2.9**: Attenuation depth of X-rays in SiO_2 as a function of the radiation energy. With the standard notation for the x-ray region the incidence angle is measured relative to the surface (not the surface normal).*

From *Figure 2.9* is clearly visible that at the cobalt absorption edge (~780 eV), the attenuation length is roughly 1 micron, which corresponds to the penetration depth of X-rays in this material. Therefore the oxide layer in our samples completely absorbs the incident X-ray radiation.

- **$SrTiO_3$**

Strontium titanate is an oxide of strontium and titanium, commonly used as a substrate in high temperature superconductor devices and has only very recently been used in exfoliated graphene devices [52]. $SrTiO_3$ has a perovskite structure and can be grown as a single crystal. In this experiment graphene has been deposited on the (100) face of $StTiO_3$ which presents a very smooth surface, with 4 Å thick atomic steps, spaced by about 100 nm. Samples have been produced by the company SurfaceNet GmbH and their dimensions were 10 mm^2 surface area × 0.5 mm thickness.

One of the main advantages of using $SrTiO_3$ is the extremely high relative dielectric constant. In particular, $SrTiO_3$ presents a transition from a paraelectric to a ferroelectric behavior at low temperature, that causes the relative dielectric constant of the materials (ε_r) to increase from 200 ÷ 300 at room temperature, to ~ 5000 at liquid helium

temperature, with most of the increase taking place when the temperature is lowered from 50 K to 10 K [53].

In that way, it is possible to accumulate a good deal of charge on the surface of graphene using very small gate voltages. In particular, at low temperatures a greater surface density of charges can be achieved in comparison to the SiO_2/Si^{++} for the same gate voltage.

It has also been proved that although a lowering in the temperature induces a large increase in the dielectric constant, the graphene conductivity remains temperature independent, confirming what seen with SiO_2/Si^{++} substrates [52].

Another important advantage of using $SrTiO_3$ is that it is possible to apply back gate voltages of the order of 900 V without reaching the dielectric breakdown, accumulating at least 10^{13} charges/cm^2 at the substrate surface.

The dielectric constant of $SrTiO_3$ does not depend only on temperature, but also on the electric field. In particular, at a working temperature of ~ 10 K, it has been calculated that ε_r rapidly decrease from ~ 5000 to ~ 2000 with an applied back gate up to 20 V and it reduces down to a value of ~ 1000 with the maximum gate voltage applied (of the order of 900 V) [54].

The biggest disadvantage of $SrTiO_3$ compared to SiO_2, is the difficulty of seeing graphene deposited on it under an optical microscope. On a substrate with only one face polished (as the ones used in this experiment), an optical contrast of only 1.25 % has been measured for a monolayer graphene [52].

2.2.3.1. CVD-graphene transfer on SiO_2/Si^{++}

The procedure used for CVD-graphene transfer on SiO_2/Si^{++} is based on the improvement of the first "recipe" developed by Li *et al.* in 2009 [37] as also described in Han *et al.* [48]. In the following, the full technique is discussed in detail.

The procedure must be performed in a very clean and controlled environment, such as a clean room, in order to avoid contamination and damage of the very delicate graphene samples.

The procedure can be divided into seven steps:

- PMMA spin coating on graphene
- Oxygen plasma etching of the back side of the copper foil
- Chemical etching of the copper foil
- Solvent residuals removal from PMMA/graphene
- Cleaning of the SiO_2/Si^{++} substrates
- PMMA/graphene deposition on the substrate
- PMMA removal

In *Figure 2.10* a schematic view of the most important steps is reported.

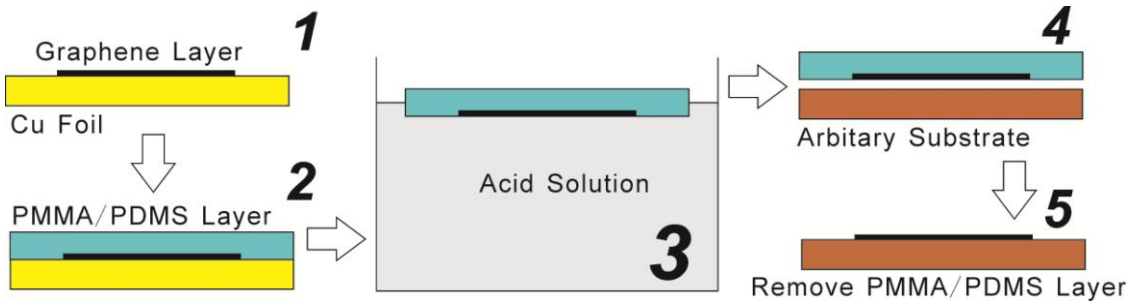

***Figure 2.10**: schematic view of graphene transfer process.*

- **PMMA spin coating on graphene**

As we need to separate graphene from the metal substrate, it is necessary to remove the copper. This is done by means of a not too strong, in order not to damage graphene, yet efficient solvent. The tricky point is that graphene is a single atomic layer, so it is not possible to simply remove copper and leave the flake floating in the solvent, since it would curl up and it would not be possible to transfer it any more. In fact, besides increasing visibility and facilitate handling, the supporting layer is necessary as bare graphene may collapse due to surface tension.

So, the graphene layer has to be protected. In order to do so, a polymer (usually PMMA[10] or polystyrene) is spin coated onto the graphene/Cu foil, according to the

[10] PMMA is an abbreviate form for Polymethylmethacrylate, it is a transparent thermoplastic often used as a light or shatter-resistant alternative to glass.

following procedure.

First of all, a pair of acetone cleaned and highly precise scissors should be used to remove the parts of the graphene/Cu foils that present more defects, damages and wrinkles, otherwise the polymeric coverage will not be uniform. At this point it is important to be very careful not to touch the sample surface covered by graphene. The foil can be held gently by one corner with tweezers or by the back side with gloves.

Once the sample is ready, it is possible to perform spin coating. Always touching only corners by tweezers, the sample is deposited, as flat as possible, on the spinner of the spin coating machine. There is a small hole located in the centre of the spinner and connected to a pumping system. Upon applying vacuum the foil is strongly attached to the spinner without getting damaged, except for the formation of some wrinkles in the region in direct contact with the hole. A low rate N_2 gas flow directed vertically to the surface can be used to eventually remove dust residuals. Then the polymer, in the case of this experiment PMMA 4%, is deposited on the sample. A tiny pipette should be used to obtain a very uniform coverage all over the graphene layer. Attention must be paid not to have the polymer running over onto the backside. If the PMMA coats both sides of the square, the etchants will not work as they cannot penetrate PMMA and the copper foil will not be removed. Spin coating is performed at 3000 RPM for 30 seconds.

PMMA/graphene/Cu samples obtained in this way should be baked on a hot plate at 180 °C for 1 minute in order to dry the polymer.

- **Oxygen plasma etching of the back side of the copper foil**

Before etching the copper foil another important step should be done. During the process of CVD growth, a single layer of graphene is supposed to be deposited only on the top face of the copper foil (see paragraph 2.2.2). However, if the foil does not perfectly stick on the quartz support located inside the CVD furnace system, some carbon atoms will be deposited even on the back side of the copper foil, forming some randomly distributed graphene islands. Once the copper foil has been removed by the etchant, these islands may collapse on the single layer graphene previously grown on the other side of copper. In that way, there will be formation of some double layer regions and defects, lowering the graphene quality.

To prevent this problem, the back face of the copper foil can be polished using plasma etching. The PMMA/graphene/copper sample is placed upside-down in the plasma etching machine. The graphene monolayer, being protected by PMMA, will not be damaged when put in contact with the smooth surface of the plate of the plasma etching machine. After evacuating the chamber down to 10^{-5} mbar, oxygen gas is injected in the chamber. The O_2 gas is ionized in a vacuum system by using RF excitations, at the operation frequency of 13.56 MHz at 50 mWatt, as chosen by the Federal Comunications Commission (FCC) for industrial and scientific use. Ions from the plasma are then accelerated by a voltage towards the target substrate. In this way, the copper foil is bombarded by high energy ions and their energy can be selected by setting the gate value. The sample should be left in the plasma etching machine from 3 to 5 minutes. Residual carbon ad-atoms on the back side of copper will be completely removed, while the desired single layer of graphene will not be affected, since the oxygen ions bombard the target vertically and the copper foil is too thick to be significantly damaged by the plasma.

- **Chemical etching of the copper foil**

It is now possible to cut the PMMA/graphene/copper foil into smaller squares and dip them into the etchant. The cutting procedure should be done using the same precautions already explained at the beginning of the paragraph. For experimental purposes, a good square dimension is about 4 mm × 6 mm. Smaller samples would be very difficult to cut without creating a lot of wrinkles, whereas bigger samples would be very difficult to transfer on the new substrate.

PMMA/graphene/copper squares should now be put into a beaker with the etchant. PMMA has to be on the top, in order to improve the contact between copper and solvent and increase the efficiency of the etching, while graphene is stuck to the underside of it.

- **Solvent residuals removal from PMMA/graphene**

Now it is necessary to clean the PMMA/graphene from any residuals of the solvent, otherwise the samples could present Cu impurities and dopants. Then PMMA/graphene

is transferred onto the selected substrate and finally PMMA will be removed.
Two different procedures are possible in order to remove any etchant residuals. One is "safer", while the other one is "faster". In the following both will be presented:

- In the "safer" procedure, two clean and tiny pipettes, a big beaker full with de-ionized (DI) water and two empty beakers are required. The DI water is used to progressively dilute the solvent, in a many step procedure.
  In the first step, a pipette is used to move the solvent from the beaker with PMMA/graphene, into one of the empty beakers. In this way the solvent is recovered. Using the second pipette, fresh DI water is moved from the full beaker into the beaker containing PMMA/graphene, until the beaker is full. The process of emptying and filling the beaker is then repeated several times, using the second beaker to deposit the DI water. At least 10 cycles are required to remove any residuals of etchant solution from the sample.
  Attention must be paid not to touch the very fragile graphene with the pipette. Because of the hydrophobicity of the PMMA/graphene [55], it sticks very well to most materials, such as the plastic of which the pipette is made. If the sample becomes attached to it, it will never be possible to recover the graphene.
  The flow of water induced by the pipette should be controlled very carefully too, as bubbles can be formed in the beaker. They tend to be trapped at the interface between graphene and water and it is very difficult to remove them without damaging graphene. If not removed, they will lower the quality and the flatness of the resulting sample once it will be transferred on the substrate.

- As already seen, this former procedure is quite safe for graphene, but is very time consuming. An alternative is to use a plastic spoon to fish delicately the PMMA/graphene square out of the etchant solution and into a clean DI water bath. This transfer must be repeated several times (6 should be enough) in order to allow fresh water baths to disperse etchant solution remaining on the PMMA/graphene.
  In this case it is very easy to destroy graphene or make wrinkles on the sample through contact with the spoon, so it is necessary to be extremely gentle. It could be very useful to use not only a spoon, but also a pipette. The water flow created by the

pipette will drive the PMMA/graphene in its movements in and out the spoon and facilitate the process.

- **Cleaning of the SiO_2/Si^{++} substrate**

At the end of both those cleaning procedures, PMMA/graphene is still floating in a beaker full of clean DI water. The upper surface of the substrate should be cleaned before transferring graphene on it. Here is presented the general procedure followed for cleaning substrates.

First of all, SiO_2/Si^{++} wafers should be cut by a diamond tip in small squares (roughly 8 mm × 8 mm). Squares are then dipped into a beaker containing acetone and then put in a sonicator for 60 seconds. The same procedure is repeated twice, using isopropanol and water mixed with RBS (a clean room soap) instead of acetone. It is better not to use the sonicator at the maximum power in order to avoid the formation of cracks that could lead to the breakdown of the dielectric and reduce the possibility of applying a gate voltage to the substrate for future transport measurements.

Once the squares have been extracted from the sonicator, they should be rinsed by flowing water and dried using a N_2 gas under high pressure. In order to desorb all the water from the surface, the squares are baked on a hot plate at 180 °C for 3 minutes.

Finally the SiO_2/Si^{++} is etched by oxygen plasma, at 1 mbar, for 5 minutes. Plasma etching plays a fundamental role in the success of the graphene "fishing" by the substrate. Indeed the SiO_2/Si^{++} surface is hydrophilic before etching, so that the substrate is covered by a water film and the hydrophobic graphene escapes far from it making deposition very complicated, while plasma etching removes organic layers (like greases, oils or waxes) from the SiO_2/Si^{++} surface making it hydrophobic. In fact, impurities are attacked chemically by oxygen that forms molecules of CO or CO_2. Moreover, plasma heats the sample slightly, which together with the vacuum can force impurities to evaporate. Also, high energy particles in the plasma may cause the breaking of impurities into smaller molecules that can be extracted easily. The UV radiation generated from the plasma can destroy impurities as well.

- **PMMA/graphene deposition on the substrate**

Now the PMMA/graphene can be removed from the solution and transferred onto the desired substrate.

In *Figure 2.11* images taken during the transfer process at NANOsciences are reported. In Figure *2.11 f)* it is shown how the samples look like at the end of the transfer process.

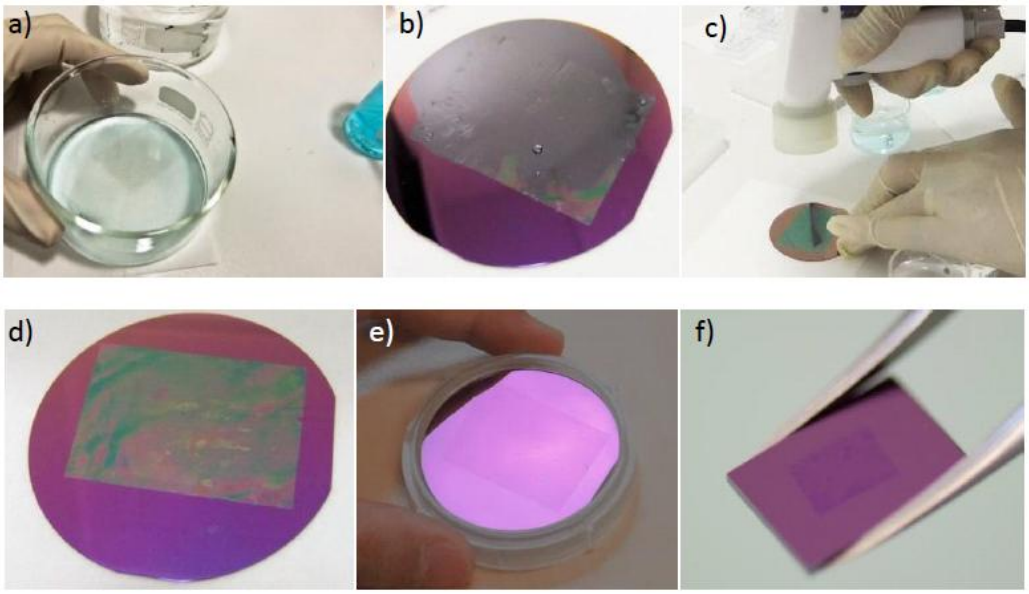

***Figure 2.11**: a) graphene/PMMA bilayer floating on the surface of Na2(SO4)$_2$ solution, b)-d) wet graphene/PMMA bilayer after transfer on SiO_2/Si^{++}, e) transferred graphene on an oxidized silicon wafer after PMMA removal, f) millimetre size graphene. Dimensions of PMMA/graphene layers and SiO_2/Si^{++} presented in a)-e) are bigger than those used in the experiment (roughly 6 cm in diameter for the silicon wafer and 4 cm × 3 cm for PMMA/graphene flakes). The choice to show them is due to a better visibility of graphene.*

The process can be summarized it the following way.

First of all the substrate should be dipped into the water bath and delicately approach the PMMA/graphene square, from the graphene side. As mentioned above, PMMA/graphene is highly hydrophobic, so it would stick easily to the silica substrates. Then, using the substrate as a spoon, graphene should be gently pulled out of water, taking care of avoid folding.

As long as the sample is still wet, it is possible to adjust the position of the

PMMA/graphene on the substrate, putting the PMMA/graphene in the centre by gently pushing it at the sides. It is possible to do that by using a plastic pipette or by tweezers. A pipette is very soft, so it represents a better solution, but attention must be paid not to let the graphene attach onto its surface.

PMMA/graphene/substrate should be left to dry in air for at least a couple of hours in order to achieve a better adhesion at the graphene-substrate interface. Then the PMMA/graphene/substrate is baked for 5 minutes at roughly 100 °C to remove any residual water.

- **PMMA removal**

Once the graphene layer has attached onto the substrate, it is necessary to remove the PMMA over layer.

It is pretty difficult to dissolve PMMA because it sticks very well on graphene. So this is a very important step: the less PMMA residuals, the purer the graphene sample. The procedure for removing PMMA can be summarized in the following way.

The sample should be dipped in a beaker full of acetone and put onto a hot plate at 40 °C for at least 12 hours. Then it may be rinsed with isopropanol. Sometimes this is not enough to remove all the PMMA from the sample, and even with an optical microscope it is possible to see PMMA residuals on graphene[11]. For a better cleaning, the sample could be annealed.

Annealing can be performed in the furnace of the CVD chamber using an argon atmosphere at a pressure of 1 mbar, and a temperature of 300 °C, for at least four hours. It is important not to anneal the sample in air to avoid graphene oxidation, doping and even oxygen induced etching. Annealing also helps to desorb eventual impurities (which bring doping) and to smooth wrinkles and folds present on the graphene surface, due to the growth and transfer processes[12].

If everything went well, at the end of the process, there should be a mm-scale continuous graphene sheet deposited on the silica substrate.

[11] Optical images of graphene samples before and after PMMA removal are presented in the following paragraph, related to the morphological characterization.

[12] See the paragraph about morphological characterization for AFM and optical images.

The transfer technique presented in this chapter has been developed for silica substrate, but it is a very general procedure and can be applied with small changes to almost all the substrates, as will be shown in the following paragraph.

2.2.3.2. CVD-graphene transfer on $SrTiO_3$

The procedure used for graphene transfer on $SrTiO_3$ is very similar to the one used for SiO_2/Si^{++} substrate. In this paragraph we presented only the differences, for the rest we refer to the previous one.

The necessity of developing some changes is due to the fact that it is not safe to anneal $SrTiO_3$ in vacuum or in argon atmosphere as already done for SiO_2/Si^{++}. Indeed, it has been proved that, during the annealing, STO might lose oxygen becoming conductive at the surface [56-57].

The only way to anneal STO preventing its metallization at the surface, is to do that in an oxygen atmosphere, so that the atoms desorbed from the material would be replaced by the O_2 present in the chamber. Unfortunately this would induce oxidation and even etching of the graphene layer [58].

Thus the need of developing a transfer procedure without annealing arises.

There are two possibilities: (i) use the same procedure developed for SiO_2/Si^{++} and simply avoid the annealing step, (ii) develop a new method. Both were tried without noticing relevant differences in the quality and purity of the final graphene layer.

Concerning the new method, it has been developed using a trial-and-error procedure, and it is reported in the following.

Since sometimes annealing seems to be the only way to remove efficiently PMMA residuals from the graphene layer, the idea is to replace PMMA with another polymer, that can be removed avoiding annealing. Instead of directly spin coating PMMA on graphene, two different runs of spin coating were performed. The first one using a different polymer, called S1818[13] , and the second one with PMMA. In that way PMMA is still used as mechanical support for graphene, whereas it is not in direct contact with

[13] S1818 is a polymeric photoresist often used in lithography. From the mechanical and chemical point of view is very similar to PMMA.

it. The spin coating parameters are the same as the ones previously used for PMMA.
As seen in the previous paragraph, copper is then chemically etched and PMMA/S1818/graphene is transferred on the substrate of $SrTiO_3$.
At that point it is necessary to remove the polymeric coverage. At first acetone is used, as presented in the previous paragraph for PMMA only. This procedure should be enough to remove most of the PMMA/S1818 surface. For a better cleaning of the sample it is even possible to expose it to UV light and remove the remaining PMMA/S1818 with a proper lithography developer known as CD-26[14]. After being dipped in the developer, the sample is be rinsed with DI water. It has been proved that no CD-26 residuals are present on the graphene layer. Nevertheless, attention must be paid in using this procedure, because it could damages the graphene surface.

2.3. Sample characterization

In the following paragraphs it will be presented a detail morphological and electrical characterization of our samples, performed using facilities of NANOsciences and of the Surface Science Laboratory (SSL) of ESRF.

2.3.1. Morphological characterization

In order to perform a a morphological characterization of our samples, different techniques have been used, in the following, the main information obtained by each of them will be summarized.

- **Scanning Electron Microscopy**

Scanning electron microscopy (SEM) has been used to characterize the process of graphene growth on copper.

[14] CD26 developer is an alkaline (base) liquid containing tetramethyl ammonium hydroxide (TMAH), it is used in photolithography techniques as a developer for positive resists.

Graphene can grow continuously across Cu grain boundaries and step edges, in the form of islands whose edges can be dendritic or smooth, and whose nucleation and density have been better and better controlled in the few last years.

Details of the grown process are strongly affected by the process parameters. Nowadays there are two main possibilities of growing CVD graphene on Cu: (i) low pressure (typically ~ 1 mbar) and (ii) ambient pressure growth. At ambient pressure the kinetic is higher, that leads to faster deposition of graphene and formation of "hexagonal" graphene islands, rather than "dendritic flowers" as seen in the low pressure case [59].

In case of our experiment, due to the experimental setup requirements, low pressure CVD has been used. In the following images of graphene as obtained in our experiments will be presented.

In *Figure 2.12* it is clearly possible to see the early stage of graphene growth on the copper surface.

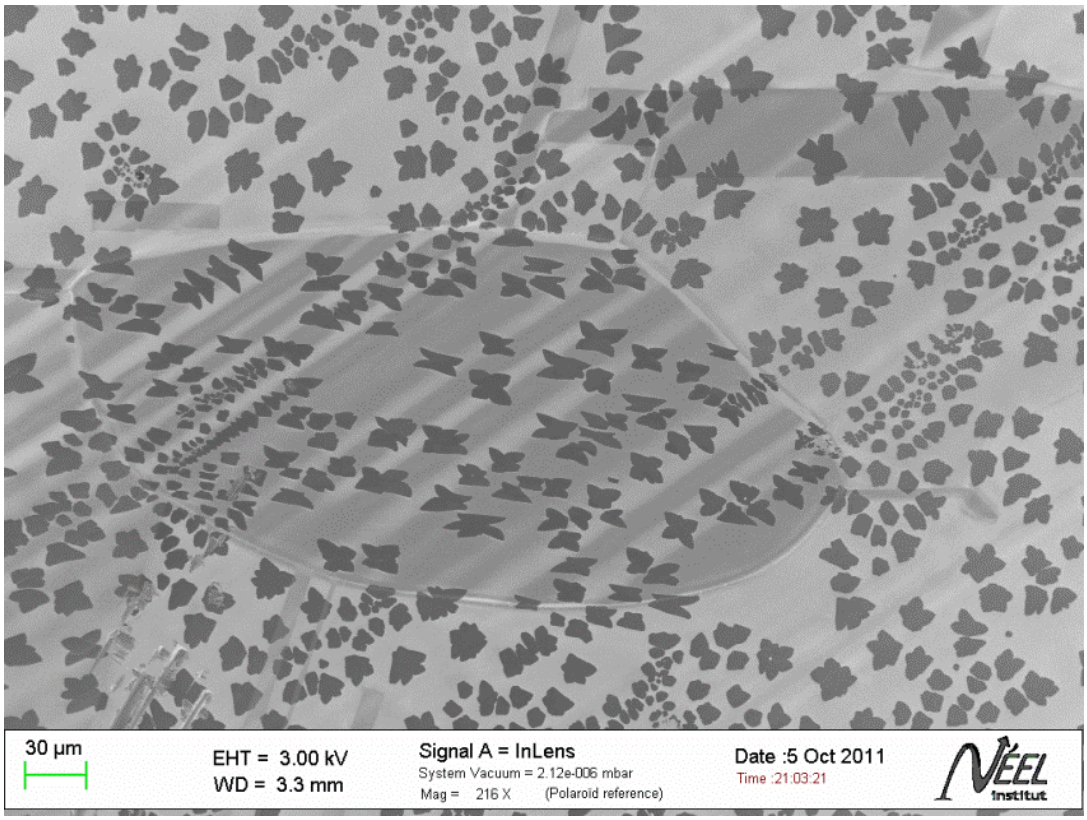

***Figure 2.12**: SEM image of graphene islands growth on copper. Images acquired at NANOsciences.*

The growth process starts, in fact, with the nucleation of small islands in correspondence of substrate defects, then the structures grow with a characteristic "flower like" shape, which can have a more hexagonal, rectangular or butterfly like structure according to the underneath orientation of Cu crystal. After a few tens of minutes growth, the islands start aggregate with each other forming second layer and wrinkles in the regions where they enter in contact.

By controlling the process parameters it is possible to make the graphene islands grow and nucleate until a continuous graphene monolayer is formed on the copper surface.

In *Figure 2.13* it is possible to see how graphene follows very well the underlying copper substrate surface, forming wrinkles in correspondence of edges of copper grains. Even some second layer islands, growing underneath or on top of the first graphene monolayer, are visible[15].

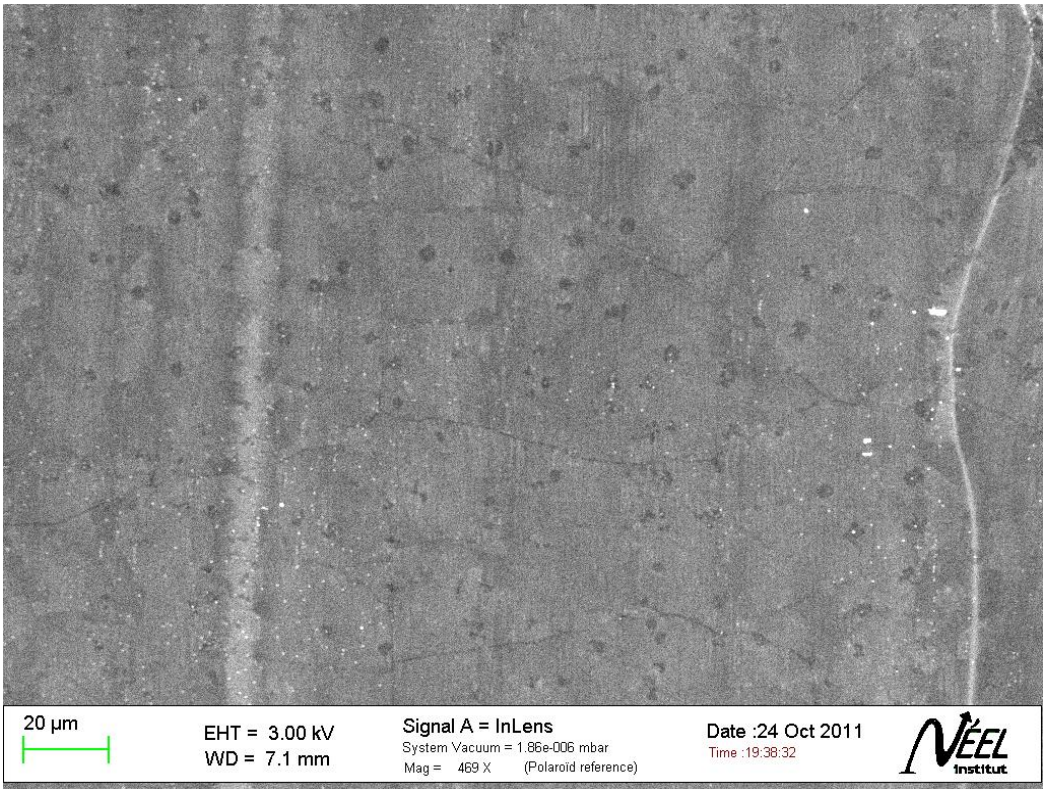

***Figure 2.13**: SEM image of graphene monolayer grown on copper. Wrinkles and second layers are visible. Image produced at NANOsicences.*

[15] For more details, see next paragraph about Optical Microscope characterization.

SEM images have been obtained at NANOsciences with a Field Emission Scanning Electron Microscope ZEISS UltraPlus. To observe with efficiency the thin layer it is used a very low voltage (2 kV and 3 kV), a working distance about 3 mm and the in-lens secondary electrons detector.

- **Optical Microscopy**

Once graphene has been transferred from the copper foil to the desired substrate, optical microscopy is the easiest way for performing a quick identification of single layer and few layers graphene flaks.

As already seen, due to thin film interference effects, graphene becomes visible on SiO_2/Si^{++} substrates using an optical microscope. Indeed, interference between the reflection paths that come from the air-to-SiO_2 and the SiO_2-to-Si^{++} interfaces are affected by thickness variations of a fraction of wavelength, leading to color-shifts that can be easily appreciated by eye. The contrast depends on the thickness of SiO_2, the wavelength of light used and the angle of illumination [60]. Using white light, a 300 nm SiO_2 substrate is required. In the following, some optical images taken on graphene deposited on SiO_2/Si^{++} will be presented. By means of the color scale, it is possible to distinguish some characteristic features, such as single-graphene layers, second layers, grain boundaries, wrinkles, PMMA residuals and eventual impurities.

In *Figure 2.14* is reported a picture of a good quality graphene sample, this is the standard we have tried to keep for the sample used during the experiment. The sample presents a continuous single-layer graphene, with some second-layer islands (less than 5 % of the surface). It is possible to distinguish them because they are darker in the used color scale. Even straight wrinkles are visible, they are due to the process of growth on copper. These wrinkles are associated with the thermal expansion coefficient difference between Cu and graphene, and they are found to cross Cu grain boundaries, indicating that the graphene film is continuous [37]. Sometimes even the transfer process itself can induce wrinkles in the graphene layer, as we will show in the next image. The amount of PMMA residuals (light bluish regions in the upper-left corner of the image), defects and impurities is very low.

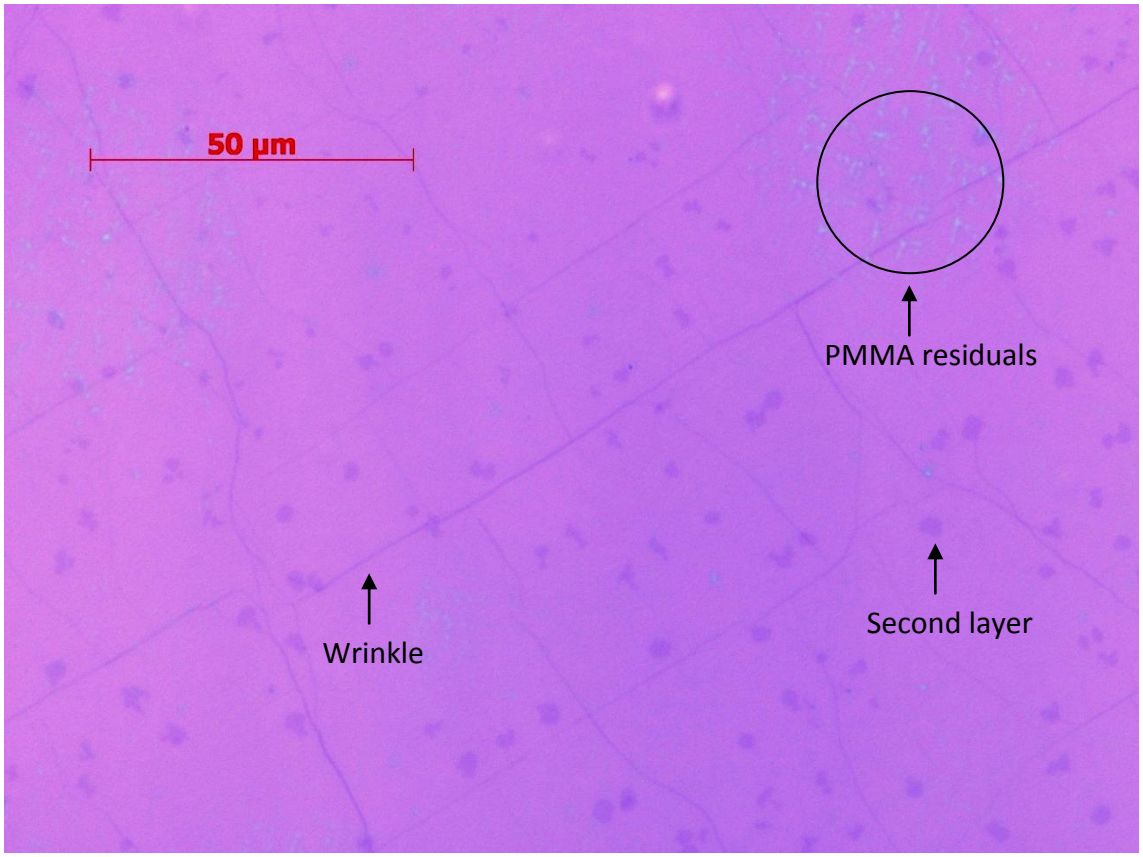

***Figure 2.14**: Optical microscope image of a typical good quality graphene/SiO_2/Si^{++} sample, produced at NANOsciences.*

For a comparison with what we defined as "good quality sample", in the following we also present some images from samples that have been rejected for our experiment. In fact, due to the high variability of the growth and transfer process, not all the samples present the same quality, and a preliminary characterization is always required. Usually, only 3÷4 samples out of a group of six, was considered suitable for our experiment. In *Figure 2.15* a sample with a huge amount of wrinkles and multi-layer in presented. It is still possible to see second-layer graphene islands grown over the underneath monolayer, but in this case the amount is bigger than 5 %, and in some areas it is even possible to see third-layers growing on the top of the second layer[16]. In this case two

[16] The process that lead to the formation of second and multi layers is still under debate. Since few months ago it has been assumed that these islands grow on the top on the graphene monolayer [23], but recent studies suggest that second layers can even grow underneath the graphene monolayer. Indeed during CVD-growth some carbon atoms seems likely to diffuse under the growing graphene monolayer and aggregate creating and underneath second layer in correspondence of copper defects [61].

different kinds of wrinkles can be seen: (i) "small and purple" ones are due to the crystalline grain of copper as seen before, (ii) "big and blue" ones are due to the manipulation of the sample during transfer process.

It is also possible to see some impurities (small blue dots), the origin of whose is still uncertain. They could be: (i) impurities adsorbed on the graphene surface, (ii) copper remains or other defects trapped between the graphene layer and the SiO_2/Si^{++} surface.

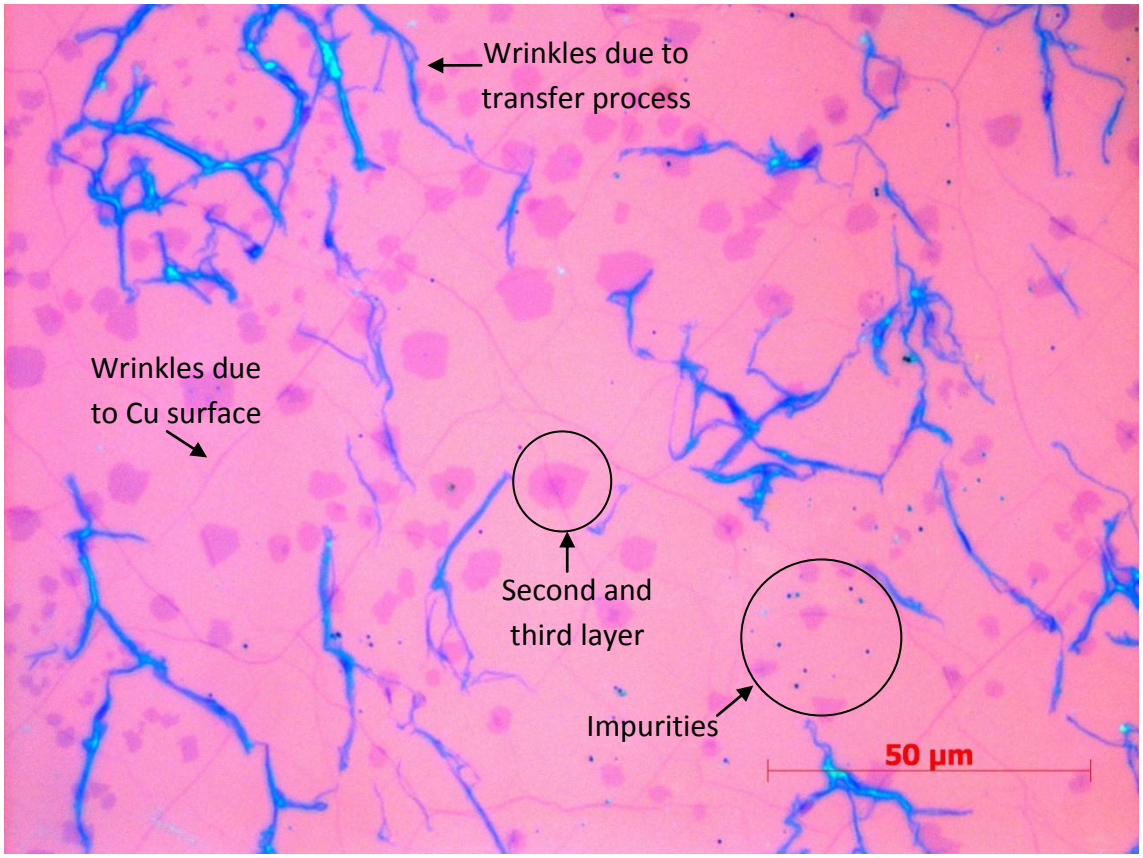

***Figure 2.15**: Optical image of graphene/SiO_2/Si^{++} produced at the NANOsciences department. Multi-layers and wrinkles are visible.*

We have explained how important it is to properly remove PMMA residuals and how, if not completely removed, it is possible to see them even with the optical microscope. In *Figure 2.16* and *Figure 2.17* two examples of how PMMA residuals look like on the graphene surface are shown.

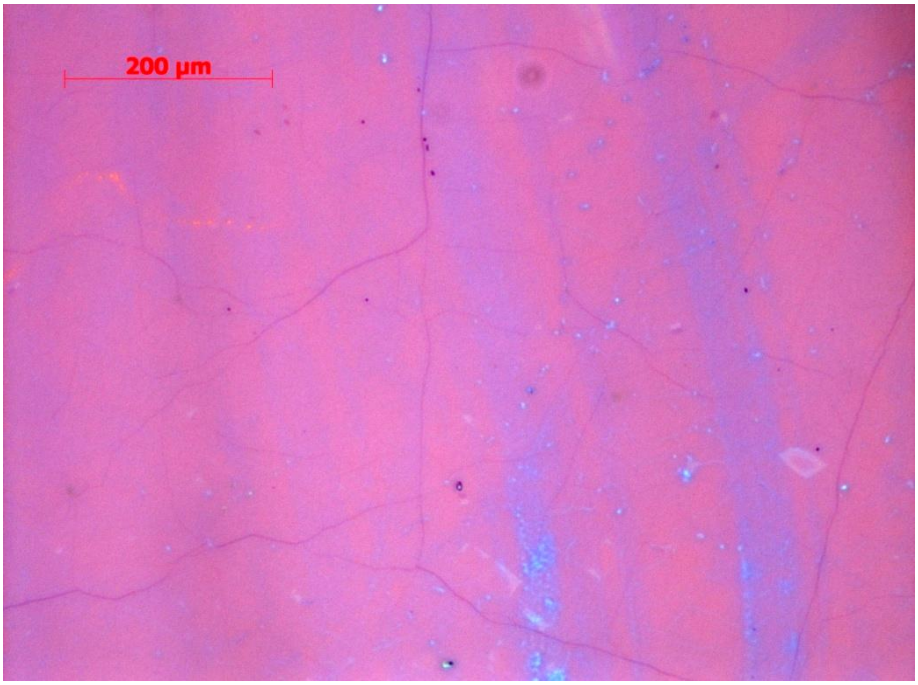

***Figure 2.16**: Optical image of PMMA residuals of graphene/SiO_2/Si^{++}. A sample before PMMA removal is presented, all the graphene surface is covered by a PMMA layer. Image acquired at NANOscences department.*

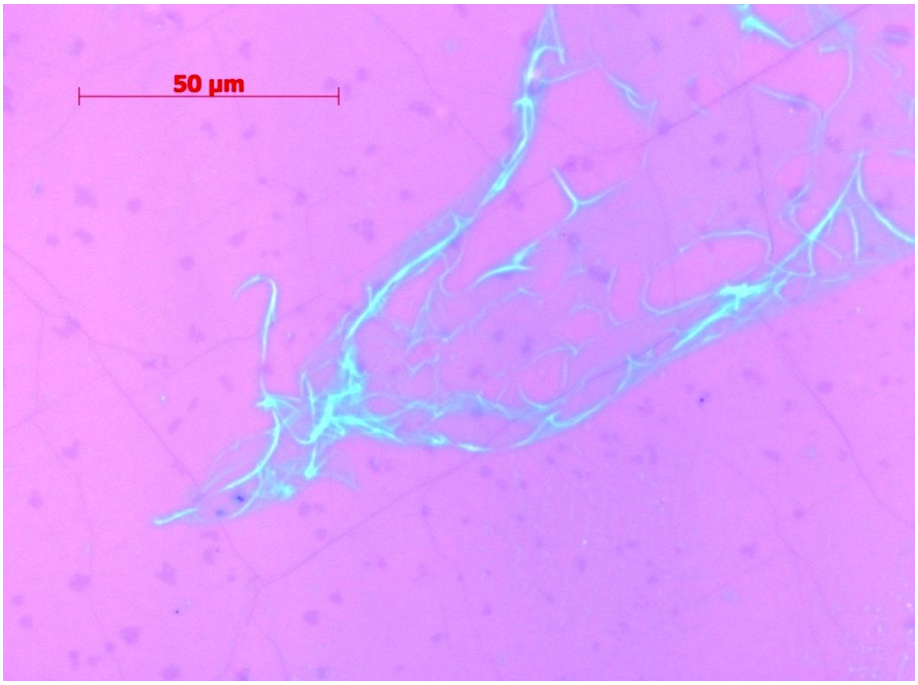

***Figure 2.17**: Optical image of PMMA residuals of graphene/SiO_2/Si^{++}. Residuals of PMMA after acetone rinse are shown. Image acquired at NANOsciences department.*

The same characterization has been performed on graphene deposited on $SrTiO_3$. We do not report images because the contrast is much lower (1,25 %) and it is very difficult to distinguish graphene surface features.

- **Atomic Force Microscopy**

By means of AFM we tried to have a look in more details to the graphene surface and the mean roughness. In the following AFM scans from graphene/SiO_2/Si^{++} will be reported.

In *Figure 2.18* a typical AFM scan of graphene samples used in our experiment is reported. It is possible to see very flat regions (less than 1 nm of variations) intercalated by wrinkles, with an high varying from a few to 10 nm related to the flat surface, as it is shown in *Figure 2.19*, where the roughness profile of the region indicated by the red line in *Figure 2.18* is reported.

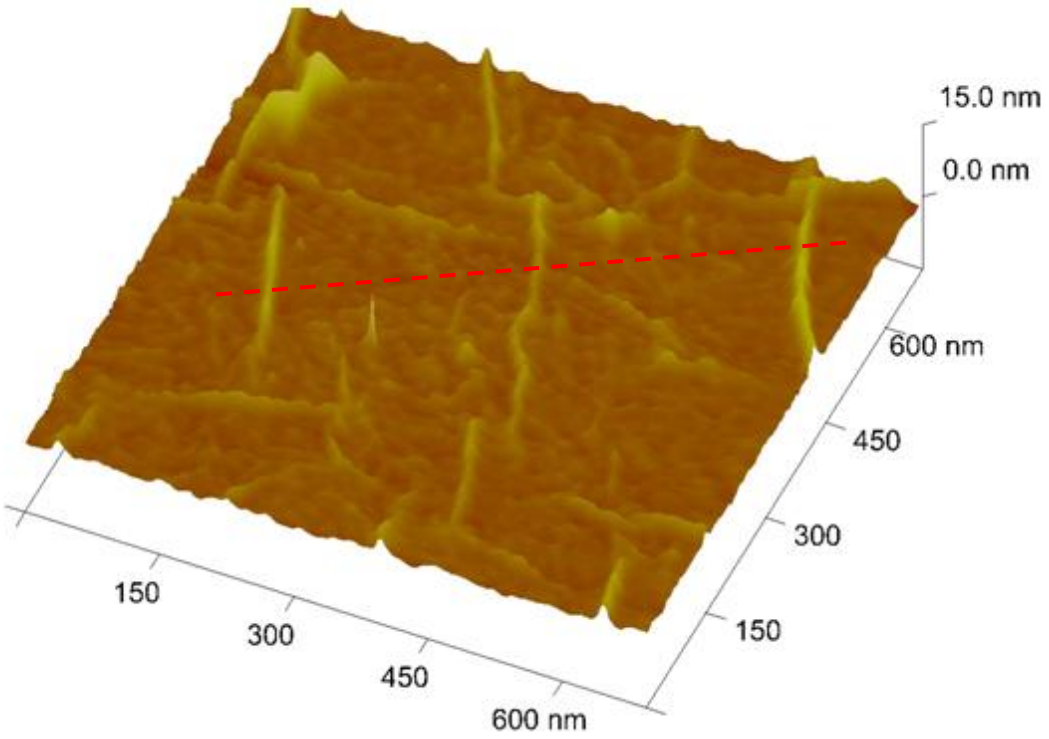

***Figure 2.18**: AFM scan of graphene/SiO_2/Si^{++}. Measurements performed at SSL, ESRF.*

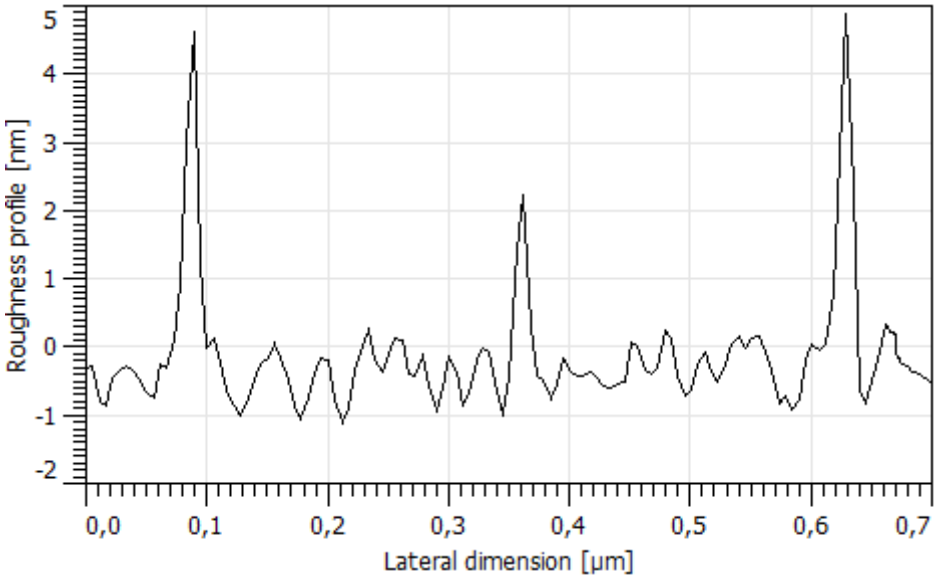

***Figure 2.19**: Roughness profile the region indicated by the red line in Figure 2.18.*

Atomic Force Microscopy measurements have been performed with an Asylum Research AFM at the Surface Science Laboratory (SLS) of ESRF. Both contact and tapping mode have been used.

The same characterization has been performed also on graphene/$SrTiO_3$. No evident differences have been noticed between the two systems. In principle we could expect a lower graphene roughness in case of $SrTiO_3$ substrate compared to SiO_2/Si^{++}, since it has been proved that transferred graphene tends to follow very well the roughness of the substrate underneath [62] and $SrTiO_3$ has smaller roughness than SiO_2 . However, it could be that the noise level in our measurements simply covered the slight differences in roughness.

- **Raman Spectroscopy**

Raman spectroscopy of graphene can be used to determinate the number of graphene layers as well as the density of defects and impurities.

Raman scattering depends on the electronic and vibrational properties of a material. Its spectrum in graphilitic materials has three prominent peaks: G, D, and D'. The G peak (1580 cm^{-1}, 210 meV) arises from in-plane vibration of carbon atoms. The D peak is

associated to defects and it appears in graphene at 1350 cm^{-1} (180 meV). In presence of many defects in the material, D will have a pronounced intensity. The D' peak (2700 cm^{-1}, 365 meV) also known as the 2D peak is sensitive to energy dispersion and it is the indicator for single layer, bilayer and multilayer graphene. Since the interlayer interactions give more phonon modes in Raman scattering, in monolayer graphene the 2D peak is a single and sharp peak, while in graphite it is made by the superposition of multiple peaks, appearing then broader and shifted with respect to the monolayer case [63]. Raman spectroscopy can distinguish a single from a bilayer from few layers graphene (less than five). More than five layers are almost indistinguishable with respect to bulk graphite.

In *Figure 2.20* [64] the dependence of graphene Raman spectra from the number of layers is presented.

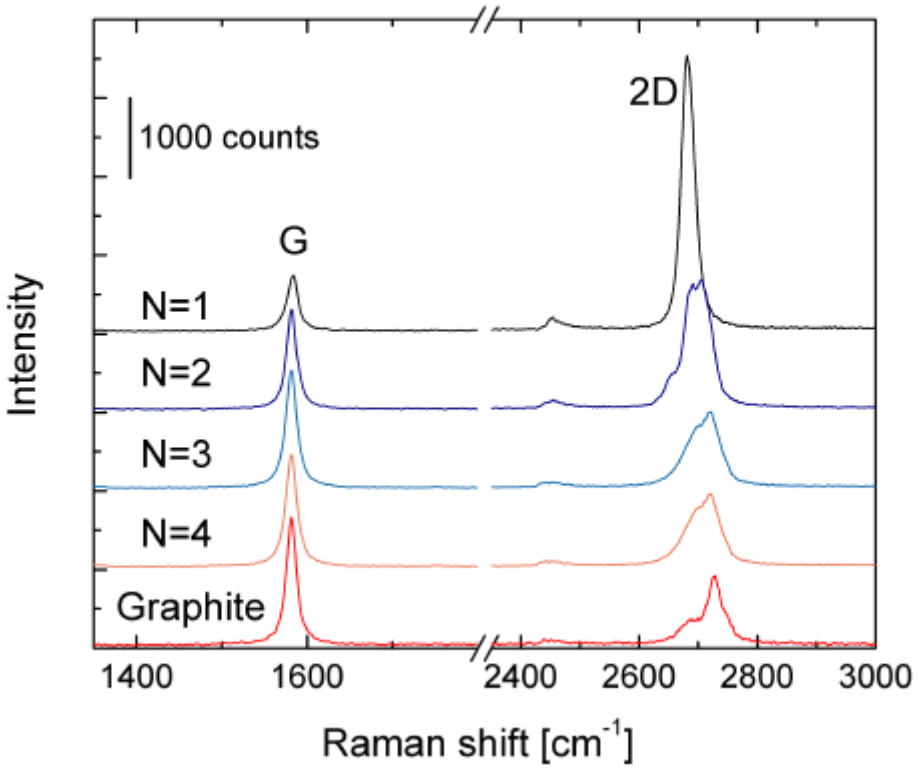

***Figure 2.20**: Raman spectra of N = 1 ÷ 4 layers of graphene and bulk graphite on SiO_2/Si. Single layer graphene shows a very sharp, symmetric, Lorenzian 2D peak, with an intensity greater than twice the G peak. As the number of layers increases, the 2D peak becomes broader, less symmetric and decreases in intensity. Cooper et al., 2011 [64].*

In *Figure 2.21* a Raman spectrum of our samples is presented. From what discussed it is clear that our samples are monolayer graphene flakes. Our spectra have been taken on graphene/copper samples, while the spectra in *Figure 2.20* on graphene/SiO_2/Si^{++}. We are not expecting to see any particular dependence of the Raman spectra from the substrate: if the transfer process has been performed properly, a single layer graphene on copper should retain his single layer features even on SiO_2/Si^{++}. The only difference in Raman spectra could take place at the D peak, which could be more intense on graphene/SiO_2/Si^{++}, since the transfer process can introduce some defects in graphene. When stress is induced during the transfer process, it can also shift the position of G and 2D bands.

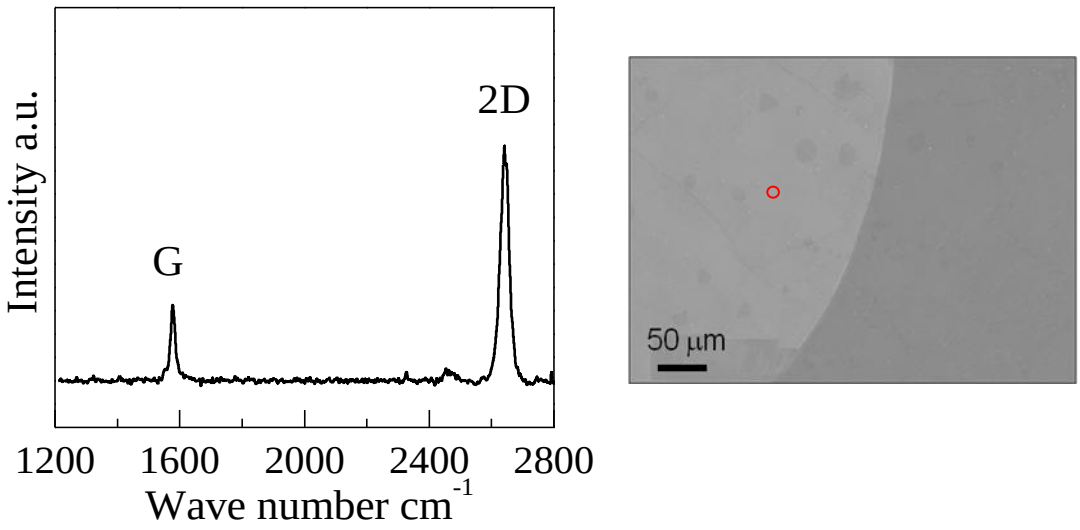

Figure 2.21*: On the left side, Raman spectrum taken from the dotted line in b. Typical monolayer features are distinguishable. Notice the almost invisible D band. On the right side, SEM image taken from one of our samples of graphene on copper.*

Confocal micro-Raman spectroscopy was performed with a commercial Witec Alpha 500 spectrometer set-up with a dual-axis X-Y piezo stage in a backscattering configuration. Laser excitation wavelengths used were 632.8 nm (He-Ne). Raman spectra were recorded in air with a Nikon 100x objective (NA=0.95) leading to a spatial resolution about 320 nm.

2.3.2. Electric transport measurements

Transport measurements have been performed for the graphene samples after deposition on SiO_2/Si^{++} and $SrTiO_3$, in order to characterize their electric proprieties and verify the sample quality.

In *Figure 2.22* a typical field effect curve of millimeter size CVD graphene/SiO_2/Si^{++} is reported. For comparison, the field effect curve for a 1 micron flake of CVD graphene and a 1 micron flake of expholiated graphene are also shown in *Figure 2.23* and *Figure 2.24*.

Pure graphene should be at the Dirac point with an applied back gate of V_g = 0V, that is not strictly true for real graphene, where the Dirac point is often found to be above or below V_g = 0V. CVD-graphene, in particular, it is never neutral, and it is possible to notice both electron or hole doping. Our graphene samples on SiO_2/Si^{++} were always electron doped.

The origin of this intrinsic chemical doping is difficult to determine exactly. One possible scenario associates doping with the impurities introduced during the process of growth and transfer, for example (i) remains of the copper substrate non completely etched away, (ii) residuals of the chemical agents not totally removed by the cleaning with DI water, (iii) impurities adsorbed during the annealing process. However, even the interaction with the substrate itself that can change the density of charges [43].

The process-induced chemical doping is clearly understandable by a comparison of CVD graphene field effect curves with expholiated graphene curves. Expholiated graphene is more similar to ideal graphene, and usually presents less contaminations, indeed its field effect curve usually have a sharp pick in correspondence of the Dirac point at $V_g \simeq$ 0V, while CVD graphene curves are broader and the Dirac point is shifted. So that, compared to exfoliated graphene, graphene prepared by CVD always exhibits lower carrier mobility, which can be ascribed to both its polycrystalline nature and defects induced by the transfer process.

Moreover, in the case of CVD graphene, it is often observed that the amount of doping scales with the graphene area. Indeed, the position of the Dirac point is found to fluctuate, fluctuations are mostly around the value of 20 V for 1 micron flakes of

graphene, while they could reach values as high as 100 V for millimeter size graphene. Since the fluctuations are ascribed to transfer residues locally doping graphene, while preparing 1 micron graphene samples, it is possible to select "good" quality regions, in order to avoid defects and impurities that can increase the sample doping, while using millimeter size graphene this is not possible. Since the field effect measurements are average measurements and not local measurements, the presence of low quality regions in millimeter size CVD graphene can increasingly shift his Dirac point.

This area-related doping not only shift but also broaden the Dirac point. Indeed, due to the presence of different regions with different doping and so different position of the Dirac point in CVD millimeter size graphene, during field effect measurements is sometimes possible to see a sort of "plateau" instead of a sharp Dirac point. This phenomena is due to the convolution of the different field effect curves of the different doping regions present in the sample.

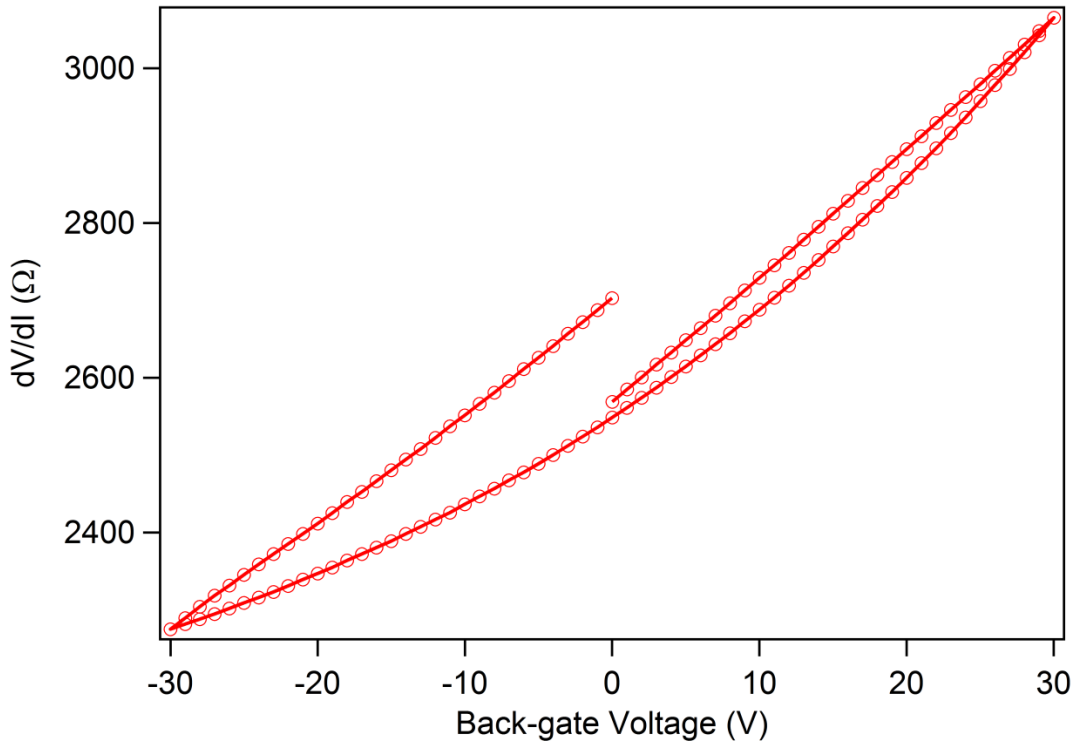

***Figure 2.22**: Field effect curve from millimetric CVD graphene on SiO_2/Si^{++} sample. Measurement performed at NANOsciences at 300K, see Appendix A.*

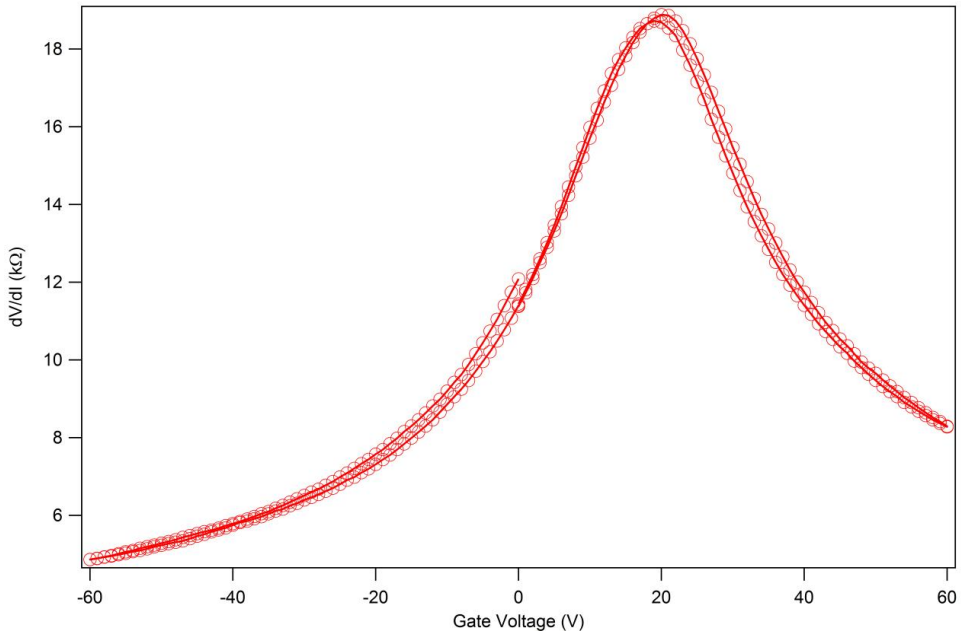

***Figure 2.23**:Field effect curve from 1 micron flake CVD graphene on SiO_2/Si^{++} sample. Measurement performed at NANOsciences at 300K, see Appendix A.*

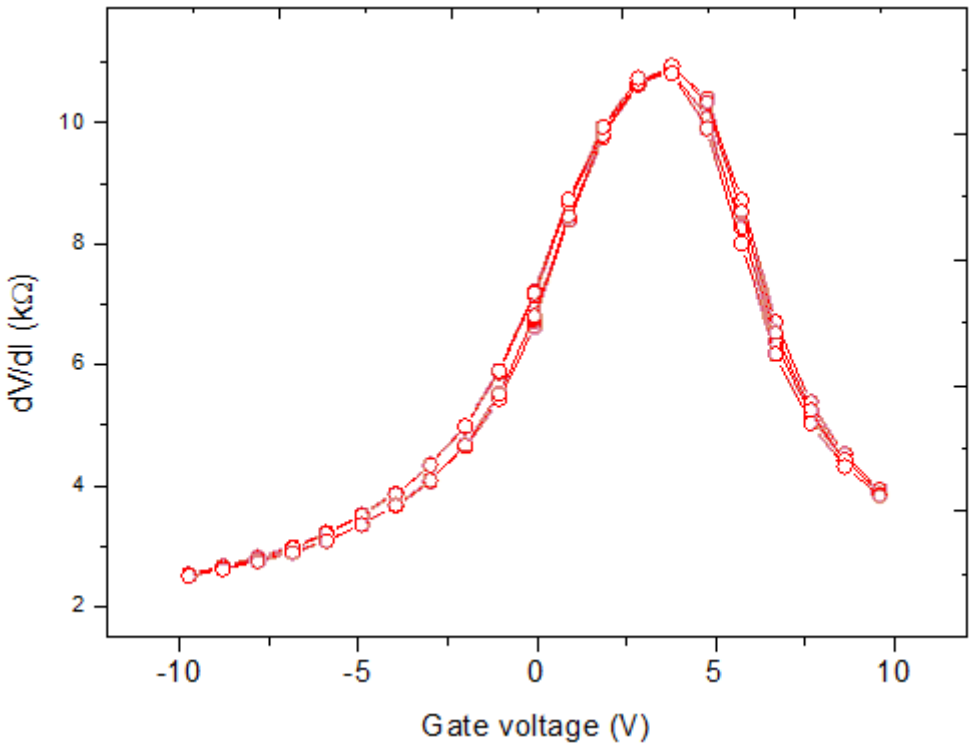

***Figure 2.24**:Field effect curve from 1 micron flake espholiated graphene on SiO_2/Si^{++} sample. Measurement performed at ESRF at 10K, see appendix C.*

In *Figure 2.25* we can see a field effect curve for graphene/STO.

The dependence of STO dielectric constant on the gate voltage (see paragraph 2.2.3) induces a loss of linearity in the relation between charge density and applied gate voltage that can be seen as a "stretching" in the field effect of graphene.

The only way to avoid this problem is to perform the field effect measurement remaining in the range between -15 V and 15 V, where the dielectric constant stays about constant. In particularly, in *Figure 2.25* it is shown a field effect curve obtained remaining in the range ± 10 V for gate voltage.

We also notice that graphene on $SrTiO_3$ shows electron doping at zero gate voltage.

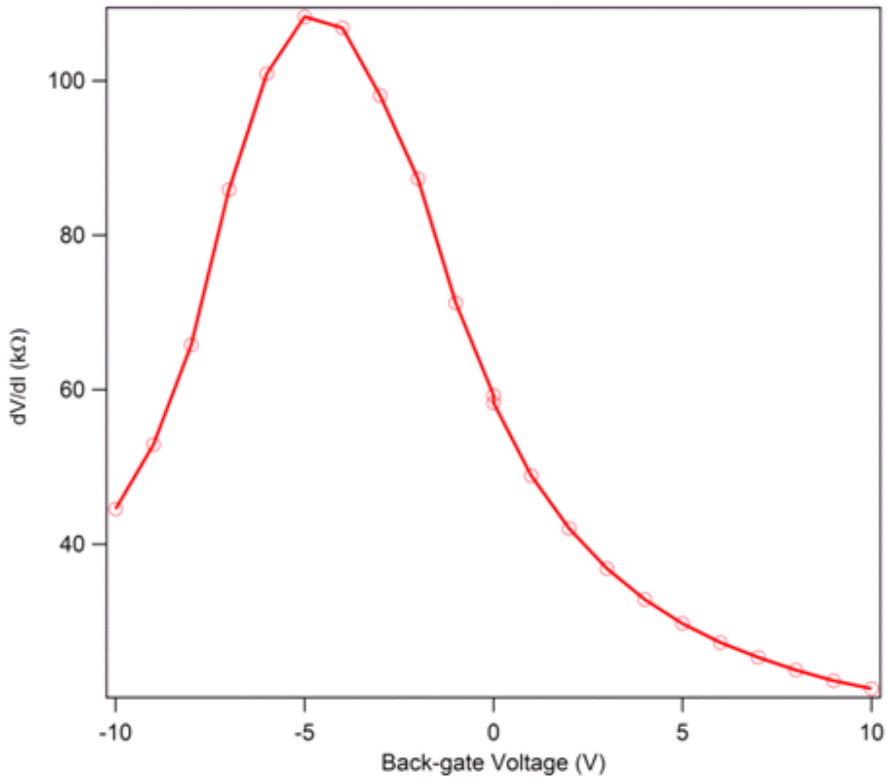

***Figure 2.25**: $SrTiO_3$ field effect curve in "low" voltage regime. Measurement performed at ESRF at 10K, see Appendix C.*

It is then clear the necessity of a proper characterization of the charge doping in our samples, since our goal is to study the possible interaction between electron charges in graphene and the molecules deposited on it.

Therefore all the samples used in the experiment have been previously characterized at the probe station of NANOsciences (for a detail description of the experimental set-up see Appendix A), and then a sample holder provided of electrical contacts have been suitably developed in order to perform a subsequent in-situ characterization during the X-ray measurements, in order to check any possible modifies in the sample doping (for a detailed description of the experimental apparatus see Appendix C).

Chapter 3

Magnetism and charge transfer in CoPc molecules on graphene substrates

Once obtained graphene samples as described in the previous chapter, CoPc molecules have been deposited on them and X-ray spectroscopy measurements have been performed at the ID08 beamline of European Synchrotron Radiation Facility (ESRF). The aim was to study the magnetic and electronic proprieties and the hybridization with the substrate of the Co central ion in CoPc/graphene systems.

In this chapter X-ray absorption techniques and experimental setup will be introduced, then the experimental results will be presented and discussed in the framework of existing models. In the first paragraph a brief theoretical and experimental introduction to the X-ray spectroscopy techniques used here will be discussed. In the second paragraph the experimental apparatus will be described, with a focus on the sample preparation. Finally, in the last paragraph experimental XAS, XMCD and XLD results for CoPc molecules on different graphene substrates will be presented. Co spectroscopic features for CoPc on HOPG, SiO_2 and $SrTiO_3$ substrates will be analyzed and compared to both calculations and experimental results for similar CoPc systems. Individuation of the molecule electronic structure and d orbitals filling will allow to investigate the charge transfer in these systems, which is found to strongly depend on the carrier type and concentration at the graphene Fermi level.

3.1. X-ray absorption spectroscopy techniques

In the following paragraphs the X-ray absorption spectroscopy techniques used to characterize the electronic and magnetic properties of CoPc molecules will be presented. Some peculiar proprieties of these techniques make them particularly suitable for our experiment.

First of all x-ray absorption is element specific, allowing to obtain information on a specific chemical element in a composite system. In the case of the present experiment, chemical sensitivity is used to directly address the electronic configuration of the central TM ion in metal-Pc molecules which is not achievable with other techniques (for example spin polarized STM and STS, for more detail see paragraph 1.2.2).

Second, the high intensity of synchrotron radiation allows studying extremely diluted systems, where the content of the element under investigation is about only few percent of a monolayer (ML). This possibility is very important for our experiment, as we want to keep the molecules as much far away from each other as possible, to avoid eventual interactions. Surface sensitivity is insured by recording the signal with the TEY mode (see paragraph 3.1.4).

Third, the use of synchrotron radiation with variable energy and circular polarization allows to achieve quantitative information on the spin and orbital moment of the selected element which is not the case with other magnetization sensitive techniques like SQUID[17].

It is also important to stress the fact that X-ray techniques are non-local, spatially integrated techniques, where the detected signal is the average over an area of the sample determined by the dimension of the beam spot size. In that way it is possible to have an idea of the average behaviour of the molecules on the substrate, differently from what is done with local techniques such as STM or AFM.

[17] SQUID is an acronym for Superconducting Quantum Interference Device, which is a very sensitive magnetometer made by superconducting loops containing Josephson junctions and used to measure stable magnetic fields.

3.1.1. XAS spectroscopy

X-ray Absorption Spectroscopy (XAS, also known as Near Edge X-ray Absorption Fine Structure (NEXAFS), allows to probe the unoccupied electronic states of a sample. As already seen, it is an element specific technique since the absorption edges have different energies for each atom, and it is even a chemically specific technique because it is able to distinguish chemically different environments for the same atom.
The absorption signal is analyzed at different photon energies, so that a tuneable source is necessary. In order to get a tuneable x-rays source with high intensity and brilliance in a wide range of energies, a synchrotron radiation facility is required (for more details about synchrotron radiation production and characteristics we refer to Appendix B).

3.1.1.1. The single electron picture: selection rules

In XAS the photon energy is scanned across an absorption edge. In a first order approximation, we can assume that if the incident photon energy is sufficient (i.e. comparable with the electron binding energies of the material under study), a core electron can be promoted into an unoccupied higher energy state of the sample creating a core hole. The system is now in an unstable state and equilibrium is reached again upon filling the core hole. This can occur either (i) radiatively by means of a fluorescence process, or (ii) non-radiatively by means of Auger decay. The former is a process in which an electron in a high energy position fills the core hole state and a photon is emitted with an energy corresponding to the difference between the energy of the electron in the initial and in the final state. In the Auger process instead the energy released by the decay of the high energy electron is resonantly transferred to an electron at higher energy, which is photoemitted in that way. The time constant associated to both the filling processes is in the order of femto- or attoseconds, and it depends on the location of the core hole.
In *Figure 3.1* a very schematic view of the absorption process is presented.
In the case of molecules, such as CoPc, we can consider transitions between core states,

and molecular states located near the HOMO (highest occupied molecular orbital) and LUMO (lowest unoccupied molecular orbital), while in the case of bulk materials we consider transitions between core states, which are so strongly bound to the nuclei to be treated as atomic-like states, and a continuum of levels given by the valence and conduction bands.

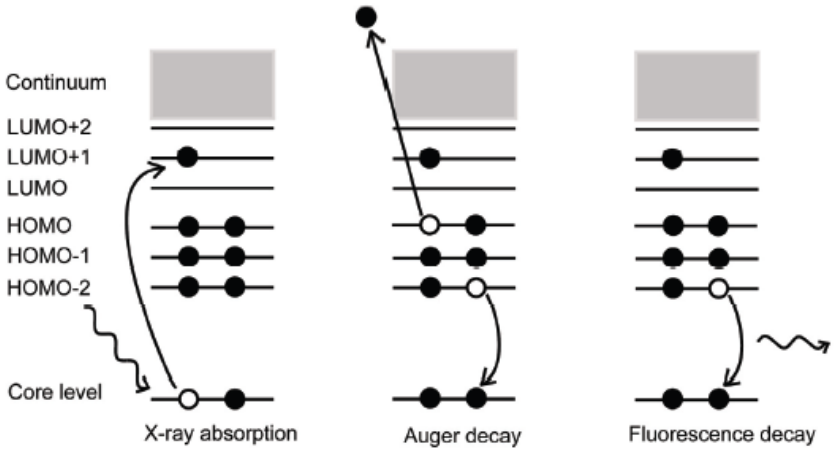

***Figure 3.1**: Schematic view of the X-ray absorption process and excited-state decay.*

In order to understand the absorption process more in detail it is necessary to focus on the interaction between incident photons and matter. As already seen, since the light induces transitions from the core levels to higher energy levels, it is possible to define the absorption cross section of the process σ as the number of excited electrons per unit time $W_{i\to f}$ (or transition amplitude between the initial and the final state) divided by the incident photon flux F_0:

$$\sigma = \frac{W_{i\to f}}{F_0} \tag{3.1}$$

$W_{i\to f}$ is given , in a first order perturbation theory, by the Fermi Golden Rule:

$$W_{i\to f} = \frac{2\pi}{\hbar}\sum_f \left|\langle \phi_f \left|\widehat{H_1}\right| \phi_i\rangle\right|^2 \delta\left(E_f - E_i - \hbar w\right) \tag{3.2}$$

in which E_f and E_i are the energies of the final and initial electronic state, with the summation carried over all the possible experimentally-indistinguishable symmetry-degenerate final states, $\hbar w$ is the incident photon energy, ϕ_f and ϕ_i are the initial and final state wavefunctions, $\widehat{H_1}$ is the perturbation Hamiltonian. In a first order model, considering only one photon process, $\widehat{H_1}$ can be written as:

$$\widehat{H_1} = -\frac{e}{mc}\boldsymbol{A}\cdot\boldsymbol{p} \tag{3.3}$$

with $\boldsymbol{A}$ vector potential of the electromagnetic radiation and $\boldsymbol{p}$ electronic momentum operator of the system. The expression has been simplified choosing the Coulomb Gauge for $\boldsymbol{A}$, so that $\boldsymbol{\nabla}\cdot\boldsymbol{A} = 0$ and the commutator [$\boldsymbol{A}$, $\boldsymbol{p}$] between the two operators is zero, where **p** can be written as -i $\hbar$ $\boldsymbol{\nabla}$.

In order to easily calculate the absorption cross section it is possible to introduce two important approximations to simplify the relation in (3.2): (i) the *electron dipole approximation* and (ii) the *single-electron approximation.* The electron dipole approximation considers that during the absorption process the core-electrons, localized around the nuclei, do not see spatial variation of the electromagnetic wave, since it can be assumed that the photon wavelength is larger compared to the electronic shells typical dimensions. $\boldsymbol{A}$ can then be considered as a constant in the integral involving the $\boldsymbol{A}\cdot\boldsymbol{p}$ operator. This approximation is valid in the energy range of soft x-rays (photon energy lower than 2KeV), in which our measurements will be performed. The single-electron approximation instead concerns the electron excitation process which is considered to be a one-electron process. This allows to write the initial state as a core wavefunction and the final state as an empty level wavefunction. All the other electrons are assumed not to take part in the X-ray transition process. Using (i) and (ii) the absorption cross section can now be expressed as:

$$\sigma \sim \left|< \phi_f \left|\boldsymbol{\epsilon}\cdot\boldsymbol{r}\right|\phi_i >\right|^2 \rho\left(E_f - E_i + \hbar\omega\right) \tag{3.4}$$

where $\boldsymbol{\epsilon}$ is the photon helicility that depends on the polarization of the incident beam and is conventionally labelled as $\boldsymbol{\epsilon^0}$ for linear and $\boldsymbol{\epsilon^{\pm}}$ for right (R) and left (L) circular

polarization respectively and **r** is the position vector of the electron considered in the interaction. The sum over all the possible final states has been replaced by $\rho(E)$, which is the density of the unoccupied final states, and $\rho(Ef - Ei + \hbar\omega)$ simply express the energy conservation, as well as the delta function in (3.2).

The only allowed transitions are the ones for which σ is different from zero. The requirement for the matrix element $\langle\phi_f|\boldsymbol{\epsilon}\cdot\boldsymbol{r}|\phi_i\rangle$ not to be zero imposes the following conditions for the quantum numbers of the final state, also known as dipole selection rules: $\Delta l = 0$ (parity), $\Delta m_l^{linear} = 0$ and $\Delta m_l^{R,L} = \pm 1$ (angular momentum conservation), $\Delta m_s = 0$ and $\Delta s = 0$ since the operator $\boldsymbol{\epsilon}\cdot\boldsymbol{r}$ does not involve the electron spin, thus it is conserved during absorption processes. If levels are split due to spin-orbit interaction, m_l and m_s are no more good quantum numbers, hence they are not separately conserved during transitions, and the selection rules becomes: $\Delta j = 0, \pm 1$ (parity), $\Delta m_j^{linear} = 0$ and $\Delta m_j^{R,L} = \pm 1$ (total angular momentum conservation).

In the previous expressions *j*, *l*, and *s* are the quantum numbers of the total angular momentum, the orbital angular momentum and the spin momentum respectively, while m_j, m_l and m_s are the components of the total, orbital and spin moments along the quantization direction, given by the propagation direction of the beam, assumed to point in the *z* direction. The superscript label of m_j and m_l indicates the light polarization, which could be either linear or circular (positive or negative).

The initial and final states of the system, ϕ_i and ϕ_f, are then properly expressed as linear combinations of ϕ_{n,l,m_l,m_s} states using Clebsch-Gordan coefficients and the matrix elements in (3.4) are evaluated. The use of this notation is because the absorption process directly involves the angular momentum quantum numbers *l* and m_l and not the total moment *j*. For a complete derivation see reference [65].

The relations obtained so far have a general value and, in a first order approximation, allow to obtain good agreement with the experimental spectra for different classes of materials [66].

In the following we will be interested in studying compounds including *3d* TM as well as nitrogen ligands, the interested transitions allowed by dipole selection rules will be then:

$$L_2 : 2p_{1/2} \rightarrow 3d_{3/2}, 4s \qquad (3.5)$$
$$L_3 : 2p_{3/2} \rightarrow 3d_{3/2,5/2}, 4s$$
$$K : 1s \rightarrow 2p_{1/2}$$

where the subscript indicates the total angular momentum quantum number *j*.

It has been proved that for 3d TM the "white lines" transitions from *p* to *d* states, dramatically dominates the process, since they correspond to almost 95% of the total absorption [67]. Therefore, transitions from *p* to *s* levels will not be considered in the future. Moreover, the electronic and magnetic proprieties of *3d* TM compounds are strongly related to the unfilled *3d* states. Thus, our attention will be dedicated to the $L_{2,3}$ absorption edges, which are located in the energy range of the soft x-rays.

Further, we will make use of the nitrogen *K* edge that is also located in the soft X-rays energy range. In this case only the linear dichroism will be investigated, which will be explained in paragraph 3.1.3.

In *Figure 3.2* an example of XAS spectra is reported.

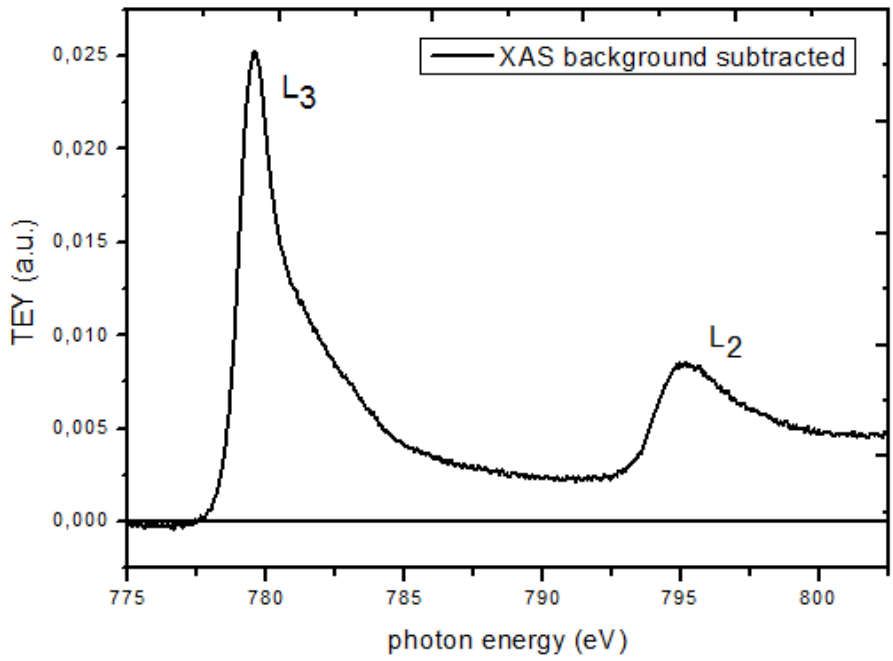

***Figure 3.2**: XAS spectra of Co nanostructures deposited on graphene/SiO_2/Si^{++}. Measurements performed at ID08 beamline (ESRF) at 10. $L_{2,3}$ absorption edges are indicated in figure.*

Figure 3.2 presents XAS spectra of Co nanostrucutres (about 10% of a monolayer as estimated from comparison with known Co coverage samples on the same substrate[18]) deposited on graphene/SiO_2/Si^{++}.

The L_2 and L_3 absorption edges are indicated in the image. The graphene substrate background XAS, measured before Co deposition, has been subtracted from the spectra.

As explained with (3.4), the sum of the intensities of L_3 and L_2 lines after the eventual subtraction of the *2p→4s* contribution is proportional to the number of unoccupied states in the *3d* Co band.

3.1.1.2. Beyond the single electron approximation: multiplet splitting

Before moving to a description of XMCD and XLD signals, that will be presented in the next paragraph, it seems necessary to explain what happens to the model summarized by equation (3.4) if removing the single-electron approximation.

Indeed, the model presented so far is a very simplified scheme of the process, which neglects the interaction between electrons. In most of the experimental cases this model is accurate enough (especially for bulk materials), however it represents a very strong approximation in case of single atoms and single molecules. In relation to the needs of this experiment, it is then interesting to see what happens when relaxing this approximation.

In the following a summary of the theoretical interpretation of *3d* TM compounds spectra, as proposed in 1990 by de Groot *et al.* [68], will be presented.

The starting point is again the x-ray-absorption cross section, removing the approximated assumption considered in obtaining (3.4), it can be generally written as:

$$\sigma(E_X) \sim \sum_f \left|\langle \phi_i | X | \phi_f \rangle\right|^2 \delta(E_f - E_X - E_i) \qquad (3.6)$$

where *X* represent a generic perturbation acting on the system (i.e. the absorption of the

[18] From the height of the L_3 edge jump compared to the background intensity it is possible to estimate the amount of material deposited, once calibrated with an additional technique such as STM.

phonon) and E_X is the associated energy, while ϕ_i and ϕ_f are the wavefunctions of the initial and final states, as already seen for (3.4).

Differently from (3.4), de Groot *et al.* introduced the idea that the single particle approach, where ϕ_i is a core state and ϕ_f is an empty state, simply coupled by dipole selection rules, is not enough in order to properly calculate the cross section given by (3.6). Indeed, for *3d* TM compounds, it is necessary to consider the *3d-3d* and the *2p-3d* two-particle interactions in determining the *2p* XAS spectrum, since these interactions are responsible of the TM ion ground state and split the possible final state in to a large number of configurations.

Considering at first an atomic approach, so that any solid state effect will be negligible and atomic multiplets features will be expressed explicitly, it is then possible to express the *2p* XAS cross section of *3d* TM ions as:

$$\sigma_{2p}(E_X) \sim \sum_j \left|\left\langle \phi_G(3d^N)_{O(3)} \middle| X \middle| \phi_{fj}(2p^5 3d^{N+1})_{O(3)} \right\rangle\right|^2 \delta(E_f - E_X - E_G) \qquad (3.7)$$

where $\phi_G(3d^N)_{O(3)}$ is the ground state of the $3d^N$ multiplet, while $\phi_{fj}(2p^5 3d^{N+1})_{O(3)}$ is the final state *j*, considering all the possible *j* final states for the atomic multiplet. The label *O(3)* indicates that we are using a spherical geometry for the system, since we are considering an atomic model. We will discuss later how the Hamiltonian of the system can be changed in order to consider a different geometry, for example it is possible to modify this atomic description to include the solid state interactions just by adding a cubic crystal field term to the Hamiltonian of the system.

The atomic multiplet spectrum can be calculated considering dipole transitions from the ground state multiplet to all the possible final multiplet states.

In order to calculate $\phi_G(3d^N)_{O(3)}$ and $\phi_{fj}(2p^5 3d^{N+1})_{O(3)}$ states, it is necessary to know the Hamiltonian of the system in the two configurations.

De Groot *et al.* proved that the Hamiltonian in the $3d^N$ initial-state multiplet can be expressed as the *3d-3d* Coulomb interaction (H_{dd}), while the *3d*-spin-orbit coupling is shown to be small and will be neglected since hybridization and temperature effects will mix the spin-orbit split states.

As what concerns the $2p^5 3d^{N+1}$ final state, it is necessary to add two terms to the ground state Hamiltonian, which are related to the presence of the *2p* core hole: (i) the first term considers the spin-orbit coupling of the *2p* core hole (H_{cLS}) and splits the *2p* adsorption edge into L_3 and L_2 edges, respectively related to transitions from $2p_{3/2}$ and $2p_{1/2}$ states, (ii) the second term is due to the *2p-3d* Coulomb and exchange interaction (H_{cd}).
In conclusion the total ground state Hamiltonian and the excited state total Hamiltonian for the atomic multiplet can then be written as:

$$H_{A\phi_G} = H_{dd} \tag{3.8}$$

$$H_{A\phi_{fj}} = H_{dd} + H_{cLS} + H_{cd} \tag{3.9}$$

In order to extend the description from the atomic to the solid state configuration, it is possible to simply simulate the solid (or, as in the case of our experiment a more general surrounding environment for the central TM ion, such as the isonodol structures of the Co-Pc) with the addition of a crystal field term (H_{CF}) to the total Hamiltonian (3.9):

$$H_{A\phi_{fj}} = H_{dd} + H_{cLS} + H_{cd} + H_{CF} \tag{3.10}$$

In the case of a solid it is possible to consider a cubic crystal field, which reduces the symmetry of the system from *O(3)* to O_h, while for Co-Pc molecules a D_{4h} symmetry will be introduced, as already seen in the first chapter.
Depending on its symmetry and intensity, the crystal field can further split the initial and final multiplet states inducing changes in the spectrum.
It is then possible to introduce in (3.10) a correction related to lower symmetries (H_{LCF}), *3d* spin orbit coupling (H_{LS}), magnetic interactions (H_{ex}) and intra- or extra-atomic interactions. However, in general they can be neglected since their influence in the final state multiplet is very small.
Knowing the Hamiltonian of the system, is then possible to calculate the multiplet of the $3d^N$ initial state and the $2p^5 3d^{N-1}$ final state, and to determine the $\phi_G(3d^N)_{O(3)}$ ground state. Considering dipole interactions from the initial to the final state, the XAS cross

section in (3.6) is finally obtained as a series of lines at energies (E_G - E_{fj}) with an intensity given by the correspond matrix element of the transition from the initial to the final state: $\left|\langle\phi_G(3d^N)_{O(3)}|X|\phi_{fj}(2p^5 3d^{N+1})_{O(3)}\rangle\right|^2$. Real experimental spectra are broaden in comparison with the series of lines obtained theoretically, this broadening effect is due to different causes, such as: (i) lifetime effects, (ii) vibrations, (iii) hybridization. However, spectra obtained with this model, based on atomic multiplet calculations and crystal field, are found to be in a good agreement with experimental data from *2p* XAS for *3d* TM compounds.

In *Figure 3.3* [69] XAS spectra from Co clusters with different size are presented.

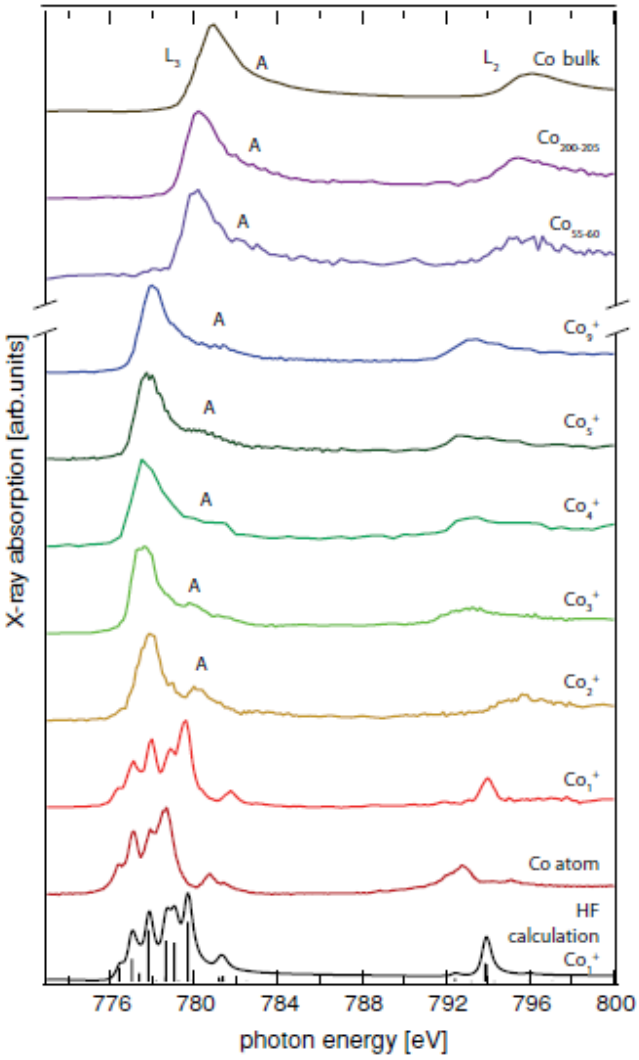

***Figure 3.3**: XAS spectra from Co clusters of different size. Extracted from [69]. Multiplet splitting transition and experimental broadening are shown.*

Typical multiplet splitting features are visible for monomers Co_1, which disappear abruptly already for dimers Co_2. Increasing Co-Co coordination leads to the screening of the core hole–electron interaction with sudden reduction of the multiplet splitting and broadening of the spectrum. Multiplet splitting features completely disappear with the formation of complexes with highly coordinated TM atoms and of a metallic *d* band. The spectra continue to evolve with increasing Co-Co coordination and already above 10 atoms similar spectra to those found for bulk Co are observed. Changes in the crystal field at the cobalt atoms and *d* electrons delocalization, are responsible for the shift of the energy spectra while increasing the cluster dimension.

The de Groot *et al.* model is then valid for *3d* TM single atoms structures, or *3d* TM compounds where the metal ions do not interact directly as in the case of CoPc molecules.

In the following paragraphs the effects of light polarization on the spectral shape will be evaluated, through X-ray linear and circular dichroism.

3.1.2. XMCD spectroscopy

X-ray Magnetic Circular Dichroism (XMCD), is an x-ray absorption technique in which circular polarized light is used to probe the magnetic state of the system under investigation. X-Ray Magnetic Dichroism (XMD) was demonstrated for the first time by using linear polarized light in 1986. Since then XMCD has been further developed both theoretically and experimentally, becoming an important techniques in studying magnetic proprieties of materials especially at the nano-scale.

XMCD has the advantage to bring information on the element specific spin and orbital magnetic moments and also on their anisotropies, when studied at different angles between magnetization and sample normal.

The main idea of XMCD is the fact that the absorption process for a magnetized sample depends on the relative orientation of the sample magnetization **M** and the photon helicity $\boldsymbol{\epsilon}$, which indicates the light polarization direction. Indeed, as already seen, light can have linear or right (R) and left (L) circular polarization and the corresponding helicity is conventionally labelled as $\boldsymbol{\epsilon^0}$ for linear and $\boldsymbol{\epsilon^{\pm}}$ for R and L circular

polarization, respectively.

XMCD is defined as the difference in the absorption cross sections for parallel $I+$ and antiparallel $I-$ alignment between the sample magnetization **M** and the helicity of circular polarized light. This can be measured equivalently by using R and L circular polarization or by changing the magnetization direction. In *3d* TM systems the XMCD signal is found to be proportional to the imbalance between majority and minority *3d* states above the Fermi level, which defines the sample magnetization **M**. In the following, a qualitative explanation of the physics underlying XMCD will be presented. The model presented is taken from to Stohr *et al.* [70].

Starting from the calculation presented in [65] it can be proved that the probability P to excite a selected spin state with a certain light polarization (R or L) (defined as the squared matrix element normalized by the sum of all the squared matrix elements for the considered edge) for both edges is given by: $P_{R,up}(L_3) = 62.5\%$, $P_{L,up}(L_3) = 37.5\%$, $P_{R,up}(L_2) = 25\%$, $P_{L,up}(L_2) = 75\%$. This means that R circularly polarized light excites more spin up at the L_3 edge than at the L_2 edge, and the opposite is true for L circular polarized light, where: $P_{R,down}(L_3) = 37.5\%$, $P_{L,down}(L_3) = 62.5\%$, $P_{R,down}(L_2) = 75\%$, $P_{L,down}(L_2) = 25\%$. In *Figure 3.4* a scheme of allowed transitions and relative intensities between the initial states given by the $2p_{3/2}$ and $2p_{1/2}$ core states and the final *3d* states, split into minority and majority spin states is presented. It is clear that P depends on the light polarization and on the value of m_l in the initial state.

It is now necessary to introduce the presence of *3d* unfilled states, to understand how a net magnetization can change the allowed transitions of the excited photoelectrons and how this is reflected in the XMCD signal. The proportionality of the absorption cross section to the density of the final empty states is expressed in (3.4). In the absence of a net magnetization, the number of excited electrons for a given light polarization will be the same for any of the two edges L_2 and L_3, since the total spin polarization of both $2p_{3/2}$ and $2p_{1/2}$ states is equal to zero. Consider now the effect of a net magnetization, suppose that the *3d* states, in the case of single atoms or molecular systems, or the *3d* bands in the case of solids, are exchanged split and the empty states have a predominantly minority character, as explained in *Figure 3.5*.

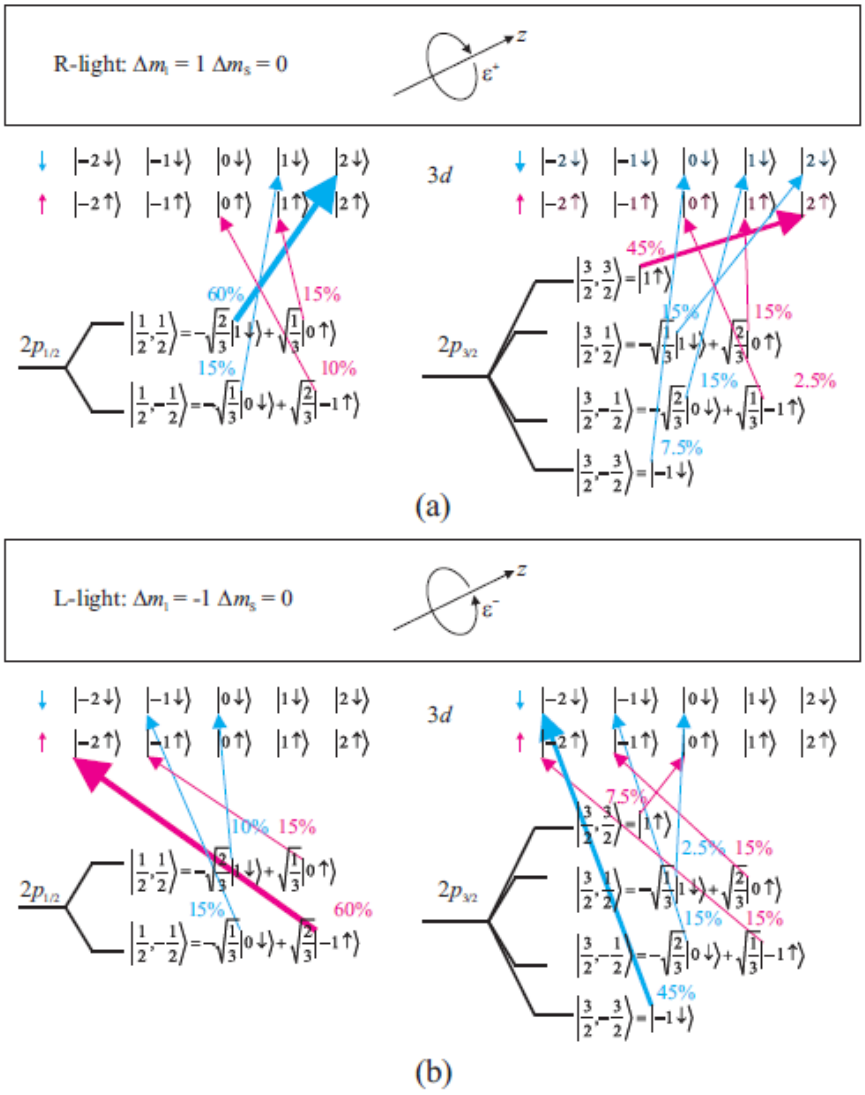

***Figure 3.4**: Schematic representation of allowed transitions and probabilities.*

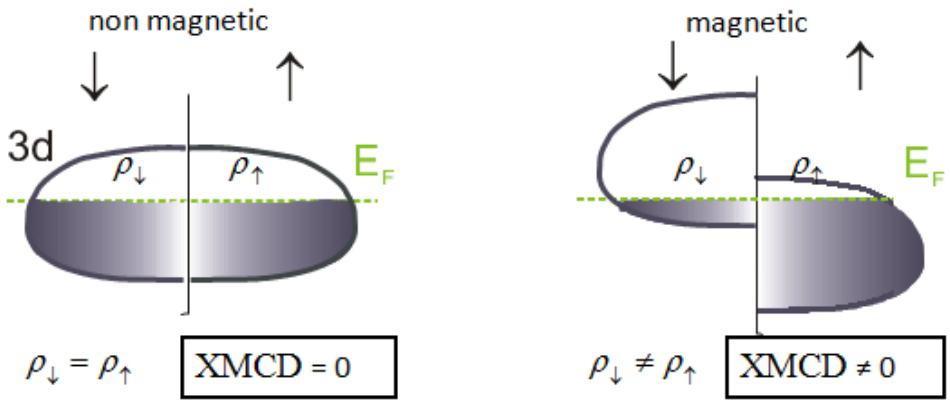

***Figure 3.5**: Schematic representation of 3d bands exchange splitting induced by the presence of a net magnetization.*

In a case as the one presented in *Figure 3.5*, right panel, the favored transitions are the ones that involve states with predominant minority carriers.

In particular, according to what discussed earlier, these are the transitions at the L_3 absorption edge for R ($P_{R,up}(L_2)$ = 25%) and at the L_2 for L ($P_{L,up}(L_2)$ = 75%) polarization. In this way, the exchange splitting final states are acting as a filter for the spin of the excited photoelectrons. We remind that for convention the photon helicity is taken to be positive (negative) when parallel (antiparallel) to the photon propagation direction, corresponding to R (L) polarization. In the case of our experiment the external magnetic field, applied along the photons propagation direction, is used to align the system magnetization parallel or antiparallel. The maximum dichroism is present when the sample magnetization is aligned with the photon direction. If there is an angle θ between the two, then the XMCD signal is reduced by a factor $\cos\theta$ and in this case the effective magnetization in the direction of the incident beam should be considered.

In summary, due to sample magnetization we will have an increasing of the L_2 edge intensity for R polarization if compared with L polarization. In the same way L_3 intensity is higher in antiparallel than in parallel coupling.

The exchange splitting final states are then acting as a filter for the spin of the excited photoelectrons. We note that by convention the photon helicity is taken to be positive (negative) when parallel (antiparallel) to the photon propagation direction, corresponding to R (L) polarization.

For a given orientation of the magnetization **M** with respect to the photon helicity, we will then have an increase of the L_2 edge intensity for $\boldsymbol{\epsilon}$ parallel to **M** if compared with the antiparallel condition. In the same way L_3 intensity is higher in antiparallel than in parallel coupling.

Therefore a non-vanishing XMCD signal is obtained by the difference of the two XAS spectra with R and L polarized light. It clearly follows that the XMCD signal is proportional to the imbalance between majority and minority 3d states above the Fermi level, and so it is proportional to the sample magnetization.

Similarly, if the d valence shell possess an orbital momentum, it will act as an orbital momentum filter for the excited photoelectrons that will also contribute to the dichroic signal.

In *Figure 3.6* absorption spectra for Cobalt nanostructures on graphene/SiO2/Si^{++} are reported. A measured background signal of the clean graphene/SiO2/Si^{++} substrate has been subtracted. The spectra have been recorded for R and L circular polarized light, and from the intensity of the XMCD signal it is evident that the absorption process is different in the two cases, indicating the presence of a spin imbalance in the Co 3d band.

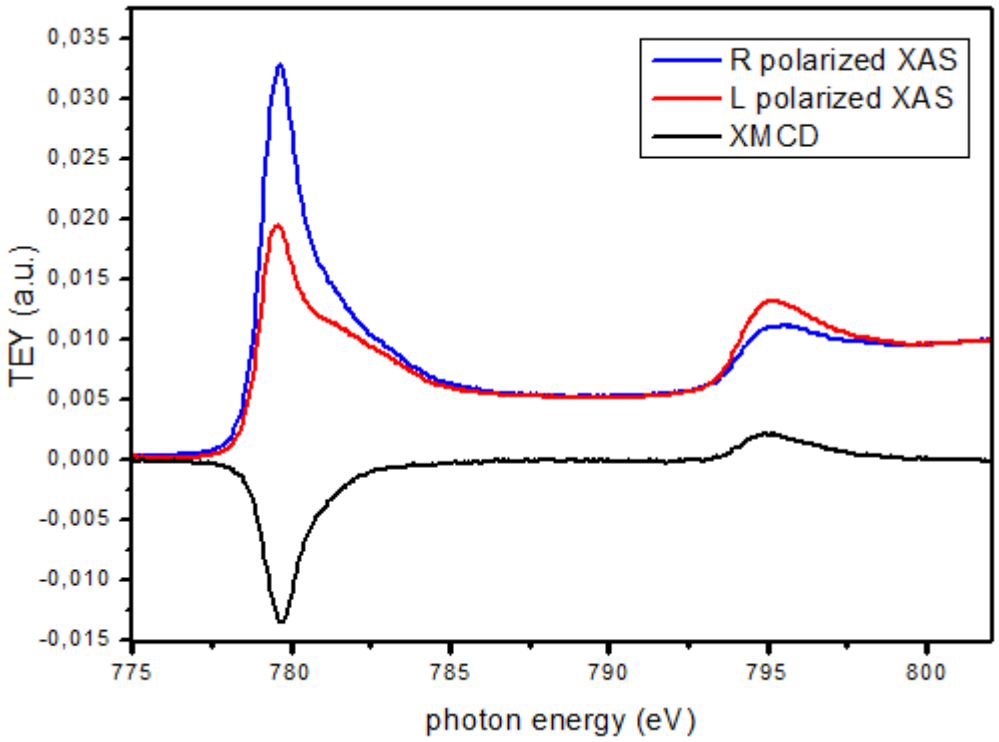

***Figure 3.6**: Positive and negative circular polarized XAS spectra and XMCD signal of Co nanostructures on graphene/SiO_2/Si^{++}. Measurements performed at ID08 beamilne (ESRF), 10K.*

In order to complete our description of XMCD technique, it is important to notice that given an experimental set of data, is it possible to use the so-called "sum rules" to extract the orbital and the effective spin contribution to the magnetic moment from an XMCD spectrum [66].

Sum rules are not discussed here, since they have not been used in our data analysis, where the ground state magnetic moment of the system have been found after comparison to simulated spectra.

3.1.3. XLD spectroscopy

In X-ray Linear Dichroism (XLD) spectroscopy linear polarized light ($\boldsymbol{\epsilon^0}$) is used, and XLD signal is defined as the difference between XAS recorded with light polarized horizontal or vertical with respect to the surface plane.

A proper treatment of XLD technique is beyond the aims of this thesis. In the following we will just stress how XLD can be used as a tool for determining the orientation of adsorbed molecules with respect to the substrate, since the intensity of the resonances in the XAS spectrum changes with the angle between the electrical field vector of the light and the orientation of the orbitals of the adsorbed species.

This is based on the fact that the resonances intensities in XAS are proportional to the absorption cross-section (3.4), which has a strong angular dependence through the matrix element. More precisely the angular dependence arises from the scalar product of the electrical field vector related to **A** (or indirectly to ϵ, once introduced the dipole approximation) and the linear momentum operator **p** (depending on **r**). The cross-section is then maximal when the dipole matrix element is oriented along the final state orbital.

It is even possible to make an accurate determination of the angle between the molecules and the surface. An experiment for the determination of the molecular tilt angle involves measuring intensity changes of a particular absorption resonance as a function of the x-ray incidence angle with respect to the normal to the sample.

In our experiments we made use of XLD measurements at both the cobalt $L_{2,3}$ and nitrogen *K* absorption edges.

3.1.4. Measurement methods

It has been proved that the X-ray absorption cross section is directly proportional to the number of holes created during the process [71]. It is then possible to quantitatively express the X-ray absorption process by simply measuring the core holes generation. For that purpose, different processes can be used.

The XAS spectra can be acquired (i) by direct transmission, recording the light intensity transmitted through the sample, or (ii) by measuring fluorescence [72] or (iii) Auger electrons [71] obtained from the decay of the excited state created by the photon absorption.

In fluorescence measurements emitted photons are collected, while in the Auger process the signal is due to electrons, and we refer to it as the Total Electron Yield (TEY).

Since we are working with soft X-rays, transmission acquisition requires very thin samples, so that fluorescence and TEY are more suitable for experiments involving *in-situ* preparation, since they allow using less fragile bulk samples.

In experiments in which surface sensitivity is required, such in our case, TEY is preferable compared to fluorescence. The latter, indeed, is more affected by contributions from the bulk substrate, since the escape depth of photons is greater (for example some microns in the case of the used SiO_2) compared to the electrons one which is in the order of few nm. Moreover, Auger emission is the primary decay process in the energy range of soft X-rays. It is then clear why TEY has been chosen to collect the XAS spectra in the case of our experiment.

In *Figure 3.7* a schematic representation of the TEY technique is presented.

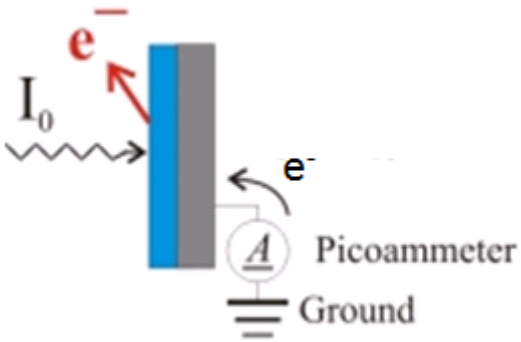

***Figure 3.7**: Schematic representation of TEY technique. The photon incident flux I_0 causes the emission of electrons due to Auger effect, the sample is grounded and emitted electrons at the surface are recorded by an amperometer.*

The absorbed X-ray intensity is measured by collecting the drain current on the sample due to photoelectrons created by the Auger process. It is interesting to notice that the main signal in not due to the primary Auger electrons, since while they are leaving the

sample, they create a cascade of scattered secondary electrons which dominate the TEY intensity, as explained in *Figure 3.8*.

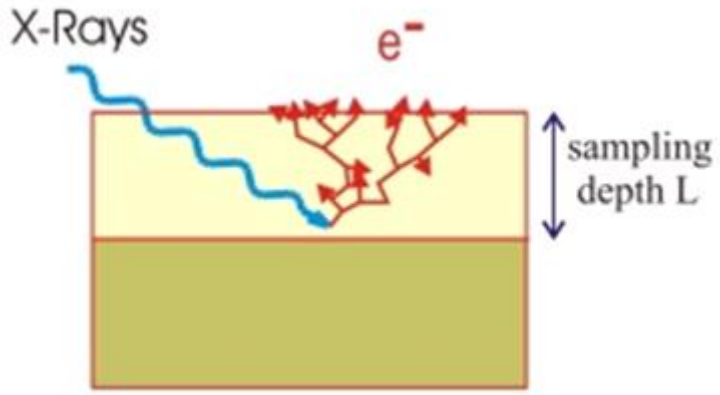

***Figure 3.8**: Schematic representation of TEY signal generation. Incident X-rays induce Auger electron emission, that are responsible of a cascade generation of secondary electrons due to scattering process along their path thought the surface.*

Finally, it has been demonstrated that, as long as the condition of no saturation effects is verified, the TEY current is proportional to the product between the absorption cross section and the energy ($\sigma(E) \cdot E$) [73]. Since saturation effects occur when the mean free path of electrons inside the material is larger or comparable to the penetration depth of the X-ray [74], we can assume that in the case of our experiments the intensity of the emitted Auger electrons and induced secondary electrons cascade, and so the TEY signal, can be considered as a direct measurement of the absorbed X-ray intensity.

3.2. Experimental apparatus for X-rays studies

ID08 is the beamline of ESRF dedicated to soft X-ray spectroscopy. The use of an undulator insures the possibility to measure with variable light polarization, linear and circular. This beamline was found to be the only suitable laboratory for the experiment reported in this thesis.

Indeed, it offers the opportunity of having (i) high intensity, very stable soft x-rays

necessary to observe transitions from *2p* to *3d* states as well as the nitrogen *K* edge, (ii) a high field magnet required for performing magnetic analysis with XMCD technique at liquid helium temperatures, (iii) the possibility of changing sample orientation relatively the X-ray beam direction in order to investigate XAS at different incidence angles, (vi) a surface facility directly connected to the magnet chamber so that samples can be prepared and characterize *in-situ*, (vii) the possibility of performing XMCD and electronic transport measurements on the same sample by means of a sample holder provided of electrical contacts.

In the following these features as well as the sample preparation will be discussed in more details.

3.2.1. The high field magnet and STM probe station at ID08

The experimental apparatus at ID08 beamline is mainly constituted by two elements: (i) the high field magnet (HFM) probe station and (ii) the sample preparation facilities characterized by the presence of the Scanning Tunneling Microscopy (STM) probe station.

The high field magnet system in mainly constituted by an ultra high vacuum (UHV) cold bore superconducting split-coil magnet (Oxford instruments). The magnet produces a variable ±5T magnetic field in the direction of the incident X-ray beam propagation, so that standard XMCD measurements can be preformed. An important propriety of the system is the possibility of rapidly changing the magnetic field up to a speed of 5T per minute. Together with the possibility to continuously scan the beamline energy, the high ramping speed allows to achieve a very rapid XMCD signal acquisition (about 2 minutes for each scan).

The sample is connected to the cold finger of the magnet by means of a suitable sample holder, and its temperature can be varied from 8K up to room temperature due to the presence of an integrated open flow He^4 cryostat where He flow and heat power can be controlled in order to get the desired sample temperature.

The sample can be rotated with respect to the beam, from normal incidence to almost

grazing incidence.

Recently a new sample holder with multiple electrical contacts has been developed which makes possible to combine X-ray absorption with electrical transport measurements. This tool has been particularly useful in the case of our experiment, since we were able to perform *in-situ* field effect measurements, in order to monitor sample proprieties throughout the absorption experiment. For a detail discussion of the system we refer to Appendix C.

In *Figure 3.9* a photo of the high field magnet probe station and of the sample preparation facilities is also shown.

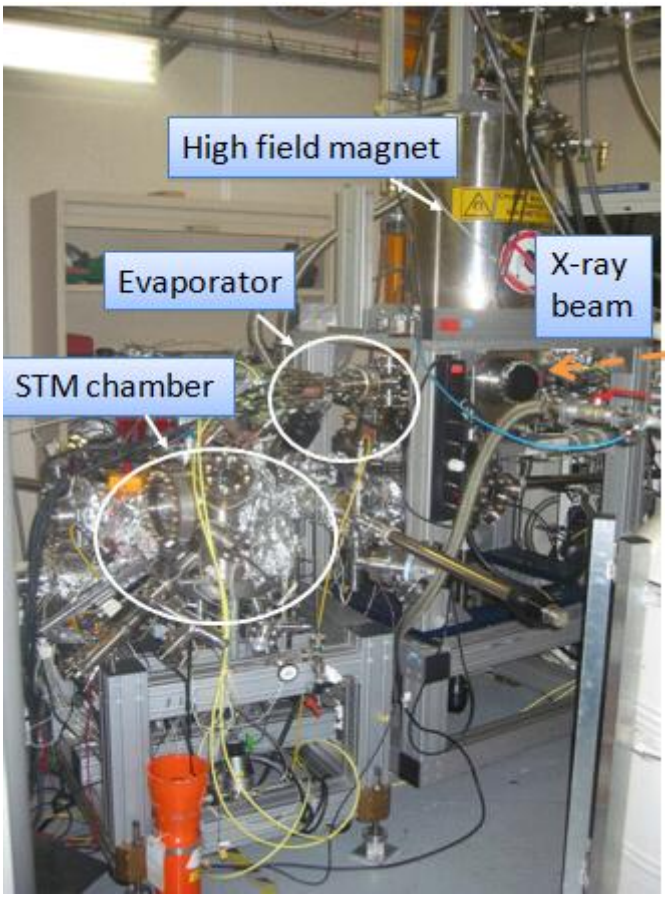

***Figure 3.9**: The High field magnet probe station and sample preparation facilities at the ID08 beamline, ESRF.*

Concerning the sample preparation facilities, below the high field magnet chamber there is a small preparation chamber equipped with a load-lock that allows to introduce two

sample holders without breaking the vacuum in the system. Vacuum ports are also available in the high field magnet and in the preparation chamber that can be fitted with *ad hoc* instrumentation required for experiments. In the case of our experiment a molecular evaporator and a heater have been mounted in the preparation chamber.
A second preparation chamber, the STM chamber, is connected to the first one again without breaking the vacuum, which is in the order of 2×10^{-10} mbar in the magnet chamber and in the STM chamber, and around 1×10^{-9} mbar in the preparation chamber. An STM and an analyzer for LEED (low electron energy diffraction) and Auger spectroscopy are located in this more sophisticated preparation chamber, where samples can be even cleaned by sputtering with Ar gas and annealed up to 2000°C.

3.2.2. CoPc deposition and calibration

The presence of a sample preparation facility directly connected to the high filed magnet chamber allows *in-situ* deposition of CoPc molecules on HOPG and graphene substrates.
Molecules have been deposited from a crystalline powder phase, at room temperature and in UHV conditions. The technique used is evaporation, which is classified as a physical vapor deposition technique (PVD) and consists in a very simple process, in which the desired material is heated until it reaches its boiling or sublimation (as in the case of CoPc) point. The deposition in performed in vacuum conditions, so that the evaporated molecules have a long mean free path and can therefore travel straightly until they reach the target (in our case the HOPG or the graphene substrate) and condense on it.
Since CoPc molecules have been found to be a very stable system it has been possible to deposited them at room temperature, whereas in the case of single atoms evaporation low temperature conditions are required, in order to make them condensate on the target as soon as they reach it, without diffusing on the surface and forming clusters. Indeed, the central Co ion in CoPc is somehow "protected" by the surrounding molecular ligands, so that Co ions from different molecules are not in direct contact with each other. In that way, possible molecular diffusion and interaction on the target surface at

room temperature do not dramatically change the surrounding environment for single Co ions, that remains isolated and do not interact with each other.

To perform the deposition, a properly designed molecular evaporator has been connected between the small preparation chamber and the STM chamber by means of one of the available vacuum ports. The evaporator is formed by a quartz crucible surrounded by a metal filament. A power supply is used to flow a current into the filament and Joule heating of the filament increases the temperature in the crucible in which the molecular powder is located. The aperture where CoPc molecules are passing thought once evaporated is shaped in order to collimate the molecules flux in the direction of the target and can be closed by a shutter once the deposition process is ended. The evaporator is equipped with a thermocouple, so that the temperature close to the crucible can be continuously monitored during the evaporation. Before deposition, the evaporator has to be degassed at a temperature slightly higher than the one used for deposition ($\sim 420°C$), so that no impurities are introduced during the *in-situ* sample preparation.

A calibration has been done in order to determine the deposition parameters, such as (i) the evaporation temperature, and consequently the current applied to the filament, and (ii) the evaporation time required to obtain the desired coverage. The calibration procedure is very simple: the current in the filament is slowly increased until the crucible reaches a temperature close to the expected sublimation temperature of the Co-Pcs, then a first evaporation run (usually a few minutes) is performed. STM is used to check the presence of molecules on the target at the end of the deposition. If no molecules are found on the substrate, the crucible temperature is increased and the procedure repeated, until the correct evaporation temperature is determined. In the present experiment, the evaporation temperature was found at 400°C with a 2.26A current flowing in the filament.

Maintaining the temperature fixed at 400°C, the deposition time was varied, to achieve the desired molecule coverage. A single crystal of Cu(001) has been used as a substrate during calibration, since CoPc molecules are particularly stable on this substrate and diffusion effects induced by the interaction with the STM tip are minimized, making easier the coverage estimation. The crucible has been kept at approximately 180°C, with

0.6A current for a long time before evaporation, in order to reduce fluctuations in deposition.

In *Figure 3.10* an STM image of clean Cu(001) surface is shown where large terraces separated by atomic step edges are clearly visible.

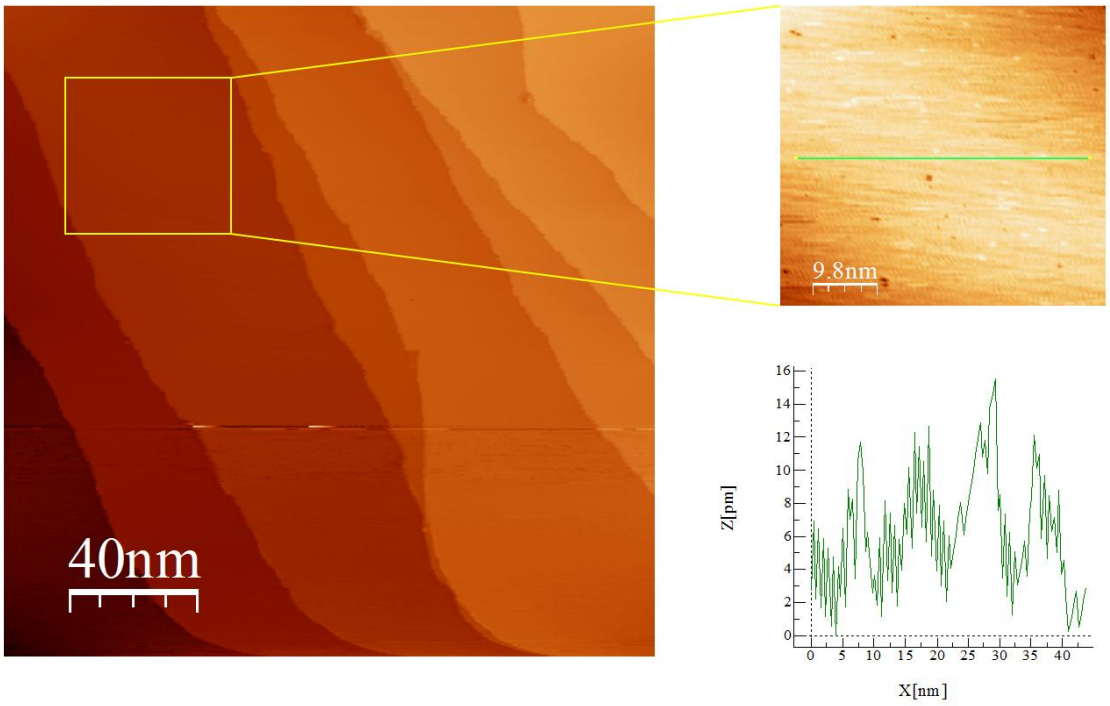

***Figure 3.10**: STM image of clean Cu(001) surface where terraces and atomic step edges are clearly visible. A zoom in and the height profile corresponding to the green line are also shown.*

STM images in *Figure 3.11*, *3.12* and *3.13* show CoPc molecules deposited on Cu(001) at 400°C at increasing evaporation time: 2, 5 and 10 minutes. In all 2, 5 and 10 minutes deposition samples, less than one monolayer of CoPc is deposited on the target surface. The amount of coverage can be roughly estimated as 5%, 10% and 18%, respectively. In the case of our experiment we decided to use 5' as deposition time.

Figure 3.14 shows an STM image of a few CoPc molecules on Cu(001) where the typical "flower like" structure formed by the central ion and the four isonodol rings is clearly distinguishable. The height profile indicates typical CoPc dimension, ~ 3nm in-plane diameter and ~1.4Å out-of-plane thickness.

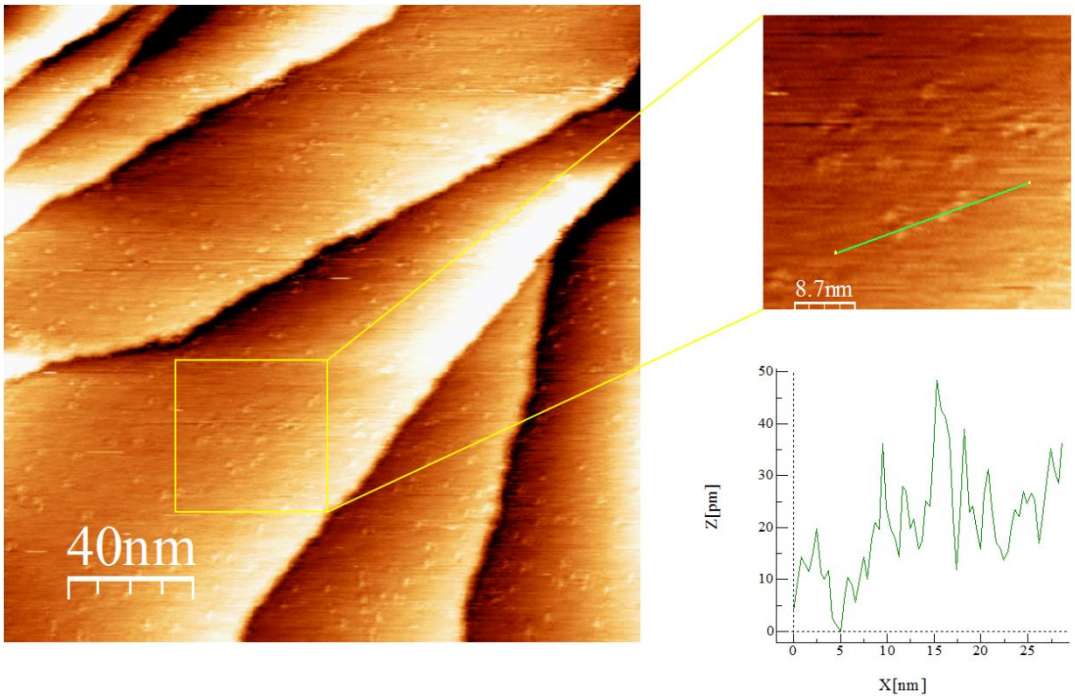

***Figure 3.11**: STM image of Co-Pcs deposited on Cu(001) surface at 400°C and 2' evaporation time. Molecules are clearly visible on the copper terraces. A zoom in and the height profile corresponding to the green line are also shown.*

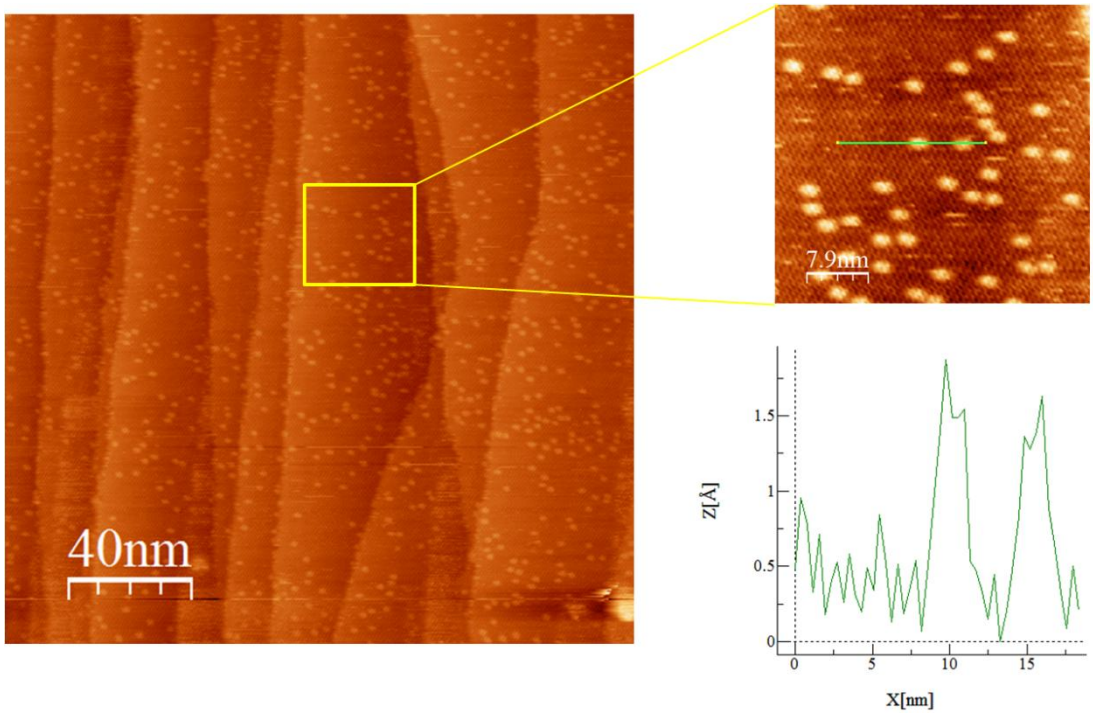

***Figure 3.12**: STM image of Co-Pcs deposited on Cu(001) surface at 400°C and 5' evaporation time. Molecules are clearly visible on the copper terraces. A zoom in and the height profile corresponding to the green line are also shown.*

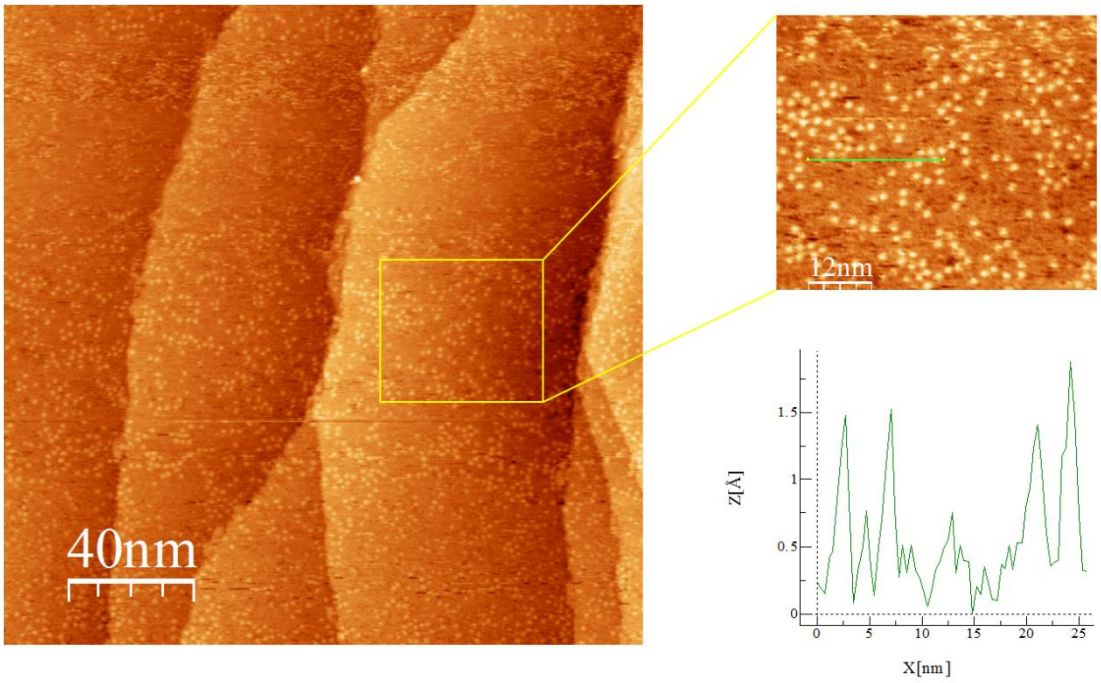

***Figure 3.13**: STM image of Co-Pcs deposited on Cu(001) surface at 400°C and 10' evaporation time. Molecules are clearly visible on the copper terraces. A zoom in and the height profile corresponding to the green line are also shown.*

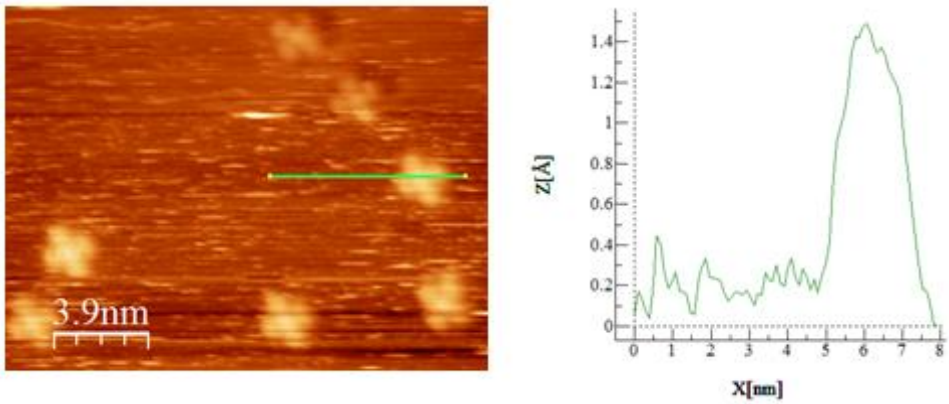

***Figure 3.14**: STM image of Co-Pcs deposited on Cu(001) surface at 400°C and 5' evaporation time. Molecular "flower-like" shape is clearly visible. The height profile corresponds to the green line.*

The sticking coefficient of CoPc on HOPG and graphene is not the same as on Cu(001) [35]. However, STM measurements (not shown) suggest that such differences affect the

calibration less than the intrinsic fluctuations due to the evaporation process itself[19]. Once calibrated the coverage by STM, we have also estimated the amplitude of the XAS signal at the L_3 absorption edge with respect to the background signal at the same energy (edge jump). This value has then been used as reference to check the CoPc coverage on graphene samples. Here in fact STM cannot be used, as the sample holder with electric contacts is not compatible with the STM samples receptacle.

In order to avoid impurities at the interface between CoPc and the substrates, the latter have been properly cleaned before deposition. HOPG samples have been either cleaved *ex-situ* or annealed in the STM chamber. No differences have been noticed for spectra obtained in the two cases. Concerning graphene samples, they have been produced with clean room techniques and the presence of possible defects and impurities has already been described in great details in paragraph 2.3.1, so that they have been low temperature (around $\sim$200° C) annealed, just to remove water absorbed from air. For this purposed a heater has been connected to the small preparation chamber thought a vacuum port, as already done for the evaporator. The heater has been developed and calibrated at the ID08 beamline and is simply constituted by a support in which the sample holder for the high field magnet can be connected. The support itself is surrounded by a resistive heater, in which a current ($\sim$1A) is flown to get Joule heating.

3.3. XMCD and XLD measurements of CoPc molecules on graphene

XAS and XMCD techniques have been used to investigate the electronic and magnetic properties of CoPc metal-organic molecules adsorbed on graphene, in order to probe charge transfer and hybridization effects.

XLD measurements have been performed as well, in order to characterize the

[19] Even using the same applied current, evaporation time and target, small differences in the amount of CoPcs deposited have been noticed during calibration. They can be due to variations in the distribution of the molecular powder inside the crucible, so that the local temperature or the orientation of the evaporated moleculas related to the crucible aperture can be slightly different.

adsorption geometry of the molecules on the substrate surface.

X-ray spectroscopy measurements have been performed at the Dragon beamline ID08 of ESRF using linearly and circularly polarized light tuned to the $L_{2,3}$ cobalt absorption edges situated at energies between 780 and 800eV. All the spectra were recorded at 8 K in total electron yield mode. XMCD measurements have been made under a 5T magnetic field. The angle θ between the normal to the sample and the beam direction was also varied in order to investigate the magnetic anisotropy, the molecules alignment with respect to the substrate, as well as the crystal field interaction of the Co ions due to the ligands. In particular, XMCD and XLD measurements have been performed at normal ($\theta=0°$) and grazing ($\theta=70°$) incidence.

The XAS (XMCD) signal here is taken as the average (difference) between the TEY signals recorded under negative (I^-) and positive (I^+) circularly polarized X-ray beam. The TEY is normalized to the reference signal taken on a gold mesh which is located after the last optical element just before the sample. As already seen, the XAS signal is proportional to the number of empty states, whereas the XMCD is proportional to the expectation value of the TM magnetic moment projected onto the X-ray incidence direction.

CoPc molecules were evaporated *in-situ* onto the desired substrate held at room temperature in ultrahigh vacuum. STM measurements of CoPc on Cu and HOPG substrates were used to calibrate the molecule coverage (for more details on the sample preparation we refer to paragraph 3.2).

3.3.1. CoPc on HOPG

First of all, spectra of CoPc molecules deposited on HOPG have been collected as a reference to investigate charge transfer effects with the substrate. In fact, as already seen before (see paragraph 1.1.1.2), graphite is a well known and easy to control system that presents the same hexagonal arrangement of carbon atoms on the surface as graphene. The CoPc are therefore expected to "sit" in a very similar way on the two substrates.

Due to the interaction between graphene layers in HOPG and in general in graphite, the linear dispersion of graphene is lost. Valence and conduction bands are parabolic and

they slightly cross at the Fermi level, making graphite a semimetal. Therefore, different to graphene the density of states at the Dirac point is not zero even in the undoped case (graphite is often referred to as a bad metal).

In *Figure 3.15* and *Figure 3.16* XAS and XMCD spectra from CoPc/HOPG are reported. Spectra have been collected at both normal (*Figure 3.15*) and grazing (*Figure 3.16*) incidence.

In the top part of the images, XAS spectra are reported before background subtraction together with the HOPG background recorded before CoPc deposition. The cobalt L_3 and L_2 absorption edges are visible at 782 eV and 797 eV, respectively. The cobalt signal at the L_3 absorption edge is quite small, about 1% of the background signal and this is a consequence of the small amount of molecules deposited on the sample. Following the calibration presented in the paragraph 3.2 we can assume roughly 10% of a monolayer of coverage. It is then important to notice that the amount of Co ions is significantly lower, since only a small percentage (∼5% [28]) of the molecular surface is constituted by the Co ions, most of the CoPc is in fact occupied by the isonodol rings (for more details about the molecular structure we refer to paragraph 1.2.2).

In the bottom panels of *Figure 3.15* and *Figure 3.16* the XMCD signal and the XAS signal after subtraction of the HOPG background are shown. It is clearly evident the typical multiplet splitting in XAS arising from the core-hole excitation (see paragraph 3.1.1.2). These spectroscopic features are the fingerprint of the electronic configuration of the central Co ion and are related to the specific crystal field. Moreover, the finite XMCD signal in correspondence to the $L_{2,3}$ cobalt edges indicates the presence of a net *3d* magnetic moment localized on Co, related to the spin configuration. Careful analysis of the XAS and XMCD spectra can help understanding the electronic configuration of the central Co atom.

The spectra are very similar to analogous measurements reported for thick CoPc films deposited on metals, an example is presented in *Figure 3.17* from Ref. [28]. Thick films are considered a good approximation for a free CoPc molecule, since apart from the very first layer which is in contact with the substrate, the molecules in the following layers do not interact with the metallic substrate. In *Figure 3.17* simulated spectra from ligand field multiplet calculations are also shown.

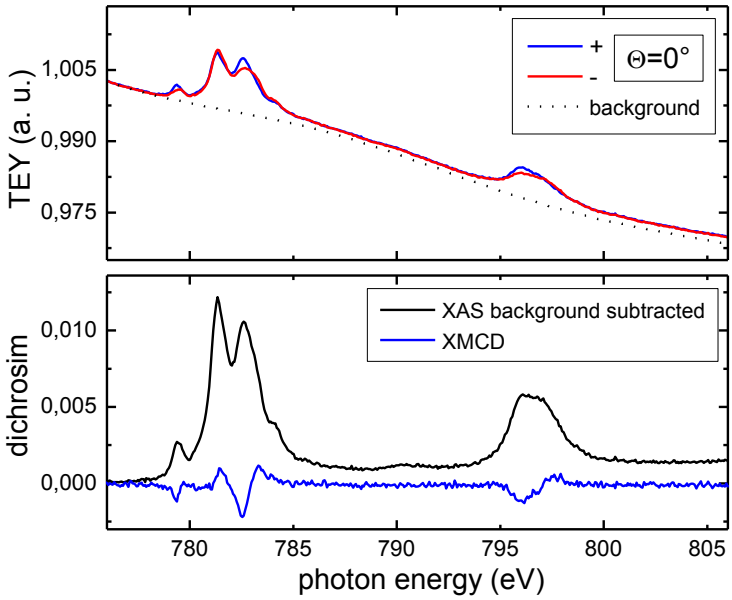

***Figure 3.15**: Circularity polarized XAS and XMCD spectra for CoPc deposited on HOPG at normal incidence. In the top panel as-measured absorption spectra taken with positive (+) and negative (-) circular polarized light are presented, together with the HOPG background spectra measured before CoPc deposition. In the bottom panel the XAS after background subtraction and XMCD spectra are shown.*

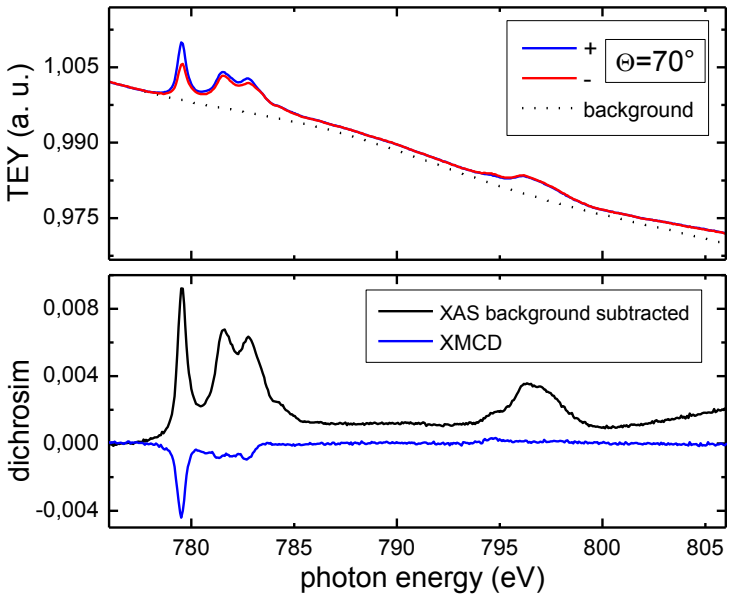

***Figure 3.16**: Circularity polarized XAS and XMCD spectra for CoPc deposited on HOPG at grazing incidence. In the top panel as-measured absorption spectra taken with positive (+) and negative (-) circular polarized light are presented, together with the HOPG background spectra measured before CoPc deposition. In the bottom panel the XAS after background subtraction and XMCD spectra are shown.*

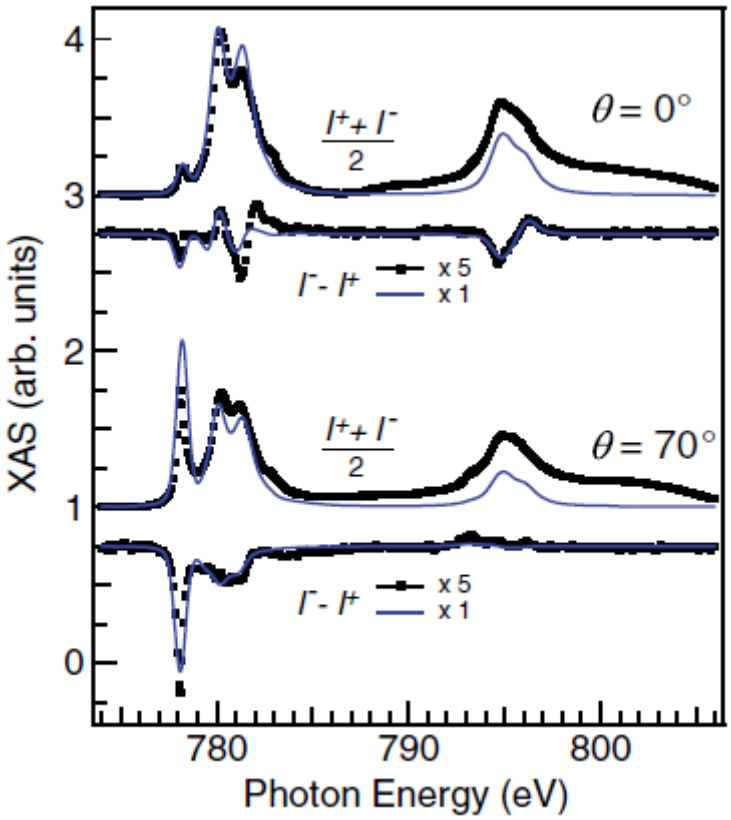

***Figure 3.17**: Circularity polarized XAS and XMCD for CoPc multilayer on Au(111) from experiments (dotted line) and simulated (solid line). Extracted from Ref. [28]*

In Ref. [28] it was found that both experimental XAS and XMCD were reproducible by a $3d^7$ configuration for Co ions and a D_{4h} crystal-field symmetry with parameters $10D_q$ = 2.3 eV, D_s = 0.55 eV, D_t = 0.20 eV and 75% reduction of the Slater-Condon integral [75]. This corresponds to the many electrons ground state symmetry $^2A_{1g}$, with a $(e_g)^{3.8}(b_{2g})^2(a_{1g})^{1.2}$ configuration, as already presented in paragraph 1.2.2. The analysis in [28] also showed that the non-vanishing magnetic moment is due to the almost half-filled out-of-plane a_{1g} orbital, while the depopulation of the e_g states, due to spin-orbit coupling which is responsible for the mixing between the molecular ground state and the first excited state, creates a finite in-plane orbital momentum, which is reflected by the larger amplitude of the integrated XMCD signal at grazing incidence compared to normal incidence.

In the case of our experiment, as already mentioned the multiplet splitting structures are very similar to what found in [28], especially the peak distribution and relative

intensities in the XMCD signal. Therefore, it is reasonable to use the same interpretation. The only difference found in our case, is a larger value of the intensity of the XMCD signal, which is more than two times what found in [28]. For a thick multilayer, the XMCD intensity is reduced compared to the simulations due to an antiferromagnetic (AFM) coupling between stacked CoPc molecules once formed the thick film. In our case instead, as the amount of molecules is well below one single layer, the AFM coupling is not present and the averaged magnetization is therefore larger than what observed in a thick film.

We can then conclude that CoPc molecules deposited on HOPG interact very weakly with the substrate and no charge transfer effect is present.

This conclusion is also in accordance with what already seen for other kinds of MePc (in particular FePc) deposited on graphite [76]. Indeed, it has been shown with Photoemission Spectroscopy (PES) measurements that FePc molecules are weakly bounded on a graphite substrate (Van der Waals forces).

Another interesting piece of information about the orientation and structure of CoPc molecules on graphite can be obtained from XLD data recorded at the K edge of nitrogen and at the $L_{2,3}$ edges of cobalt. In *Figure 3.18* and *Figure 3.19* XLD spectra recorded at grazing incidence for CoPc deposited on HOPG at the nitrogen *K* edge and cobalt $L_{2,3}$ absorption edges are presented.

XAS measurements are taken with the electric field vector polarized either parallel (v: vertical) or almost normal (h: horizontal) to the surface plane. The XLD signal is calculated as the difference between the two.

As far as it concerns the linear dichroism at the cobalt $L_{2,3}$ edges, at grazing incidence, from *Figure 3.19* we notice a strong difference in the XAS signals taken with different kind of linear light polarization. This strong natural linear dichroism is also reflected in the different shape of the XAS signal taken with circular polarized light at normal and grazing incidence (see *Figure 3.15* and *Figure 3.16*) and it is due to the reduced-symmetry environment of the Co ion within the Pc molecule, confirming the presence of a net crystal field splitting.

In the case of the nitrogen *K* edge, shown in *Figure 3.18*, the absorption spectra are characterized by multiple absorption peaks, as better explained in the insert.

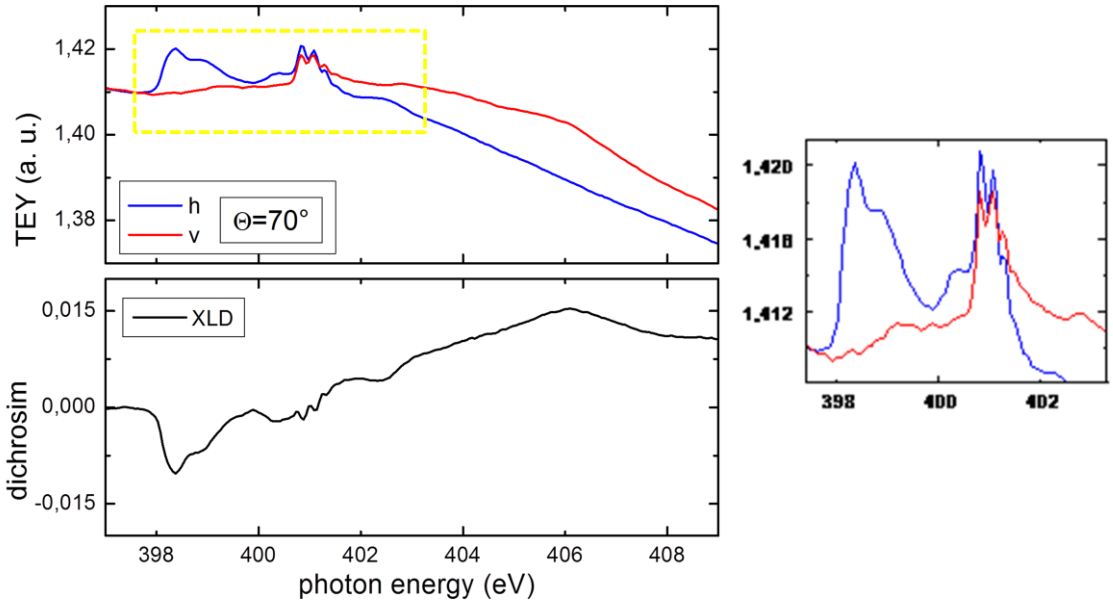

***Figure 3.18**: XLD spectra from CoPc on HOPG at the nitrogen K absorption edge measured at grazing incidence. The upper panel is dedicated to linear polarized absorption with horizontal and vertical polarization, while in the lower panel the linear dichroism is presented. The zoom is related to the region squared in yellow.*

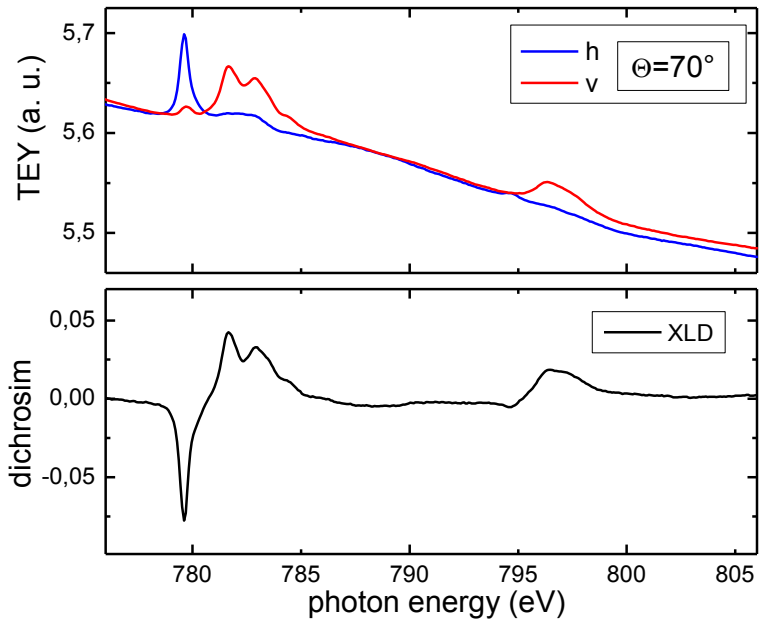

***Figure 3.19**: XLD spectra of CoPc on HOPG at the Co $L_{2,3}$ absorption edges, measured at grazing incidence. In the first panel linear polarized absorption with horizontal and vertical polarization is presented, while the second panel is dedicated to the linear dichroism.*

Multiple peaks in the absorption spectra of nitrogen *K* edges are associated to transitions from the nitrogen 1*s* core level to the empty states localized on the isoindole structure of the molecule, constituted by benzene and pyrrole macrocycles. These states present both a π^* and σ^* character.

In particular, the main unoccupied level in these molecules is formed by π^* states delocalized mainly on the pyrrole macrocycles, which can be reached by adsorption transitions from the *1s* initial state of nitrogen [30]. The multi-peak structure visible around 400.8 eV is due to the presence of a very tiny amount of N_2 gas in the measurements chamber which is physisorbed on the sample at cryogenic temperature and it disappears at room temperature.

There is a clear dichroic effect at the nitrogen *K* edge for the two polarizations, with distinct polarization dependence on the π^* and σ^* resonances. Due to the different orientation of these states related to the plane of the molecule, the observed dichroism suggests a planar orientation of the CoPc molecules. In fact, horizontal polarized light interacts mainly with the out-of-plane π^* unoccupied orbitals, while vertical polarized light interacts only with the in-plane σ^* unoccupied orbitals.

This is in accord with what is generally observed for molecules presenting such π-conjugated structure. Once deposited on metal substrates, they are generally adsorbed in a planar configuration and they are found to lie flat on the substrate surface [30]. Also in the specific case of CoPc adsorbed on metals such as Au(111), Cu(111) and Au(110), both molecular single layers and multilayers have been experimentally proved to lie flat on the substrate, at least until a critical deposited multilayer thickness (in the order of some nanometers) has been reached [35].

For a better understanding, the linear polarized XAS signals of CoPc molecules on Au(110) are reported in *Figure 3.20* from Ref. [30] for both single layer and multilayer of CoPc. In both cases the dichroic behavior is clearly distinguishable. In *Figure 3.20* a dashed line is used to divide the energy range for π^* and σ^* related resonances. As already seen, the former are located at lower energies and interact with horizontal polarized light, while the latter are located at higher energies and interact with vertical polarized light. It is interesting to notice that qualitatively single layer and multilayer CoPc on Au(110) display a very similar structure, meaning that the interaction with the substrate does not sensitively modify the ligands geometry.

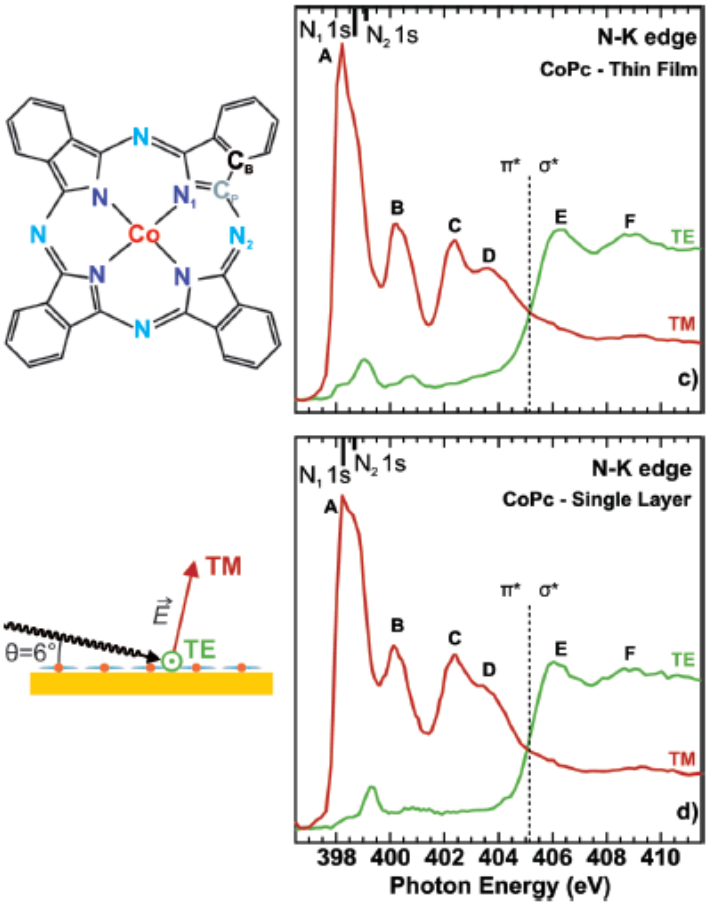

***Figure 3.20**: Nitrogen K edge linear polarized XAS data for the CoPc/Au(110) system at the thick film (a) and single layer (b) coverage. Image extracted from [30].*

From a comparison between *Figure 3.20* for CoPc/Au(110) and the insert in *Figure 3.18* for our CoPc/HOPG system, we can clearly see strong similarities in the π-related region of the spectra, in particular we can both recognize the presence of the A peak (see *Figure 3.20*) located at 398.35 eV, with the related shoulder at 398.85eV, and the B peak (see *Figure 3.20*) at 400.36 eV. Peak C and D, presented in *Figure 2.20*, are not clearly distinguishable due to presence of the multi-peak structure of the N_2.

In our spectra it is more difficult to clearly distinguish σ-orbitals related features, that even in the case of *Figure 3.20* are less pronounced. This could be due the presence of a strong signal coming from the background. It is also important to point out that our XAS signal in much lower than the one recorded for the spectra in *Figure 3.20*, since we are studying molecules in a diluted regime, instead of monolayers or multilayers. Thus, it is reasonable to assume a flat geometry of the CoPc molecules on HOPG, as

even confirmed by *Figure 3.19*.

It is even interesting to notice that the same experiments have been repeated using different coverage of CoPc on HOPG, always depositing less than one monolayer, and no evidence of different behaviors or appearance of coverage-dependent features have been noticed. This indicates that the eventual proximity of CoPc molecules does not affect the ligands and metal center electronic configuration.

3.3.2. CoPc on graphene/SiO_2/Si^{++}

After explaining in detail the "model" case of CoPc on HOPG, we move now to the analysis of CoPc molecules deposited on real graphene substrates with different doping levels. This paragraph is dedicated to strongly hole doped graphene whereas the next one will be focused on strongly electron doped graphene.

XAS and XMCD spectra of CoPc molecules on graphene/SiO_2/Si^{++} are presented in *Figure 3.21*, for normal incidence, and *Figure 3.22*, for grazing incidence.

From a comparison with the already shown spectra of CoPc deposited on HOPG, we can easily identify the same multiplet structure and the same ratio between peaks in the XMCD signal, at both incidence angles. This result suggests that the ground state of the molecule and the spin configuration are the same in the two systems.

The average XAS signal is also quite similar in the two systems at normal incidence, but tiny differences are seen at grazing incidence in the relative intensity of the peak at about 780 eV compared to the double peak structure at higher energy which is a bit lower for CoPc on HOPG. These differences are probably related to small variations of the linear natural dichroism in the two systems.

XLD measurements at grazing incidence for Co and N are reported in *Figure 3.23* and *Figure 3.24.* For both elements the shape of the linear dichroic signal is very similar to what already observed for CoPc molecules deposited on HOPG, suggesting that the molecule electronic configuration and geometry does not present large differences in the two cases. However, in agreement to what already observed for the XAS at grazing incidence, the order of magnitude of the dichroic effect is slightly smaller in the case of CoPc on SiO_2/Si^{++}.

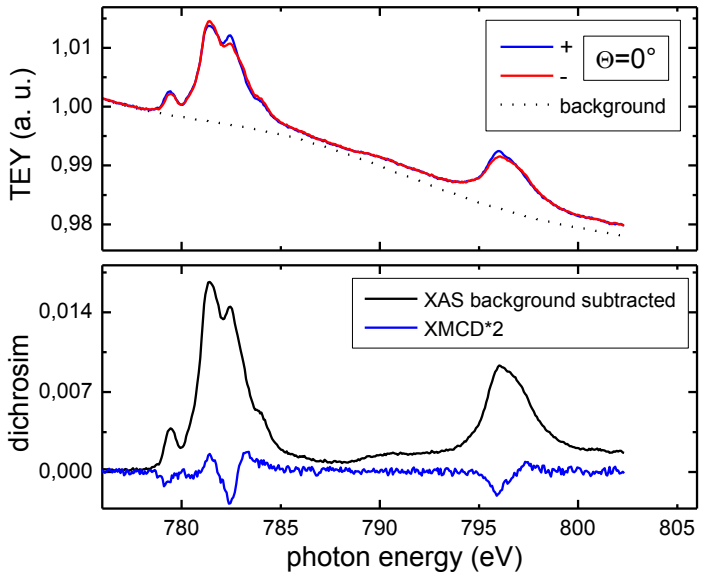

***Figure 3.21**: Circularity polarized XAS and XMCD for CoPc deposited on graphene/SiO_2/Si^{++} at normal incidence. In the top panel as-measured absorption spectra taken with positive (+) and negative (-) circular polarized light are presented, together with the HOPG background spectra measured before CoPc deposition. In the bottom panel the XAS after background subtraction and XMCD spectra are shown.*

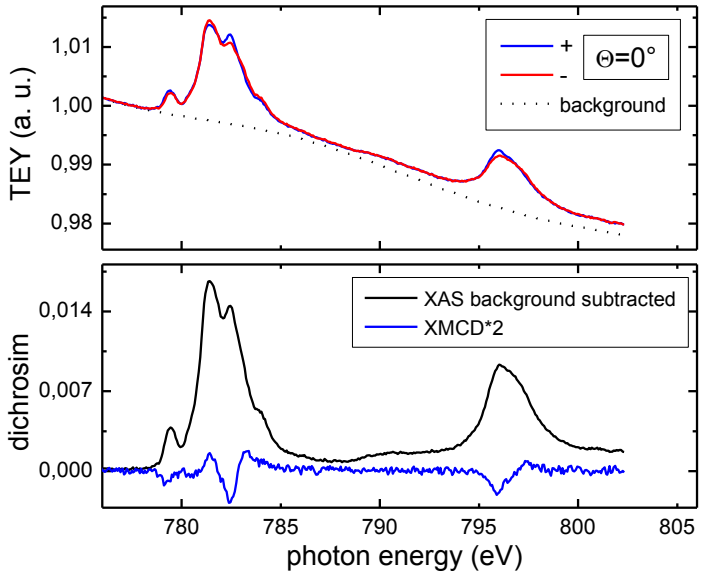

***Figure 3.22**: Circularity polarized XAS and XMCD for CoPc deposited on graphene/SiO_2/Si^{++} at grazing incidence. In the top panel as-measured absorption spectra taken with positive (+) and negative (-) circular polarized light are presented, together with the HOPG background spectra measured before CoPc deposition. In the bottom panel the XAS after background subtraction and XMCD spectra are shown.*

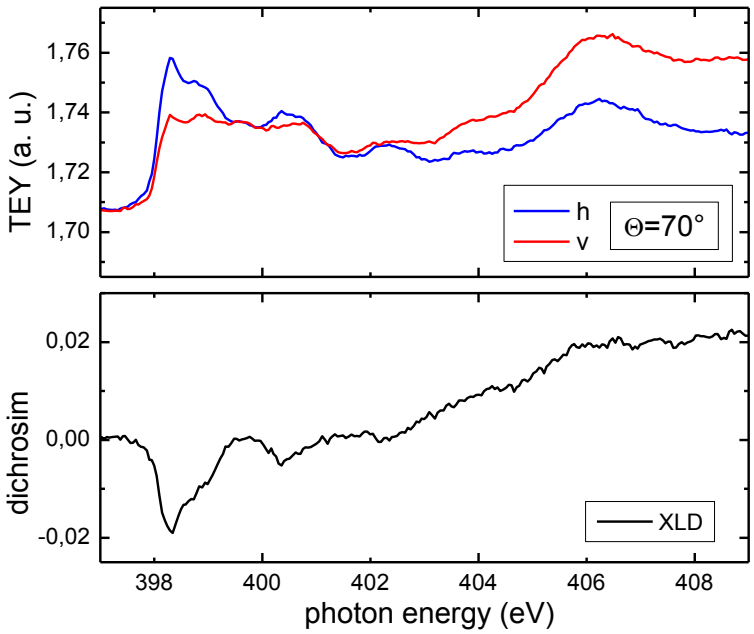

***Figure 3.23**: XLD spectra from Co-Pc on graphene/SiO_2/Si^{++} at N edge and grazing incidence. The upper panel is dedicated to linear polarized absorption with horizontal and vertical polarization, while in the lower panel the linear dichroism is presented.*

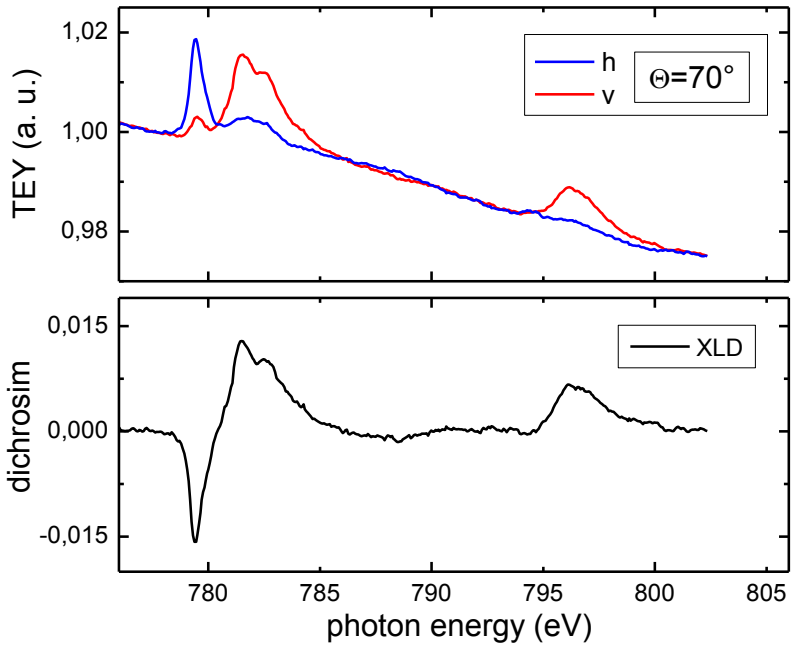

***Figure 3.24**: XLD spectra from Co-Pc on graphene/SiO_2/Si^{++} at Co edge and grazing incidence. In the first panel linear polarized absorption with horizontal and vertical polarization is presented, while the second panel is dedicated to the linear dichroism.*

We tentatively attribute these tiny differences observed, in both XAS and XLD, at grazing incidence to the presence of small areas with residual PMMA where the molecules, following the substrate roughness, assume different orientations with respect to the surface normal. This effect would only decrease the intensity of the linear dichroism but not the shape, as the electronic configuration is not altered, coherently with what we observe.

We have also tried to fit the experimental Co XLD measurements with simulated spectra, using the program CTM4XAS [77]. The simulations are mainly based on semi-empirical atomic multiplet calculations, for determining the ground state of the central ion and the accessible final excited states, combined with crystal field theory and ligand charge transfer theory, in order to take into account possible interaction with neighboring atoms and with the substrate. The model is based on symmetries and therefore does not allow to calculate the spectra corresponding to magnetization off the symmetry axis. However, it allows an estimation of the linear dichroism.

In *Figure 3.25* and *Figure 3.26* the experimental and simulated XLD spectra are reported for both CoPc on HOPG and CoPc on graphene/SiO_2/Si^{++}. We have used a D_{4h} symmetry and a d^7configuration, as found in [28], and the following parameters: $10D_q$ = 2.65eV, D_t = 0.2eV, D_s = 0.55eV, Slater Reduction 75% and Gaussian broadening 0.2eV [75].

The same fit parameters reproduce well enough both spectra, confirming the idea that CoPc molecules present a very similar configuration on both substrates. The differences in simulation parameters between our simulation and those reported in [28] are very small, confirming that Co ions in CoPc on HOPG and on graphene/SiO_2/Si^{++} substrates are affected by a crystal field with the same symmetry and very similar intensity as found in CoPcs multilayers.

In [28] the electronic and magnetic configurations of the TM ion have been interpreted using a numerical code free of the symmetry restrictions that represent the limitations on CTM4XAS model. In the latter case, indeed, a proper simulation in case of coupled states is not possible [77].

It appears therefore to us that the code used in [28] and related model would be more suitable to simulate the XAS and XMCD spectra of our system, as also confirmed by the fact that the simulated XAS and XMCD for multilayer CoPc in [28], reported in

Figure 3.17, would provide a good fit for our data as well.

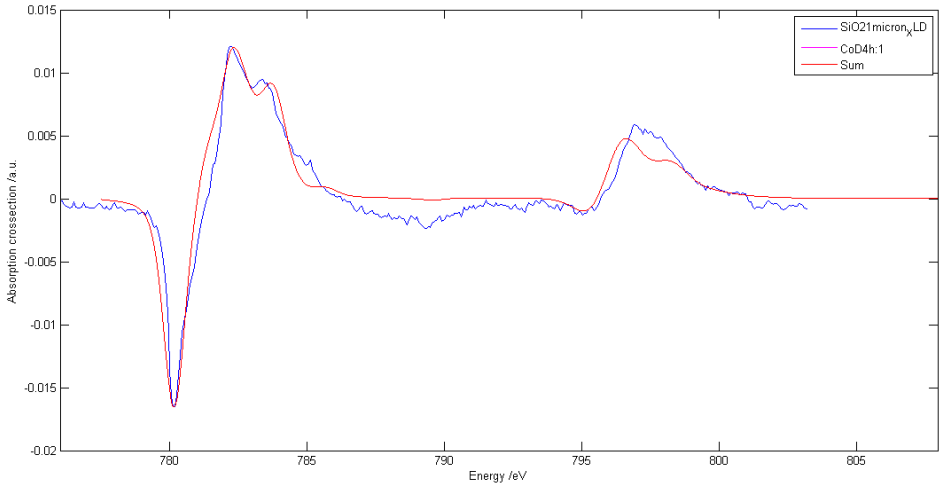

***Figure 3.25**: Co edge XLD from Co-Pc on graphene/SiO_2/Si^{++}. Experimental spectra (blue line) and simulated spectra (red line) are shown.*

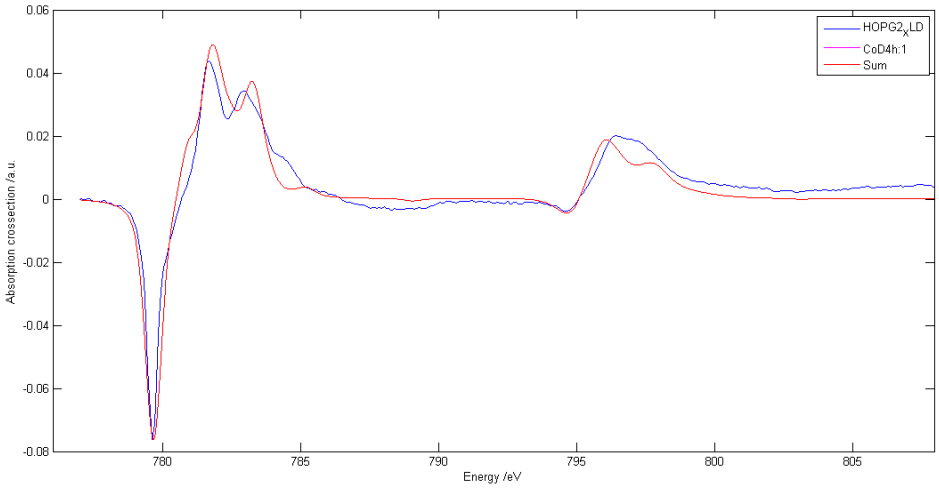

***Figure 3.26**: Co edge XLD from Co-Pc on graphite. Experimental spectra (blue line) and simulated spectra (red line)are shown.*

In summary CoPc molecules present a very similar magnetic and electronic configuration on HOPG and graphene/SiO_2/Si^{++} substrates. To our understanding, it means that mostly the CVD graphene surface looks like the HOPG surface with only a small percentage of extended defect areas which only have the effect of a slight reduction of the linear dichroism. The same interpretation can therefore be used to

conclude that CoPc molecules do not interact strongly with graphene/SiO_2/Si^{++} substrate and no evident charge transfer due to the substrate is present.
This also means that the different doping in the two substrates (graphene on SiO_2/Si^{++} is hole doped whereas HOPG is neutral but with a non vanishing density of states at the Fermi level) does not affect the interaction with adsorbed CoPc. As we will see in the next paragraph, the situation is very different when graphene presents a strong electron doping.

3.3.3. CoPc on graphene/$SrTiO_3$

In *Figure 3.27* and *Figure 3.28* XAS and XMCD spectra of CoPc on graphene/$SrTiO_3$ are presented. Spectra have been collected at the Co $L_{3,2}$ absorption edges in both normal and grazing incidence. The top panels show the XAS spectra before background subtraction. We notice two sharp peaks at 787 eV and 802 eV arising from the $SrTiO_3$ background which is also reported in the image. We attribute these features to Co impurities in $SrTiO_3$, as the energy distance between them corresponds to the one between L_2 and L_3 absorption edges of Co. No dichroism is associated with these features, suggesting a low spin configuration with zero spin, as it happens for Co^{3+} ions substitutional of Ti or associated with O vacancies [78].
After background subtraction (bottom panels of *Figures 3.27* and *Figure 3.28*) we find a dramatic change in the shape of the XAS spectra compared to the cases seen in the previous paragraphs. Moreover, the XMCD signal is extremely reduced.
In particular, comparing the XAS spectra with those recorded for CoPc on HOPG and graphene/SiO_2/Si^{++}, we notice that at both normal and grazing incidence the peak on the high energy side of the L_3 absorption edge has disappeared, becoming part of the low energy side peak at 782 eV. Furthermore, the lowest energy satellite peak which was quite pronounced at grazing incidence has now strongly reduced its intensity compared to the case of HOPG and graphene/SiO_2/Si^{++} substrates. These strong variations of the XAS lineshape indicate a strong modification of the final state configuration of the system, compared to the cases studied in the previous paragraphs.

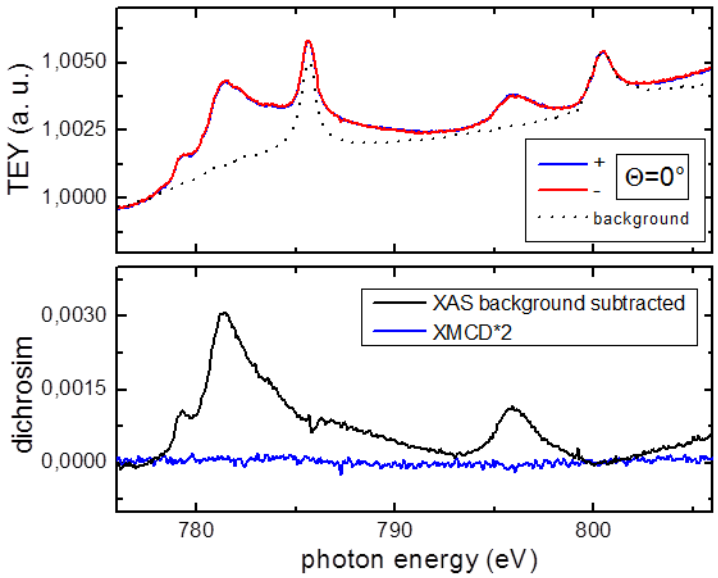

***Figure 3.27**: Circularity polarized XAS and XMCD for Co-Pc deposited on graphene/$SrTiO_3$ at normal incidence. . In the top panel as-measured absorption spectra taken with positive (+) and negative (-) circular polarized light are presented, together with the HOPG background spectra measured before Co-PC deposition. In the bottom panel the XAS after background subtraction and XMCD spectra are shown The structure at 787.5 eV is an artifact, introduced during background subtraction.*

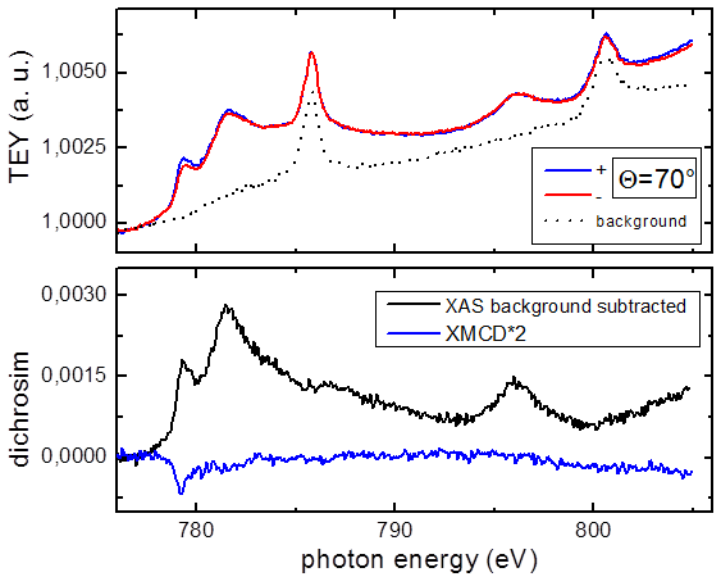

***Figure 3.28**: Circularity polarized XAS and XMCD for Co-Pc deposited on graphene/$SrTiO_3$ at grazing incidence. In the first panel absorption spectra with positive and negative circular polarized incident light and the graphite background spectra are presented, while in the second panel XAS spectra obtained as $(I^+-I)/2$ once subtracted from the background and XMCD spectra are presented.*

In *Figure 3.29* a comparison between XAS spectra collected at normal incidence and low temperature for the three systems under study are presented. For clarity, the absorption intensities have been scaled by a factor.

Since graphene on SiO_2/Si^{++} and on $SrTiO_3$ is produced under the same conditions, the morphology landscape offered to the CoPc should not differ, as we have already observed in Chapter 1 about sample characterization. The two systems are therefore expected to differ only in the carrier doping.

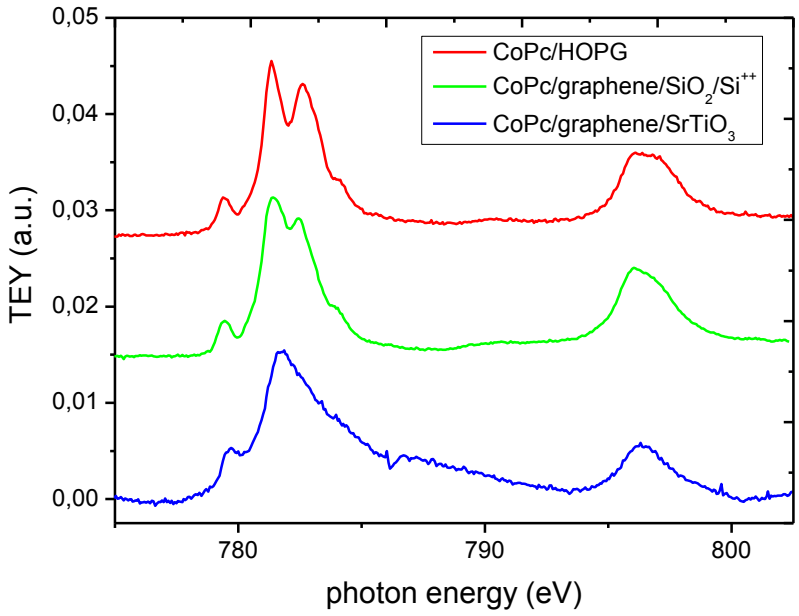

***Figure 3.29**: XAS spectra at normal incidence, comparison between the different samples investigated. The XAS signals have been scaled for CoPc/HOPG (factor ×1.5) and CoPc/graphene/$SrTiO_3$ (factor ×5) to make easier the comparison with the XAS of CoPc/ SiO_2/Si^{++}.*

Looking at the data in *Figure 3.27* and *Figure 3.28*, we observe that no XMCD signal is found for CoPc on graphene/$SrTiO_3$ in the out-of-plane direction and an extremely small, almost zero signal in the in-plane direction. This indicates that the local magnetic moment of the Co ion is now much reduced.

This behavior is consistent with experimental results and calculations for a monolayer or less of Co-Pc molecules deposited on a metallic substrate, where charge transfer from the substrate occurs. Here, quenching of the Co ion spin is due to the transfer of an

electron from the metal to the TM ion in order to fill the a_{1g} orbital. This extra electron would be coupled antiferromagnetically with the original spin, due to Pauli exclusion principle.

A more detailed description of the physics involved in the charge transfer process has been developed by Stepanow *et al.* in Ref. [28]. Studying a Co-Pc monolayer deposited on Au(111), they conclude that the 3*d* ground state of the system can be described as a coherent superposition of two charge states $d^7E + d^8$, where d^7 is the unperturbed configuration of the Co ion in the absence of interaction with the substrate, while *E* is an electron of the substrate antiferromagnetically coupled with the central metal ion of the molecule [28]. The d^8 configuration in this case has also zero spin, due to filling of the a_{1g} orbital. In *Figure 3.30* [28] a schematic view of this model is presented.

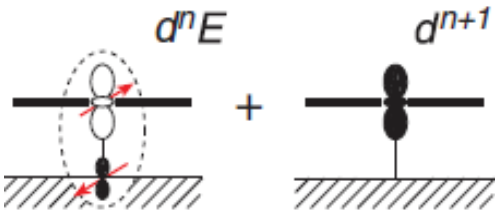

***Figure 3.30**: Charge transfer between metallic-like surface and CoPc molecule adsorbed on it. From Ref [28].*

The introduction of the mixed valence state in the model allows a better agreement between experimental and calculated XAS in the specific case of CoPc/Au(111), reported in *Figure 3.31* [28]. If we compare the latter spectra with our results on CoPc/graphene/$SrTiO_3$, we can find strong similarities in the XAS shape. It appears therefore that our electron-doped graphene provides an electron reservoir for the CoPc molecules, as well as the metallic Au surface does.

The residual dichroism observed in our spectra at grazing incidence could be due to the presence of uncoupled molecules that do not interact with the substrate, as a result of surface roughness or areas with PMMA. A non flat alignment of the molecules would also result in a different XAS line shape compared to CoPc on HOPG and on graphene/SiO_2/Si^{++}, however (i) linear dichroism at the *K*-edge is still observed (see below) and (ii) the non-flat orientation would not trivially lead to vanishing dichroism.

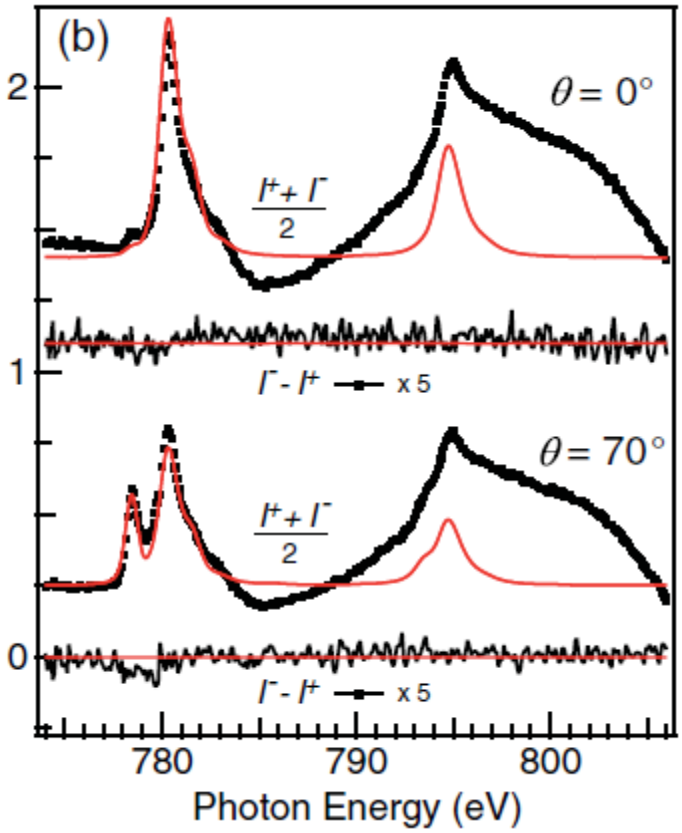

***Figure 3.31**: Circularity polarized XAS and XMCD for Co-Pc monolayer on Au(111) from experiments (dotted line) and simulated (solid line). Extracted from Ref. [28]*

As far as it concerns the crystal field and the orientation of CoPc molecules and their electronic states, XLD spectra at Co $L_{2,3}$ and at nitrogen *K* edges are presented in *Figure 3.32* and *Figure 3.33*.

A small dichroism is still present at both edges, suggesting (i) a flat orientation of the CoPc molecules on the substrate and (ii) the presence of a reduced symmetry environment for the Co ion. These findings also suggest that the CoPc molecule still maintains the same structure on this substrate, and no breaking of the molecule occurs. The weaker dichroism can be related again to the extended defects (PMMA) eventually present on the graphene/$SrTiO_3$ that can lead to a more consistent dislocation of the molecules. A poor statistics due to the very small number of molecules on this sample should also be taken into account, made worst by the fact that the $SrTiO_3$ background signal is much more prominent than the one of SiO_2/Si^{++}.

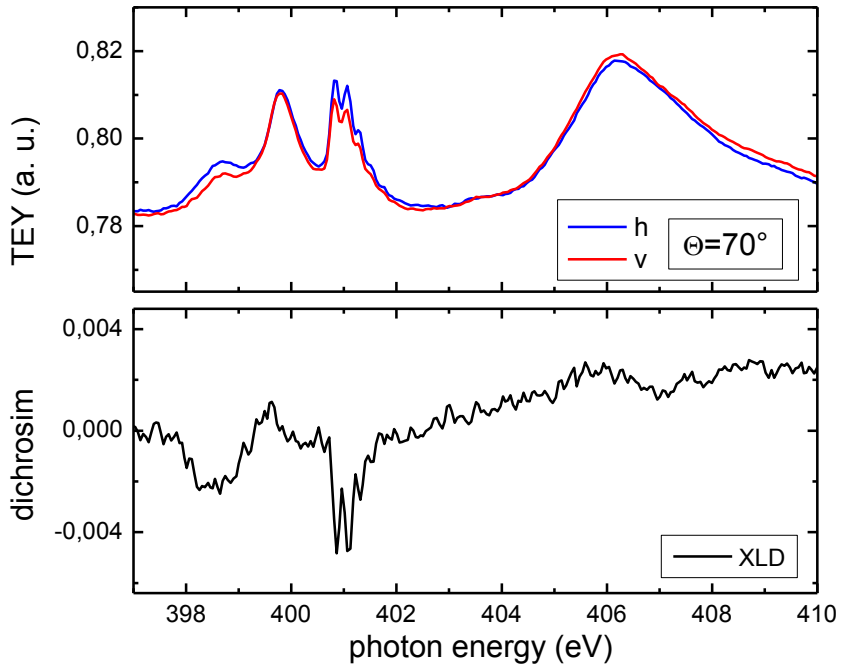

***Figure 3.32**: XLD spectra from CoPc on graphene/$SrTiO_3$ at N K edge and grazing incidence. The upper panel is dedicated to linear polarized absorption with horizontal and vertical polarization, while in the lower panel the linear dichroism is presented.*

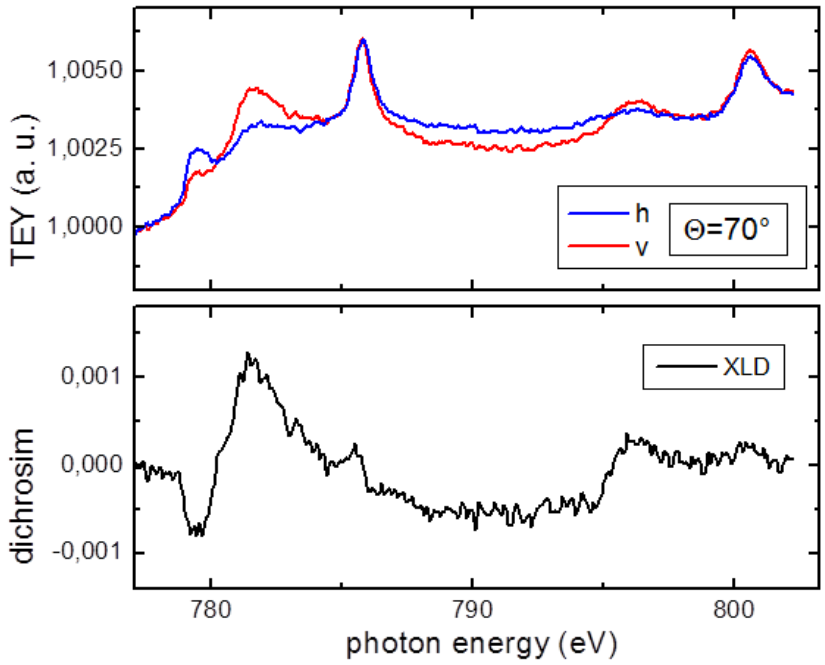

***Figure 3.33**: XLD spectra from CoPc on graphene/$SrTiO_3$ at Co edge and grazing incidence. In the first panel linear polarized absorption with horizontal and vertical polarization is presented, while the second panel is dedicated to the linear dichroism.*

More measurements are planned for this system, in order to fully characterize the CoPc electronic and structural configuration. In particular, we intend to make measurements of the linear and circular dichroism at intermediate angles and to record the substrate background also at the nitrogen *K*-edge, that will help to make our data more "clean" and therefore easier to evaluate.

3.3.4. Summary

In conclusion, our experiments suggest that a large number of CoPc molecules interact strongly with the electrons of graphene on $SrTiO_3$, and the hybridization of *3d* orbitals with graphene π band leads to charge transfer from the graphene Fermi level into the empty *d* orbital. As a consequence, almost complete quenching of the Co ion spin moment is observed.

Since the major difference between graphene/SiO_2/Si^{++} and graphene/$SrTiO_3$ is the position of the Fermi level with respect to the Dirac point, it seems reasonable to deduce that hole doped (such as graphene/SiO_2/Si^{++}) or almost neutral (in first order approximation we can assume it comparable with graphite) graphene does not interact with the adsorbed Co-Pc molecules. Opposite to that, electron doped graphene (such as graphene/$SrTiO_3$) appears to behave like a metal and its electrons form hybrid states with the molecules., which leads to a strong modification of their electronic and magnetic state.

For the future we plan to repeat part of our measurements, especially those about CoPc/$SrTiO_3$ and also to simulate the results with the proper code, in order to corroborate the interpretation of our present data.

Conclusions and outlook

In the following the main achievements of this thesis work will be summarized, then an outlook on future experiments will be presented.

First of all we were able to develop proper graphene substrates that both satisfied the requirements of having large graphene surface available for X-ray measurements and the possibility of applying a back gate in order to get information on the graphene doping (holes or electrons at the Fermi level). For this aim CVD graphene has been used, and an improved preparation procedure has been developed.

Graphene samples have been prepared not only using the standard SiO_2/Si^{++} substrate, but also adjusting the preparation technique in order to try different substrates, such as $SrTiO_3$, which present the advantage of having a very large dielectric constant, especially at low temperature and small electric fields, so that a very high density of induced charges can be achieved by applying a relatively small gate voltage.

Graphene samples reveal a quite smooth surface with a small amount of defects, such as wrinkles, PMMA residuals and impurities. Despite differences in the two dielectric materials used as a substrate no particular differences concerning the morphological proprieties of graphene have been noticed.

The doping in both samples, characterized by field effect measurements, are be different. Interestingly, in fact, graphene on SiO_2/Si^{++} was always hole doped, while graphene on $SrTiO_3$ was electron doped. Due to a multiplicity of causes that can introduce doping in the system, it has not been possible to attribute the doping level to the differences between substrates only, therefore all the samples have been monitored before and during the x-ray experiments.

X-ray absorption experiments have been performed at the European Synchrotron Radiation Facility (ESRF) in order to characterize the coupling between CoPc and graphene.

Molecules have been evaporated in-situ at room temperature. Evaporation has been calibrated on a copper substrate by means of STM technique. About 10% of a ML of

molecules has been deposited on the graphene surface.

X-ray measurements have been preliminary performed on a HOPG substrate used as reference. We found that CoPc molecules lie flat on the HOPG surface and no charge transfer effect with the substrate is noticed. Co ions in the molecule retain their crystalline ground state with a d^7 configuration and spin S=1/2, due to D_{4h} crystal field given by the ligands.

By a comparison between spectra obtained on HOPG and hole doped graphene/SiO_2/Si^{++} we can assume the same behavior, apart from a small reduction in the dichroism indicating the presence of defected regions with high roughness (most probably PMMA residuals) where the molecules, following the substrate, assume several orientations respect to the sample normal.

Finally CoPc molecules on electron doped graphene/$SrTiO_3$ present a completely different behavior, suggesting a charge transfer effect between graphene and molecules that leads to a strong reduction of the spin moment.

Our preliminary experiments therefore suggest that coupling of graphene π electrons with the *d* states of a CoPc molecule can indeed occur in samples with large electron doping. This finding suggest a way to manipulate the single molecule magnets spins by means of a substrate with tunable chemical potential such as graphene.

Inspired by these results, in the future we are planning to focus on experiments where charge transfer could be externally and reversibly triggered and not only induced by a different chemical doping of samples. The main idea is to reversibly tune the graphene doping from holes to electrons (or vice versa) by applying back-gate voltages.

Same attempts have been already done using graphene/SiO_2/Si^{++}. Due to the high level of doping induced in these samples by the CVD growth and transfer process, voltages above 80V result necessary in order to change the sign of the doping. However, the excess leakage current through the 300 nm thin SiO_2, increasing orders of magnitude with the sample exposed to the beam, made the gating experiment unpractical.

Our new idea is to use different kinds of oxide gate dielectrics: such as (i) $SrTiO_3$ and (ii) $BaTiO_3$ single crystals with (001) orientation. $SrTiO_3$ has been already introduced for preliminary measurements in the experiments presented in this thesis as a substrate for chemically electron doped graphene. As already seen, it has a very large dielectric

constant at cryogenic temperatures allowing a quite large change of the carrier density in graphene with reduced applied back-gate. In particular we have verified that the Diract point, and so the turning point between hole and electron doping, can be found within the feasible range of ±15V.

$BaTiO_3$ is instead a ferroelectric material, and it has been verified (M. Salluzzo *et al*., private communication) that a gate voltage of ±60V at room temperature can stabilize a spontaneous polarization **P**, perpendicular to the surface. This state is non-volatile, thus allowing X-ray measurements on graphene with two different doping states (hole, $\mathbf{P}^+$ state, electrons $\mathbf{P}^-$ state).

Appendix A

Probe station for field effect measurements at NANOsciences

In this appendix the field effect measurements at NANOsciences will be addressed, with a focus on the experimental set-up and procedure. First, the electrodes deposition on graphene will be explained, then a brief description of the probe station will be made.

A.1. Electrodes deposition

Before performing transport measurements, it is necessary to evaporate electrodes on the graphene surface. The method used for metal deposition is electron bombardment evaporation. A high current (of the order of 100 mA) is flown across a metallic filament that emits electrons for thermionic effect. Electric and magnetic fields are used to accelerate the emitted electrons towards a target that contains the metal to evaporate. Metal atoms are then ejected in all directions, hitting the sample. The sample is protected by a mechanical mask, in this way a uniform electrode layer is deposited only on the unprotected graphene regions.

A quartz oscillator is used to control the deposition thickness. As metal is deposited on the oscillator surface, its mass increases and the frequency of oscillation decreases. The change in frequency can be associated with the deposited metal thickness. The process is done in high vacuum ($\sim 10^{-6}$ mbar) in order to avoid the reaction or the scattering of

the evaporated atoms with the atoms in the chamber.

In the case of our samples we have used a deposition rate of 2÷5 Å/s and we have deposited 100 nm thick electrodes, made by 5 nm of titanium put in direct contact with graphene, and 95 nm of gold.

In fact, it has been found that materials making the best electrical contact with graphene are Pd/Pt or Ti/Au [79]. The thin film of Pd or Ti is used to achieve an ohmic contact between graphene and the Pt or Au electrodes, in order to avoid the formation a of a Schottky barrier, that would inhibit a linear relation between the current *I* and the applied voltage *V* in resistivity measurements. We have tried to use both combinations but finally we have selected the Ti/Au, because Ti sticks better than Pd on the graphene layer.

In *Figure A.1* an image of our samples at the end of the electrodes deposition is shown.

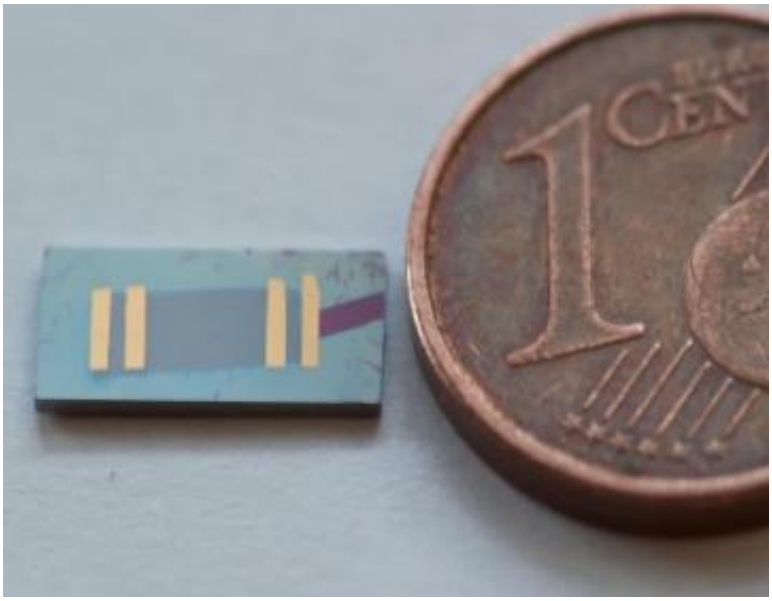

***Figure A.1**: graphene on SiO_2/Si^{++} wafer after Ti/Au electrodes deposition.*

In case of graphene samples transferred on $SrTiO_3$ it is also necessary to deposit a back gate electrode. We have deposited 100 nm thick platinum electrode on the back side of the substrate following the same procedure described above. A mechanical mask has been used in this case also to protect the substrate face covered with graphene and to

avoid platinum deposition on the lateral sides of the substrate which could short circuit graphene and the back electrode.

A.2. Field effect measurements

Field effect measurements have been performed in the probe station of the experimental room at NANOsciences, at room temperature and in vacuum conditions (P ~ 10^{-7} mbar). In *Figure A.2* a very simplified scheme of the experimental setup is reported.

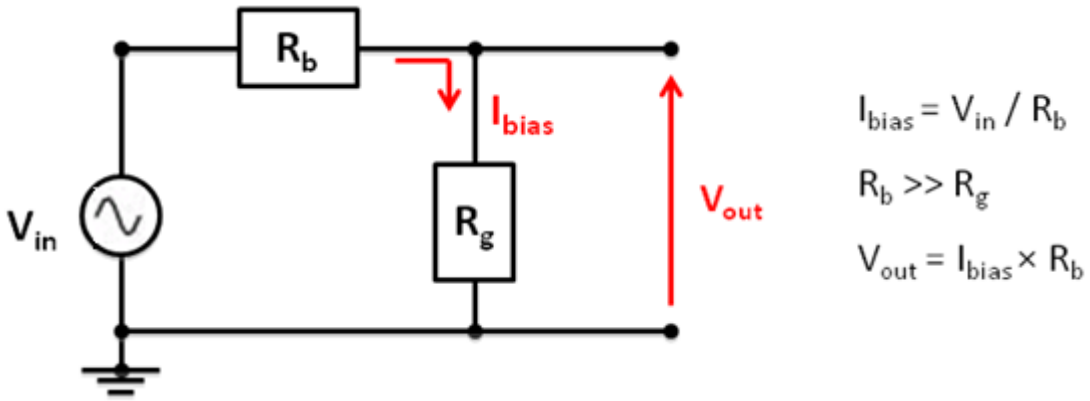

***Figure A.2**: Simplified scheme of the experimental setup for electric characterization.*

An AC voltage of 0.1 V at 383.17 Hz, in parallel with a 10 MΩ resistor (R_b) is used to bias the graphene samples. Since the latter have resistance R_g in the range between a few hundreds of ohms to a few kilo ohms, a current bias configuration is achieved.
Voltage drop of the sample is probed by a lock-in detector which is also used to source the 0.1 V AC sinusoidal voltage. By recording the *dI/dV* curve as a function of gate voltage, it is possible to obtain the field-effect curve of the graphene flake.
Measurements are performed in vacuum as moisture coming from the air could dope the sample significantly, resulting in a different doping depending on the air humidity.

Appendix B

A brief introduction to synchrotron radiation

Synchrotron radiation is an electromagnetic radiation emitted by charged elementary particles, usually electrons, moving closed to the speed of light when their trajectory is deflected by a bending device, which can be a either a single bending magnet or a periodic array of magnets, such as (i) wigglers or (ii) undulators [80].

A detailed discussion of the physics underlying the radiation process is out of the scope of this thesis and for that we refer to the literature [80].

In the following, only the characteristics making synchrotron radiation an extremely valuable probe in condensed matter physics will be discussed.

First of all, it presents a tunable emission spectrum with a bandwidth related to the characteristic of the bending device. The central frequency of the emitted photons in fact depends on the energy of the radiating particles and on the strength of the field produced by the bending magnets. Therefore, it can be varied continuously. This property of the synchrotron radiation makes it the only tunable source of photons in the soft x-ray region (10-1000 eV), which is the relevant spectral range for excitation processes from atomic core levels and the 3d states in which we are interest in this thesis.

Moreover, synchrotron radiation presents a very high intensity, as the power emitted by a single electron increases very rapidly with its energy and with the strength of the bending field.

Synchrotron radiation is even collimated, due to the relativistic velocity of the electrons

implying that the radiation is emitted in a narrow cone tangential to their curve trajectory.

The high degree of collimation and the elevated intensity determine the extraordinary brightness of the synchrotron radiation (defined as the number of photons emitted by a radiative source per unit time, solid angle, and area in 0.1% bandwidth). The high brightness allows to concentrate under a well defined angle a large number of photons, on a small sample area, increasing the sensitivity of the experiment.

Finally, synchrotron radiation presents a high degree of polarization, where the polarization vector can be modified by controlling the type of emission device and the direction of emission.

In conclusion, these peculiar proprieties of the synchrotron radiation allow to control the incident photon energy, direction and polarization in absorption processes, while the high brightness allows a very large sensitivity in spectroscopy techniques

Appendix C

Sample holder for combined XMCD and transport measurements

In this appendix a detailed description of the special sample holder developed for combined XMCD and transport measurements will be presented. This tool was first developed by the former ID08 beamline scientist J. Criginsky Cezar.
A schematic model of the sample holder will be discussed with a particular focus on the modifications we have introduced to make it compatible with the clean-room made graphene samples.

C.1. Sample holder with electrical connections

In order to insert the samples in the High Field Magnet (HFM) probe station and to move them between the different preparation facilities, vacuum manipulators and aluminium samples holders are used. Samples can be attached to the sample holders either mechanically or by means of proper UHV glues. The sample holders are then connected to the HFM cold finger at the bottom of the VTI (Variable Insertion Device), in the position for X-ray absorption measurements. In order to allow XAS, XMCD and XLD characterization and transport measurements in the same position, the sample holders are provided with electrical connections. The contact with an external voltage power supply and eventual electrometers is made by an intermediate stage of pins which

are attached to the bottom of the VTI, as seen in the drawing of Figure *C.1*. Here, the 8 pins of the sample holder and the corresponding electrical connections on the cold finger are indicated. Isolation between pins in the sample holder is provided by the use of insulating fittings made of UHV compatible materials.

The bottom of the cold finger has a threaded hole which accepts the complementary M4 screw on the sample holder top. The thread is made such as the contact between the corresponding pins in the two parts occurs when the sample holder is fully screwed in.

Electrical connections include a high voltage line, where up to 1000V can be sustained.

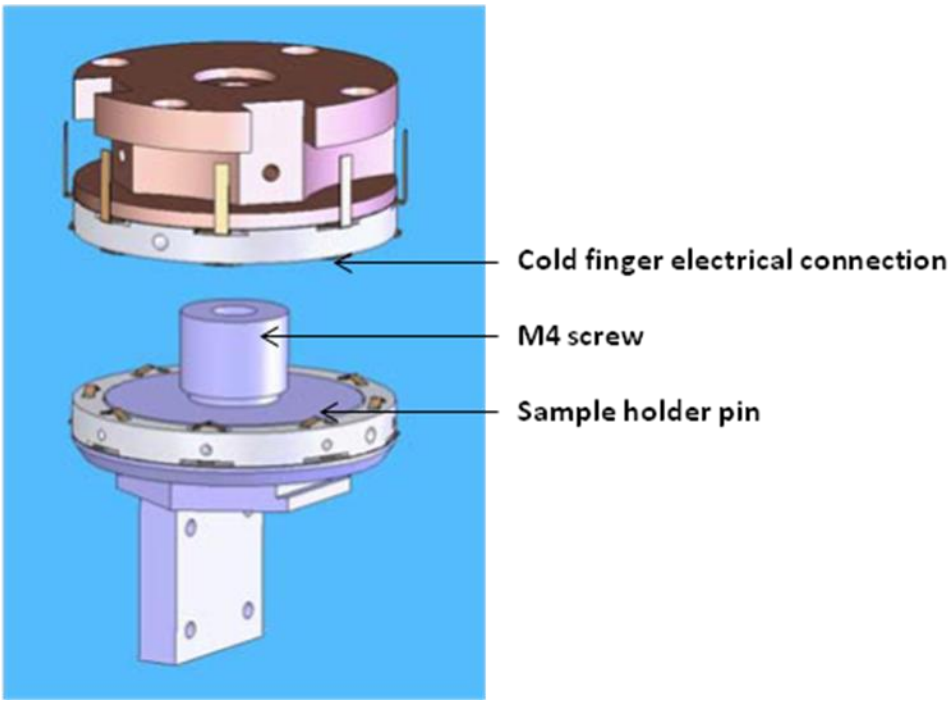

Figure C.1*: High field magnet end station sample holder with multiple electrical contacts, and bottom part of the VTI with corresponding connections.*

C.2. Connecting the sample to the sample holder

In order to use the same sample holder for XAS and field effect measurements, the graphene/SiO_2/Si^{++} samples cannot be attached directly to the sample holder. The latter

in fact are always grounded by the connection to the ammeter used to record the sample drain current in TEY mode. The back gate needs therefore to be isolated from the sample holder. In *Figure C.2* the configuration we developed in order to avoid this problem is presented.

A piece of sapphire properly cut and shaped by hand is placed between the sample holder and the sample itself. Sapphire is an electrical insulator, but it is a good thermal conductor, so that the sample is still in thermal contact with the cold finger, but it is no more grounded to the sample holder.

Sapphire has been attached to the sample holder using silver paint, an UHV glue. Since silver paint is conductive, attention must be paid in order not to put in near the edges of sapphire, risking of creating shorts.

In the future this problem will be avoided by using properly designed sapphire samples that will be mechanically screwed on the sample holder.

The sample itself is connected to the sapphire using silver paint. In that case the conductive behaviour of the glue is desirable, since it will be used as a back gate, together with the doped Si^{++} substrate, as in the case of graphene/SiO_2/Si^{++} samples (shown in *Figure C.2*), or the back deposited Pt film, as in the case of graphene/$SrTiO_3$.

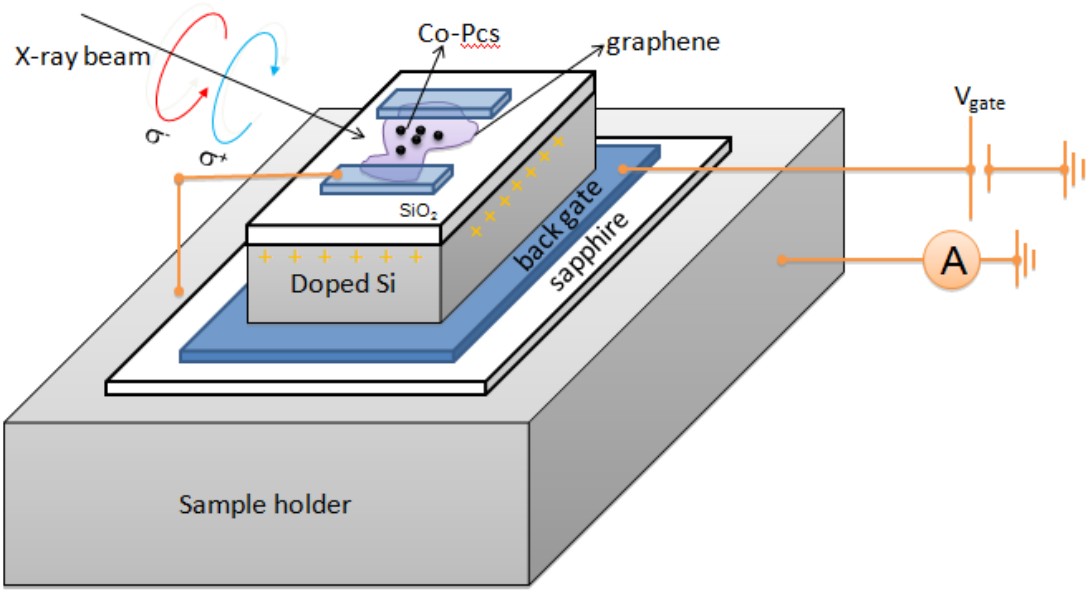

***Figure C.2**: Schematic drowning of the connection of the sample on the sample holder with electrical contacts.*

After gluing the sample on the sample holder, tiny wires must be used to connect the electrodes previously evaporated on graphene with the pins of the sample holder. One electrode is directly connected to the sample holder (see *Figure C.2*), and it carries the TEY signal.

The back gate is connected to the high voltage (HV) pin and the remaining electrode(s)[20] is connected to a standard normal pin and can be used for resistivity measurements. In *Figure C.3* a picture of the presented system is shown.

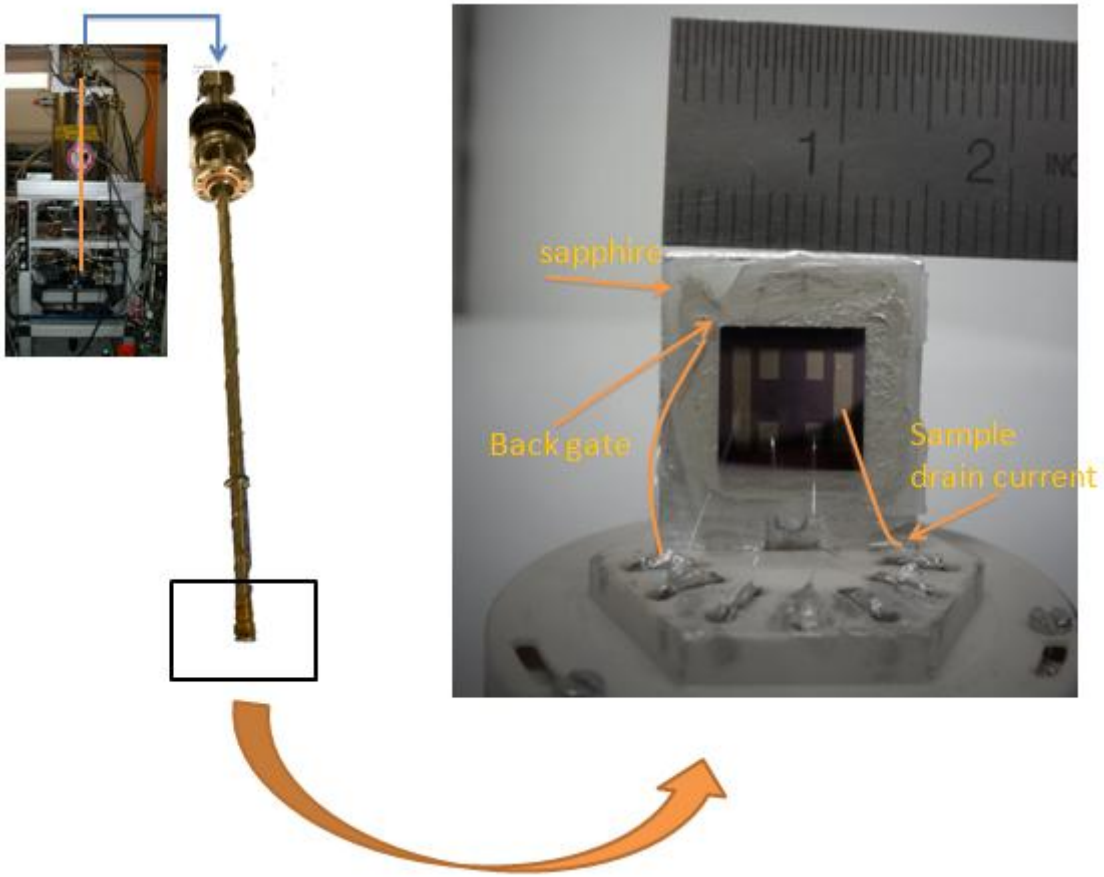

***Figure C.3**: High field magnet at ID08 with a zoom on the VTI (left side). The sample holder is connected to the bottom of the VTI which acts as a cold finger. A graphene/SiO_2/Si^{++} sample with several electrodes is also shown (right side).*

[20] In principle only two electrodes are necessary (see Appendix A for more detail), but since electrodes deposition and subsequently wire bonding on graphene samples are very critical processes, extra electrodes can be used.

Bibliography

[1] V.W. Brar, R. Decker, H.M. Solowan, Y. Wang, L. Maserati, K.T. Chan, H. Lee, C.O. Girit, A. Zettl, S.G. Louie, M.L. Choen, M.F. Crommie, Gate-controlled ionization and screening of cobalt adatoms on a graphene surface, *Nat. Phys.***7**: 43-47 (2011).

[2] D.D. Awshalom, M.M. Flatte, Challenges for semiconductor spintronics, *Nat. Phys*. **3**: 153‑159 (2007).

[3] S.A. Wolf, D.D. Awschalom, R.A. Buhrman, J.M. Daughton, S. von Molnar, M.L. Roukes, A.Y. Chtchelkanova, D.M. Treger Spintronics: a spin-based electronics vision for the future, *Science* **294**: 1488–1495 (2001).

[4] K.S. Novoselov, A.K. Geim, S.V. Morozov, D. Jiang, Novoselov, Y. Zhang, S.V. Dubonos, I.V. Grigorieva, and A.A. Firsov, Electric field effect in atomically thin carbon films, *Science* **306**: 666 (2004).

[5] A.K. Geim, K.S. Novoselov, The rise of graphene, *Nat. Mat.***6**: 183-191 (2007).

[6] P.R. Wallace, The band theory of graphite, *Phys. Rev.***71**: 622-634 (1947).

[7] R.E. Peierls, Quelques proprietes typiques des corpses solides, *Ann. I. H. Poincare* **5**: 177–222 (1935).

[8] L.D. Landau, Zur Theorie der phasenumwandlungen II., *Phys. Z. Sowjetunion* **11**: 26–35 (1937).

[9] N.D. Mermin, Crystalline order in two dimensions, Phys. Rev. 176: 250–254 (1968).

[10] J.A. Venables, G.D.T. Spiller, M. Hanbucken, Nucleation and growth of thin films, Rep. Prog. Phys. 47: 399-459 (1984).

[11] J.C. Meyer, A.K. Geim, M.I. Katsnelson, K.S. Novoselov, T.J. Booth, S. Roth, Structure of suspended graphene sheets. *Nat. Lett.* **446**: 60-63 (2007).

[12] P.R. Wallace, The band theory of graphite, *Phys. Rev.* **71**: 622-634 (1947).

[13] M.O. Goerbig, P. Lederer, Lectures on quantum Hall effect and bidimensional electrons in high magnetic fields, Orsay (2006).

[14] G.W. Semenoff, Condensed-matter simulation of a three-dimensional anomaly, *Phys. Rev. Lett.* **53**: 2449-2452 (1984).

[15] H. Lui, Y. Lui, D. Zhu, Chemical doping of graphene, *Journal of A Materials Chemistry* **21**: 3335-3345 (2011).

[16] J.H. Chen, W.G. Cullen, C. Jang, M.S. Fuhrer, E.D. Williams, Defect scattering in graphene, *Phys. Rev. Lett.* **102:** 236805 (2009).

[17] B. Partoens, F.M. Peeters, From graphene to graphite: Electronic structure around the K point, *Phys. Rev. B* **74**: 075404 (2006).

[18] D. F. Shriver, P.W. Atkins, C.H. Langford, Inorganic Chemistry – 2nd edition, Oxford University Press, Oxford New York (1994).

[19] R. Sessoli, D. Gatteschi, A. Caneschi, M.A. Novak, Magnetic bistability in a metal-ion cluster, *Nature* **365**: 141 - 143 (1993).

[20] L. Bogani, W. Wernsdorfer, Molecular spintronics using single-molecule magnets, *Nat. Mat.* **7**: 179-186 (2008).

[21] N.B. McKeown, Phthalocyanine Materials: Synthesis, Sturcture and Function, Cambridge University Press, Cambridge (1998).

[22] N. Papageorgiou, J.C. Mossoyan, M. Mossoyan-Deneux, G. Terzian, E. Janin, M. Göthelid, L. Giovanelli, J.M. Layet, and G. Le Lay, High resolution synchrotron radiation PES study of PbPc deposited on Pt(111), *Appl. Surf. Sci*. **162-163**: 178-183 (2000).

[23] K. M. Kadish, K. M. Smith, and R. Guilard, The Porphyrin Handbook – vol. 16, Phthalocyanines: Spectroscopic and Electrochemical Characterization, Elsevier Science, San Diego (2003).

[24] X. Lu, W. Hipps, Scanning Tunneling Microscopy of Metal Phthalocyanines: d^6 and d^8 Cases, *J. Phys. Chem. B* **101**: 5391-5396 (1997).

[25] H. Peisert, M. Knupfer, J. Fink, Electronic structure of partially fluorinated copper phthalocyanine ($CuPCF_4$) and its interface to Au(100).

[26] A. Zhao, Q. Li, L. Chen, H. Xiang, W. Wang, S. Pan, B. Wang, X. Xiao, J. Yang, J.G. Hou, Q. Zhu, Controlling the Kondo Effect of an Adsorbed Magnetic Ion Through Its Chemical Bonding, *Science* **309**: 1542-1544 (2005).

[27] A. Ruocco, F. Evangelista, R. Gotter, A. Attili, G. Stefani, Evidence of Charge Transfer at the Cu-phthalocyanine/Al(100) Interface, *J. Phys. Chem. C* **112**: 2016-2025 (2008).

[28] S. Stepanow, P.S. Miedema, A. Mugarza, G. Ceballos, P. Moras, J.C. Cezar, C. Carbone, F.M.F. de Groot, P. Gambardella, Mixed-valence behavior and strong correlation effects of metal phthalocyanines adsorbed on metals, *Phys. Rev. B* 83: 220401 (2011).

[29] P.A. Reynolds, B.N. Figgis, Metal Phthalocyanine Ground States: Covalence and ab Initio Calculations of Spin and Charge Densities, *Inorg. Chem.* **30**: 2294-2300 (1991).

[30] M.G. Betti, P. Gargiani, R. Frisenda, R. Biagi, A. Cossaro, A. Verdini, L. Floreano, C. Mariani, Localized and Dispersive Electronic States at Ordered FePc and CoPc Chains on Au(110), *J. Phys. Chem. C* **114**: 21638–21644 (2010).

[31] Z. Hu, B. Li, A. Zhao, J. Yang, J.G. Hou, Electron and Magnetic Proprieties of Metal Phthalocyanine on Au(111) Surface: A First-Principle Study, *J. Phys. Chem.***112**: 13650-13655 (2008).

[32] B.W. Heinrich, C. Iacovita, T. Brumme, D.-J. Choi, L. Limot, M.V. Rastei, W.A. Hofer, J. Kortus, J.-P. Bucher, Direct Observation of the Tunneling Channels of a Chemisorbed Molecule, *J. Phys. Chem. Lett.* **1**: 1517-1523 (2010).

[33] J. Brede, N. Atodiresei, S. Kuck, P. Lazic, V. Caciuc, Y. Morikawa, G. Hoffmann, S. Blugel, R. Wiesendanger, Spin- and Enery-Dependent Tunneling through a Single Molecule with Intramolecular Spatial Resolution, *Phys. Rev. Lett.* **105**: 047204 (2010).

[34] A. Zhao, Q. Li, L. Chen, H. Xiang, W. Wang, S. Pan, B. Wang, X. Xiao, J. Yang, J.G. Hou, Q. Zhu, Controlling the Kondo Effect of an Adsorbed Magnetic Ion Through Its Chemical Bonding, *Science* **309**: 1542-1544 (2005).

[35] E. Annese, J. Fujii, I. Vobornik, G. Rossi, Structure and Electron State of Co-phthalocyanine Interacting with the Cu(111) surface, *J. Phys Chem. C* Chem. **115**: 17409–17416 (2011).

[36] A. M. Cassell, J. A. Raymakers, J. Kong, H. Dai, Large Scale CVD Synthesis of Single-Walled Carbon Nanotubes, *J. Phys. Chem. B* **103**: 6484-6492 (1999).

[37] X. Li, W. Cai, J. An, S. Kim, J. Nah, D. Yang, R. Piner, A. Velamakanni, I. Jung, E. Tutuc, S. K. Banerjee, L. Colombo, R. S. Ruoff, Large-Area Synthesis og High-Quality and Uniform Graphene Films on Copper Foils, *Science* **324**: 1312-1314 (2009).

[38] K.S. Novoselov, A.K. Geim, S.V. Morozov, D. Jiang, M.I. Katsnelson, I.V. Grigorieva, S.V. Dubonos, A.A.Firsov, Two-dimensional gas of massless Dirac fermions in graphene, *Nature* **438**: 197-200 (2005).

[39] C. Berger, Z. Song, X. Li, X. Wu, N. Brown, C. Naud, D. Mayou, T. Li, J. Hass, A.A. Marchenkov, E.H. Conrad, P.N. First, W.A. de Heer, Electronic Confinement and Coherence in Patterned Epitaxial Graphene, *Science* **312**: 1191-1196 (2006).

[40] K.V. Emtsev, A. Bostowick, K. Horn, J. Jobst, G.L. Kellogg, L. Ley, J.L. McChesney, T. Ohta, S. Waldmann, H.B. Weber, T. Seyller, Towards wafer-size graphene layers by atmospheric pressure graphitization of silicon carbide, *Nat. Mater*. **8**: 203-207 (2009).

[41] P.W. Sutter, J.-I. Flege, E. A. Sutter, Epitaxial Graphene on Ruthenium, *Nat. Mater*. **7**: 406-411 (2008).

[42] J. Coraux, A.T. N'Diaye, C. Busse, T. Michely, Structural Coherency of Graphene on Ir(111), *Nano Lett*. **8**: 565-570 (2008).

[43] A. Reina, X. Jia, J. Ho, D. Nezich, H. Son, V. Bulovic, M.S. Dresserlhaus, J. Kong, Large area, Few-Layer Graphene Films on Arbitrary Substrates by Chemical Vapor Deposition, *Nano Lett*. **9**: 30-35 (2009).

[44] K. Natesan, T.F. Kassner, Thermodynamics of carbon in nickel, iron-nickel and iron-chromium-nickel alloys, *Metallurgical and Materials Transactions B* **4**: 2557-2566 (1973).

[45] G.A. Lopez, E.J. Mittermeijer, The solubility of C in solid Cu, *Scripta Materialia* **51**: 1-5 (2004).

[46] ASM international, Alloy Phase Diagrams Center.

[47] Q. Yu, S. Siriponglert, L. Hao, Y.P. Chen, S. Pei, Graphene segregation on Ni surfaces and transferred to insulators, *Appl. Phys. Lett.* ***93***: 113103 (2008).

[48] Z. Han, A. Kimouche, A. Allain, H. Armandi-Tash, A. Reserbat-Plantey, S. Paris, V. Reita, N. Bendiab, J. Coraux, V. Bouchait, Fully Single-Layer Graphene Grown by Pulsed Chemical Vapor Deposition, in manuscript (2011).

[49] X. Li, C.W. Magnuson, A. Venugopal, J. An, J.W. Suk, B. Han, M. Borysiak, W. Cai, A. Velamakanni, Y. Zhu, L. Fu, E.M. Vogel, E. Voelkl, L. Colombo, R.S. Ruoff, Graphene films with large domain size by a two step chemical vapor deposition process, *Nano Lett.* **10**: 4328-4334 (2010).

[50] V.E. Dorgan, M.-H. Bae, E. Pop, Mobility and Saturation Velocity in Graphene on SiO_2, *App. Phys. Lett*. **97**: 082112 (2010).

[51] T.P. Ma, P. V. Dressendorfer, Ionizing radiation effects in MOS devices and circuits, John Wiley & Sons (1989).

[52] N.J.G. Couto, B. Sacépé, A.F. Morpurgo, Transport through Graphene on SrTiO3, *Phys. Rev. Lett.* **107**: 225501 (2011).

[53] P.A. Fleurt, J.M. Worlock, Electric-Field-Induced Raman Scattering in $SrTiO_3$ and $KTaO_3$, *Phys. Rev.* **174**: 613-623 (1968).

[54] M. Salluzzo, G. Ghiringhelli, J.C. Cezar, N.B. Brookes, G.M. De Luca, F. Fracassi, R. Vaglio, Indirect Electric Field Doping of the CuO_2 Planes of the Cuprate $NdBa_2Cu_3O_7$ Superconductor, *Phys. Rev. B* **100**: 056810 (2008).

[55] O. Leenarts, B. Partoens, F. Peeters, Water on graphene: Hydrophobicity and dipole moment using density functional theory, *Phys. Rev. B* **79**: 235440 (2009).

[56] F. Schooley, W.R. Hosler, M.L. Cohen, Superconductivity in Semiconducting $SrTiO_3$, *Phys. Rev. Lett.* **12**: 474-475 (1964).

[57] J.F. Schooley, W.R. Hosler, E. Ambler, J.H. Becker, M.L. Cohen, C.S. Koonce, Dependence of the superconducting transition temperature on carrier concentration in semiconducting $SrTiO_3$, *Phys. Rev. Lett*. **14**: 305-307 (1965).

[58] L. Lui, S. Ryu, M.R. Tomasik, E. Stolyarova, N. Jung, M.S. Hybertsen, M.L. Steigerwald, L.E. Brus, G.W. Flynn, Graphene Oxidation: Thickness-DependentEtching and Strong Chemical Doping, *Nano Lett.* **8**: 1965-1970 (2008).

[59] W. Wu, Q. Yu, P. Peng, Z. Liu, J. Bao, S.S. Pei, Control of thinkness uniformity and grain size in graphene films for transparent conductive electrodes, *Nanotecnology* **23**: 035603 (2012).

[60] P. Blake, E.W. Hill, A.H.C. Neto, K.S. Novoselov, D. Jiang, R. Yiang, T.J. Booth, A.K. Geim, Making graphene visible, *App. Phys. Lett.* **91**: 063124 (2007).

[61] S. Nie, W. Wu, S. Xing, Q. Yu, S.S. Pei, K.F. McCarty, Growth from Below Bilayer Graphene on Copper by Chemical Vapor Deposition, *cond-mat.mtrl-sci*: arXiv: 1202.1031v1 (2012).

[62] C.H. Lui, L. Lui, K.F. Mak, G.W. Flynn, T.F. Heynz, Ultraflat graphene, *Nature* **462**: 339-341 (2009).

[63] Z.H. Ni, Y.Y.Wang, T. Yu, Z.X. Shen, Raman spectroscopy and imaging of graphene, *Nano Research* **1**: 273-291 (2008).

[64] D.R. Cooper, B. D'Anjou, N. Ghattamaneni, B. Harack, M. Hilke, A. Horth, N. Majlis, M. Massicotte, L. Vansburger, E. Whiteway, V. Yu, Experimental review of graphene, *cond-mat.mes-hall* arXiv:1110.6557v1 (2011).

[65] J. Stohr and Y. Wu, In X-ray Magnetic Circular Dichroism: Basic Concepts and Theory for 3d Transition Metal Atoms, edited by A. S.Schlachter and F.J. Wuilleumier (Kluwer Academic Publishers, 1994),volume 254 of NATO ASI Series E: Applied Sciences, p. 221.

[66] F. de Groot, A. Kotani, Core level Spectroscopy of Solids (CRC Press, 2008).

[67] H. Ebert, Magneto-optical effects in transition metal systems, *Rep. Prog. Phys*. **59**: 1665 (1996).

[68] F. de Groot, J.C. Fuggle, B.T. Thole, G.A. Sawatzky, 2p x-ray absorption of 3d transition-metal compounds: An atomic multiplet description including the crystal field, *Phys. Rev. B* **42**: 5459-5468 (1990).

[69] K. Hirsh, J.T. Lau, P. Klar, A. Langerberg, J. Probst, J. Rittmann, M. Vogel, V. Zamudio-Bayer, T. Moller, B. von Issendorff, X-ray spectroscopy on size-selected clusters in an ion trap: from the molecular limit to bulk properties, *J. Phys. B: At. Mol. Opt. Phys.* 42: 154029 (2009).

[70] J. Stohr, Exploring the microscopic origin of magnetic anisotropies with X-ray magnetic circular dichroism (XMCD) spectroscopy, *J. Mag. mag. Mat.* **200**: 470-497 (1999).

[71] J. Stohr, X-Ray Absorbtion: Principles, Applications, Techniques of EXAFS, SEXAFS and XANES (Wiley, New York, 1988), p. 443.

[72] M.O. Krause, Atomic Radiative and Radiationless Yields for K and L Shells, *J. Phys. Chem. Ref. Data* **8**: 307 (1979).

[73] R. Nakajima, J. Sthor, Y.U. Idzerda, Electron-yield saturation effects in L-edge x-ray magnetic circular dichroism spectra of Fe, Co, and Ni, *Phys. Rev. B* 59: 6421-6429 (1999).

[74] M.O. Krause, Atomic radiative and radiationless yields for k and L shells, *J. Phys. Chem. Ref. Data* **8**: 307 (1979)

[75] B. N. Figgis, M. A. Hitchman, Ligand Field Theory and Its Applications, Wiley-VCH, New York (2000).

[76] C. Isvoranu, J. Ahlund, B. Wang, E. Ataman, N. Matensoon, C. Puglia, J.N. Anderson, M.L. Boquet, J. Schnadt, Electron spectroscopy study of the initial stages of iron phthalocyanine growth on highly oriented pyrolytic graphite, *J. Chem. Phys. Rev. B* **42**: 214709 (2009).

[77] E. Stavitski, F.M.F. de Groot, The CTM4XAS program for EELS and XAS spectral shape analysis of transition metal L edge, *Micron* **41**: 687–69 (2010).

[78] M.O. Selme, P. Pecheur, The electronic structure of transition-metal impurities in $SrTiO_3$, *J. Phys. C: Solid State Phys.* **21**: 1779 (1988).

[79] Q. Ran, M. Gao, X. Guan, Y. Wang, Z. Yu, First-principles investigation on bonding formation and electronic structure of metal-graphene contacts, *Appl. Phys. Lett* **94**: 103511 (2009).

[80] R. Bachrach, Synchrotron Radiation Research (Plenum New York, 1995).

Acknowledgments

I’m grateful to Prof. Giacomo Ghiringhelli from Politecnico of Milano and to Dr. Nick Brookes from ESRF for the opportunity they gave me to work in the ID08 beamline group. Thanks to them even for the help and suggestions they gave me while writing this thesis.

My profound gratitude goes to Dr. Violetta Sessi, who was definitely more than a supervisor during the months spent at the synchrotron. Thanks for having introduced me to a new world of experimental science, apparently far away from the books I was used to, where everything is already explained and clear, for the support while writing my thesis, for the nights and the weekends spent together on the beamline and for all the discussions about science and life.

Thanks, for the help and for the great time spent together, to all the staff of ID08 beamline at ESRF: Dr. Kurt Kummer, Andrea Fondacaro, Dr. Flora Yakhou, Ross Boulton, Matteo Minola. It was a pleasure working with you.

I’m thankful to all the researchers that contributed at the realization of the experiments presented in this thesis: Dr. Vincent Bouchiat, Zheng (Vitto) Han and Adrien Allain from the NANOsciences department of the Istiut Néel (CNRS), Grenoble, for the help in the realization of the graphene samples and for all the useful discussions; Soeren Krotzky and, again, Dr. Kurt Kummer for the help during the beamtime at ESRF; Dr. Marco Salluzzo and Dr. Sebastian Stepanow for all the useful suggestions; Dr. Fabio Comin, Anthony Vial and Luca Costa from SSL at ESRF, for having introduced me to the AFM technique.

Finally, thanks to my parents, ma brother and all my big family for the continuous love and support they gave me since I was born. Thanks for having been next to me, even when it was difficult, and you knows that it could be.

And thanks to Andrea, he exactly knows why, thanks because love is not only being happy together, but also supporting each other, thanks because you are more than what I expected.